

Fredrik Bonnevie Dahler  
Nicholas Thuve

# Testing and Modeling of Thick Aluminum Castings Under Impact Loadings

Master's thesis in Mechanical Engineering  
Supervisor: Prof. Magnus Langseth / Assoc. Prof. David Morin  
June 2019



Fredrik Bonnevie Dahler  
Nicholas Thuve

# Testing and Modeling of Thick Aluminum Castings Under Impact Loadings

Master's thesis in Mechanical Engineering  
Supervisor: Prof. Magnus Langseth / Assoc. Prof. David Morin  
June 2019

Norwegian University of Science and Technology  
Faculty of Engineering  
Department of Structural Engineering





## MASTER THESIS 2019

SUBJECT AREA: Impact Mechanics (SFI CASA)	DATE: 30.06.19	NO. OF PAGES: 7+138+44
---	----------------	------------------------

TITLE:

**Testing and modeling of thick aluminum castings under impact loadings**

Testing og modellering av tykke støpte aluminiumskomponenter utsatt for støtlast

BY:



Fredrik Bonnevie Dahler



Nicholas Thuve

The aim and primary objective of this thesis is to perform experimental testing of a cast aluminum rim subjected to dynamic crash loading. Based on this, a numerical model is to be established and used for numerical validation. A substantial part of the thesis is used to validate the experimental test setup which was developed the previous year for the purpose of performing dynamic testing of aluminum rims. Managing and processing sensor and measurement data in order to get trustworthy results are in focus. The numerical model aims to achieve sufficient accuracy to be used for industrial applications.

RESPONSIBLE TEACHER: Prof. Magnus Langseth

SUPERVISOR(S): Prof. Magnus Langseth and Assoc. Prof. David Morin

CARRIED OUT AT: SFI CASA, Department of Structural Engineering, NTNU



## MASTER THESIS 2019

Fredrik Bonnevie Dahler and Nicholas Thuve

### **Testing and modeling of thick aluminum castings under impact loadings**

(Testing og modellering av tykke støpte aluminiumskomponenter utsatt for støtlast)

Nowadays, crash requirements of automotive structures involve chassis parts in addition to the traditional body in white. Recently, the Insurance Institute for Highway Safety (IIHSS) in the U.S. has released new crash scenarios which solicitate the full front end of a car. For example, a new test (referred to as the small overlap frontal test), subjects only 25% of the front end of a vehicle to a 64 km/h impact. Under these circumstances, the suspension system of the vehicle, including the wheel and rim, becomes part of the solution to manage the energy from the impact. Special numerical techniques must therefore be developed to ensure the accuracy of the numerical simulations used during the design of an automotive structure. This can only be achieved by having reliable test facilities for computer code validation.

In 2018, a master thesis was run at CASA on the development of a test rig for impact testing of cast aluminum rims. The basis for the design was a numerical model of the test rig including the rim as well as the trolley and the reaction wall of the SIMLab “Kicking Machine”. The main objective with the present thesis is to get the new test rig in operation and to carry out tests for validation of a novel modeling approach for aluminum casting. The thesis work will be carried out in close cooperation with Audi and includes a trip to the Audi plant in Ingolstadt, Germany.

The activities in this master thesis research work may include:

- A literature review of aluminum alloys/castings including constitutive and failure models as well as structural testing of rims.
- Evaluation of the test rig through numerical simulations. Included here is an evaluation of how the reaction forces and deformations modes of the tested rims shall be monitored.
- Test rig arrangements.
- Material testing as well as component testing of rims.
- Validation of a numerical model based on the tests carried out.
- Reporting

The candidate may agree with the supervisors to pay particular attention to specific parts of the investigation, or include other aspects than those already mentioned. The thesis is to be organized as a research report, recognising the guidelines provided by the Department of Structural Engineering.

The report is to be handed in not later than 15 June 2019.

Supervisors at NTNU: David Morin and Magnus Langseth

NTNU, 15 January 2019

Magnus Langseth



## Acknowledgements

We would like to express our sincere gratitude to our supervisors Professor Magnus Langseth and Associate Professor David Morin, and thank them for the valuable guidance, help and support we have gotten throughout the semester. A special thank for letting us partake in this exciting, challenging and rewarding project for our master's thesis.

We would also like to thank Tore Wisth and Trond Auestad for their invaluable work and efforts in the lab which allowed us doing all the experimental work needed. This thesis could not have been carried out without their help. Thanks to Tore for also joining us on our trip to Neckarsulm and keeping us with good company.

A huge appreciation to Arjan Strating and the team at Audi for the hospitality we were shown during our stay in Neckarsulm and for engaging discussions. We are grateful for haven gotten the opportunity to see how Audi's crash department work, and to see how the work in this thesis is relevant for real world car crash simulations. Thanks for showing us around at Audi's factory area and for showing us their impressive cars.

Thanks to Christoffer Martinsen for providing us with the basis for the numerical work, and helping us at the beginning of the semester. A considerable amount of time was saved in helping us understand how the experimental and numerical work was to be carried out. Miguel Costas must also be thanked for helping us with the numerical modeling of crash boxes.

Finally, we would like to thank our fellow students, especially Håvard Kristiansen, Gunnar Sigstad, Eyvind Evensen and Jonas Rudshaug for keeping the mood up during the semester and creating an encouraging and fun workspace.

# Abstract

## Norwegian

I denne masteroppgaven har oppførselen til støpte aluminiumsfelger fra Audi, som er utsatt for støtlast, blitt undersøkt. Det har blitt utført eksperimenter med hensikt i å validere den numeriske modellen som er utviklet. Det eksperimentelle oppsettet har sammen med eksperimentelle resultater blitt nøye undersøkt og sammenlignet med numeriske simuleringer.

Alle forsøkene har blitt utført i sparkemaskinen som er tilgjengelig i laben ved instituttet for konstruksjonsteknikk på NTNU. Testoppsettet som ble benyttet var spesialdesignet for dynamisk testing av felger og kan motstå kreftene som kommer som følge av den fundamentale usymmetriske geometrien til en felg. Totalt har fire felger har blitt testet. For alle eksperimentene ble en tralle med masse på 1 407 kg akselerert til en hastighet på omtrent 5 m/s. Rundt 17.6 kJ med kinetisk energi blir tilført systemet som blir dissipert gjennom deformasjon av felgen. En maksimal deformasjon på omtrent 80 mm har blitt oppnådd i felgtestene, noe som er tilstrekkelig for å studere bøyning og knekking av eikene i tillegg til å få brudd i både eiker og den sylindriske flaten av felgen.

For å undersøke krasj-riggen har det blitt gjennomført forsøk med kjente krasj-bokser. Resultatene er sammenlignet med tidligere resultater. Krasj-riggen viser seg å være egnet for støttesting. Videre har den foreslåtte metoden for å estimere støtkraften på felgen vist seg å gi et godt estimat av den faktiske kraften.

For å karakterisere materialet for bruk i numerisk modellering av støtet har kvasi-statiske strekktester og dynamisk Split-Hopkinson Tension Bar (SHTB) tester blitt gjennomført. Prøvestykkene er tatt fra én felg. Strekktestene er sammenlignet med tidligere resultater og antyder at flytespenning for eikene er 200 MPa isteden for 181.3 MPa slik tidligere tester viser. Resterende parametre er i tråd med tidligere tester. SHTB tester er utført for å fastslå effekten av tøyningshastighet. Det støpte materialet har vist seg å være betinget av tøyningshastighet med materialkonstant,  $C$ , lik 0.00718 for eikene. En elastisk-viskoplastisk materialmodell er dermed valgt for numerisk modellering.

Alle numeriske analyser er utført ved bruk av Abaqus/Explicit. Modellen inkluderer alle relevante deler av krasj-riggen samt et mesh av felgen fra Audi. Den numeriske modellen fanger eksperimentelle trender, men ikke maksimal kraft. Fordeling av initial skade til eike-elementene har vist seg å være en numerisk metode som fanger opp noe av den stokastiske oppførselen til felgen.

## English

In this thesis, the structural impact behavior of cast aluminum Audi car rims has been investigated. Experiments have been carried out with the purpose of validating the numerical model. A thorough investigation of the experimental setup and the experimental results have been conducted and were compared to numerical results.

All experimental testing of rims has been carried out using the kicking machine available at the Department of Structural Engineering at NTNU. The test setup used is designed for rims in particular and capable of handling the fundamentally unsymmetrical geometry of a rim. A total number of four rims have been tested. In all tests, a trolley of mass 1 407 kg was accelerated to an approximate velocity of 5 m/s, essentially applying 17.6 kJ of kinetic energy to the system. This is in full dissipated through rim deformation. In each test a permanent deformation of approximately 80 mm was achieved, enabling the study of spoke buckling and fracture of both spokes and rim bed.

To thoroughly assess the crash rig, experiments using well-known crash boxes have also been carried out. Results are compared to previous results from conventional tests. The crash rig is found to be applicable for impact testing. In addition, the method proposed to estimate the rim crushing force is found to give a valid estimate of the true force.

For material characterization needed to numerically model the impact, quasi-static tensile and dynamic Split-Hopkinson Tension Bar (SHTB) tests have been carried out. Specimens were taken from one rim. The tensile tests were compared to previous tests and suggest a yield stress of 200 MPa for the spokes instead of 181.3 MPa from earlier. Other parameters are found to be the same as previously established. SHTB tests were used to determine strain rate sensitivity. The cast aluminum is found to be relatively dependent on the strain rate, with the material constant,  $C$ , equal to 0.00718 for the spoke section. Thus, an elastic-viscoplastic material model is found appropriate for numerical modeling.

All numerical analyses have been carried out using Abaqus/Explicit. The model takes the relevant parts of the crash rig and an orphan mesh of rim provided by Audi. The numerical model is found to capture the experimental trends but not peak loads. The distribution of initial damage to spoke elements is found to be a numerical method to capture the some stochastic behavior of the rim.

# Table of Contents

Acknowledgements . . . . .	i
Abstract . . . . .	ii
<b>1. Introduction</b>	<b>1</b>
1.1. Motivation . . . . .	1
1.2. Objective . . . . .	2
1.3. Previous Work . . . . .	3
<b>2. Theory</b>	<b>5</b>
2.1. Aluminum Die Casting . . . . .	5
2.1.1. Low-Pressure Die-Casting . . . . .	6
2.1.2. Casting Defects . . . . .	6
2.2. Flow Forming . . . . .	7
2.3. Heat Treatment . . . . .	8
2.3.1. Solution Heat Treatment . . . . .	8
2.3.2. Precipitation Heat Treatment . . . . .	8
2.4. Material Mechanics . . . . .	9
2.4.1. Elastic-Viscoplastic Modelling . . . . .	9
2.4.2. Strain Rate Sensitivity . . . . .	10
2.4.3. Ductile Failure Criteria . . . . .	10
2.4.4. Probabilistic Failure Modeling . . . . .	11
2.5. Ductile and Brittle Fracture . . . . .	12
2.6. Digital Image Correlation (DIC) . . . . .	14
2.7. Signal Processing and Filtering . . . . .	15
2.7.1. Moving Average . . . . .	15
2.7.2. Savitzky-Golay Filtering . . . . .	16
2.7.3. Digital Filtering . . . . .	18
2.8. Explicit Finite Element Method . . . . .	20

<b>3. Rim Properties and Material Characterization</b>	<b>23</b>
3.1. Properties . . . . .	23
3.2. Previous Material Characterization . . . . .	24
3.2.1. Material Testing . . . . .	25
3.2.2. Global Variation . . . . .	27
3.2.3. Material Characterization . . . . .	27
3.3. New Material Tests . . . . .	30
3.3.1. Tensile Tests . . . . .	31
3.3.2. Split-Hopkinson Tension Bar . . . . .	34
3.3.3. SHTB Tests . . . . .	36
3.4. Final Material Characterization . . . . .	40
<b>4. Force Estimation Scheme</b>	<b>41</b>
4.1. Test Design . . . . .	41
4.2. Assumptions and Simplifications . . . . .	43
4.3. Estimation of Rim Contact Force . . . . .	44
4.4. Translation from Integrated Force . . . . .	44
4.4.1. Trolley Translation from Integrated Load Cell Force . . . . .	44
4.4.2. Impact Box Translation from Integrated Forces . . . . .	45
4.5. Calculation of Forces . . . . .	45
4.5.1. Signal Processing Flow . . . . .	45
4.5.2. Numerical vs. Experimental Estimation . . . . .	46
<b>5. Numerical Modeling</b>	<b>51</b>
5.1. Base Model . . . . .	51
5.2. Numerical Validation of the Force Estimation Scheme . . . . .	56
5.2.1. Force Comparison . . . . .	56
5.2.2. Different Filters . . . . .	59
5.3. Energies . . . . .	60
<b>6. Experimental Work</b>	<b>63</b>
6.1. The Kicking Machine . . . . .	63
6.2. Design of a Test Rig for Rims . . . . .	64
6.2.1. Modifications on Final Rig . . . . .	69
6.3. Test Setup . . . . .	69
6.3.1. Cameras . . . . .	70
6.3.2. Load Cell . . . . .	71
6.3.3. Images of Test Setup . . . . .	72
6.4. Calibration of the Test Setup . . . . .	73
6.4.1. Calibration of the Load Cell . . . . .	73
6.4.2. Calibration of the Cameras and DIC Setup . . . . .	74

6.5.	Ensuring Trustworthy Measurements from the Test Setup . . . . .	75
6.5.1.	Translation Measured by DIC . . . . .	75
6.5.2.	Velocity Computed from Measured DIC Translation . . . . .	77
6.5.3.	Acceleration Computed from Measured DIC Translation . . . . .	77
6.5.4.	Voltage Measured in Strain Gauges . . . . .	78
6.5.5.	Integrated Force in Load Cell . . . . .	78
6.6.	Low-Velocity Gap Tests . . . . .	80
6.6.1.	Theoretical Pure Elastic Impact . . . . .	80
6.6.2.	Test Results . . . . .	81
6.6.3.	Rotation of Rig . . . . .	81
6.7.	High-Velocity Crash Box Test With Gap . . . . .	84
6.8.	Kinematics of the System . . . . .	86
6.8.1.	Introducing Damping in the Numerical Simulation . . . . .	87
6.9.	Validation Using Known Crash Boxes . . . . .	91
6.9.1.	Experimental Validation of the Force Estimation Scheme . . . . .	92
6.9.2.	Numerical and Experimental Comparison . . . . .	94
6.9.3.	Concluding Remarks from the Crash Box Study . . . . .	97
6.10.	Rim Tests . . . . .	97
6.10.1.	Rim Orientation . . . . .	98
6.10.2.	Estimated Crushing Force . . . . .	98
6.10.3.	Deformation History . . . . .	100
6.10.4.	Images of Crushed Rims . . . . .	100
6.10.5.	Energy Conservation . . . . .	100
<b>7.</b>	<b>Validation of the Numerical Model</b>	<b>107</b>
7.1.	Comparison of the Estimated Crushing Force . . . . .	107
7.2.	Comparison of Deformation Pattern . . . . .	109
7.3.	Comparison of Kinematics . . . . .	113
<b>8.</b>	<b>Numerical Parametric Study</b>	<b>117</b>
8.1.	Purpose of Parametric Study . . . . .	117
8.2.	Statistical Analysis . . . . .	117
8.3.	Initial Damage . . . . .	121
8.4.	Material Parameters . . . . .	121
8.5.	Remeshing . . . . .	122
8.6.	Fully Integrated Elements . . . . .	124
8.7.	Excluding Fracture . . . . .	126
<b>9.</b>	<b>Discussion</b>	<b>127</b>
9.1.	Material Characterization . . . . .	127
9.2.	Quality of the Experimental Test Concept . . . . .	128

9.3. Failure Criterion . . . . .	129
9.4. Numerical Formulation . . . . .	130
9.5. Filters . . . . .	131
<b>10. Conclusion and Further Work</b>	<b>133</b>
10.1. Conclusion . . . . .	133
10.2. Further Work . . . . .	134
<b>Bibliography</b>	<b>134</b>
<b>Appendices</b>	<b>139</b>
A. Strain Rate Sensitivity . . . . .	141
B. Filters . . . . .	143
C. Numerical Rim Results - Different Filters . . . . .	147
D. Material Card of AA6005-T6 . . . . .	151
E. Crash Box Results - Different Filters . . . . .	155
F. Rim Results - Different Filters . . . . .	159
G. Deformation Sequence . . . . .	163

# Chapter 1

## Introduction

### 1.1 Motivation

In modern times, automobile safety is an important design aspect when designing cars. Institutes such as The Insurance Institute for Highway Safety (IIHS) are dedicated to reducing casualties, injuries and property damage related to motor vehicle crashes. IIHS is a U.S. nonprofit scientific and educational organization founded in 1959 with an initial purpose to support safety efforts by others [1]. Now they serve as an independent research organization working on roadway safety through improving driver behavior, roadway design and performing safety rating crash tests.

The crash tests are performed by IIHS in their Vehicle Research Centre (VRC) which form the basis for the vehicle safety rating. Vehicles are rated depending on their performance in several tests and information is readily available for consumers to help them make informed decisions when buying cars.

In 2012, IIHS introduced a new crash test replicating a crash of the front corner of a car impacting objects like utility poles, trees or other vehicles. The small overlap front test was introduced to drive further improvements in crash protection and safety design. Traditionally, the main crush-zones of the vehicle are concentrated in the middle 50% of the front end of the car [2]. Impacts affecting the outer edges aren't necessarily protected by crush-zone structures and the crash forces may go directly into the front wheel, suspension system and firewall.



**Figure 1.1:** Small overlap crash test of the 2017 Audi Q7 [3].

The small overlap frontal test subjects only 25% of the front end of a vehicle going 40 mph (64.4 km/h) to an impact with a 5-foot tall rigid barrier [4] seen in Figure 1.1. The test has given manufacturers new challenges, especially controlling the kinematics of the car and ensuring sufficient energy absorption in the front wheel through the deformation of the rim. As this component takes on a more significant role in managing the impact forces, understanding the crashworthiness of the rim and wheel becomes more important. To ensure reliable design, special numerical techniques should therefore be developed and validated through physical tests.

## 1.2 Objective

The main objective and aim of this master's thesis is to conduct experimental crash tests of aluminum cast Audi rims and to validate the numerical model developed from earlier master theses. Further, results from this master's thesis aim to be used in industrial applications.

A significant part of this thesis will also include validation of the experimental test setup with a focus on getting trustworthy and meaningful sensor data.

This thesis is written in collaboration with Center of Advanced Structural Analysis (CASA<sup>1</sup>) at Norwegian University of Science and Technology (NTNU) and the car manufacturer Audi. The thesis is focused around an Audi Q7 rim.

---

<sup>1</sup><https://www.ntnu.edu/casa>

### 1.3 Previous Work

This thesis will in large effect tie together the work done by Kittilsen and Swanberg [5] in 2017 and Martinsen [6] in 2018. The thesis from 2017 resulted in a material characterization of the relevant Audi rim, which was validated through quasi-static compression tests. The rim material was characterized through several tensile tests from specimens of both bed and spoke section of the rim. As an outcome, the numerical model proposed included two different material characterizations, one for the rim bed and one for the spoke section as they exhibit different behavior due to the manufacturing process.

In order to fully validate the material and numerical model, it was a desire to perform dynamic crushing tests. This formed the basis for the thesis written by Martinsen. Martinsen designed a test rig enabling dynamic experiments of the rims in the "Kicking Machine" available at the Department of Structural Engineering at NTNU. To safely design the test rig a numerical model was established and simulations were run to verify the performance of the rig. Martinsen also proposed a scheme which enables estimation of the crushing force acting on the specimen. A more sophisticated estimation technique was needed as the test rig did not allow for a conventional setup in which the load cell hits the specimen directly.



## Chapter 2

# Theory

### 2.1 Aluminum Die Casting

Casting describes the process for which a liquid, often metals, is formed in a mold and takes the shape of the mold cavity as it solidifies. Solidification involves the transformation between the liquid state to its solid state and the process differs depending on the material used, though the most common methods are through cooling or a chemical reaction.

The molds may be made of materials such as sand, plaster, ceramic and metal, and different casting processes are often classified according to these molds. When the material has solidified, the mold can be opened and the cast part may be extracted.

This material forming process has great capabilities and advantages especially regarding the geometry of the specimen. Highly complex geometries can be created, including both internal and external shapes and several casting processes are capable of producing parts with no additional machining needed [7]. The process may be repeated after the casting is completed making it suitable for mass production.

Disadvantages related to casting of metal parts include limitations on mechanical properties, porosity, dimensional accuracy and surface finish depending on the casting method used. Material properties are especially sensitive to the solidification process due to fluid flow and the cooling rate which can introduce material defects. The variation of defects can be separated into global systematic variations due to the casting method and system, and local stochastic variations due to process fluctuations [8]. Casting defects are discussed in Section 2.1.2.

### 2.1.1 Low-Pressure Die-Casting

The shift towards using aluminum in structural components has been noticeable in later years, and the automotive industry is now using lightweight aluminum alloy castings for many parts traditionally made of steel and cast iron [9].

The primary process for casting aluminum alloy rims is the Low-Pressure Die-Casting process (LPDC). As the name suggests, the casting process is performed with low pressure of maximum 1 bar pushing the molten metal through an intake and into the die chamber. The pressure is sustained throughout the solidification process to minimize volume defects such as shrinkage cavities [10].

Using LPDC gives better strength and precision compared to high-pressure die-casting (HPDC), making it suitable for production of aluminum alloy rims. However, this comes at the expense of significantly slower casting cycles, typically around five to six minutes [9].

### 2.1.2 Casting Defects

Cast metals will show less ductile material properties compared to other forming methods such as extrusion and forging due to the presence of microstructural defects. The fracture behavior is strongly influenced by these defects and will cause lower material ductility [8]. Casting defects can in large be classified into four groups: macroporosity, microporosity, oxide films and exogenous inclusions [9].

#### **Macroporosity**

Macroporosity, also known as shrinkage porosity, occurs where the volumetric shrinkage associated with the solidification process is not fully opposed by sufficient feeding of liquid metal. Non-uniform solidification due to different temperature gradients along the specimen leads to pore formation as the material shrinks due to thermal contraction.

#### **Microporosity**

Microporosity or gas porosity is small gas pockets that are entrapped in the metal formed during the solidification phase. As hydrogen solubility is much greater in the liquid compared to the solid aluminum, gaseous hydrogen drops out of the solidifying melt. Furthermore, air can be enclosed in the melt due to turbulent form filling, though this is more common in HPDC.

#### **Oxide Films**

When liquid aluminum is exposed to air an oxide film quickly develops on the surface. During the filling of the form, fragments of the oxide skin may be enclosed

within the cast metal and lead to formations of defects. These defects often act as microcracks and stress concentrators.

### Exogenous Inclusions

During the filling process, some exogenous inclusions may be introduced in the cast metal. These are particles foreign to the alloy and may arise from furnace linings or die particles.

### Global and Local Variations

Defects that are due to the casting method and system are known as global systematic defects meaning certain parts and geometries may be more susceptible to defects than other parts. As a result, one will find repeated properties at the same location in multiple equal components. Local random defects, however, will vary for each component for the same area and may occur at any point in the component. The mechanical behavior of the cast component will be strongly influenced by the presence of cast defects, especially ductility. As quasi-brittle fracture is the dominant fracture behavior in cast components, the ductility can be seen as a measure of strength for aluminum cast components [7, 8].

## 2.2 Flow Forming

Flow forming is a manufacturing method that falls under the group of spin forging. This process is particularly useful when producing axisymmetric hollow or tubular parts [12]. A disk or tube of metal is formed over a mandrel, also known as former, by one or more rollers using pressure. As the rollers move, the metal deforms to the shape of the mandrel by shear deformation effectively reducing the wall thickness. A schematic of the process is shown in Figure 2.1. During flow forming the component will experience strain hardening, which will improve the grain structure and increase tensile strength [13].

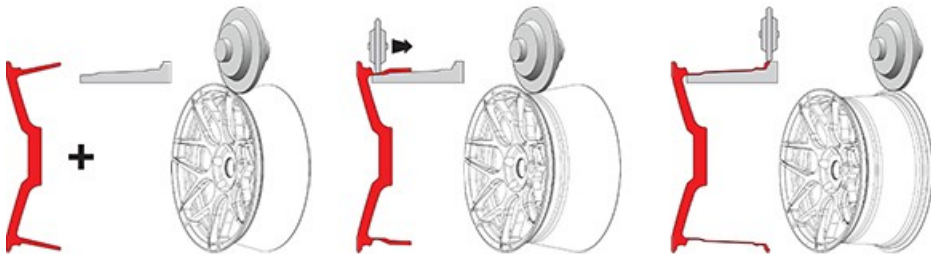


**Figure 2.1:** Flow Forming Schematic of Rim [11].

The strain hardening phenomenon is explained through dislocation-dislocation strain field interactions. As the component is cold worked, the dislocation density increases such that the motion of dislocations are hindered by the presence of other dislocations [14]. As a result, the imposed stress to deform a metal increases with cold working.

## 2.3 Heat Treatment

Heat treatment is a process that alters the mechanical properties of a metal through heating and cooling. By controlling the temperature and duration of the treatment the strength and ductility may be increased significantly. The description of precipitation hardening is described briefly and is based on Callister and Rethwisch's introductory book in Materials Science [14]. Precipitation hardening is a two-step process where the component is exposed to two distinct temperature regimes, namely solution heat treating and precipitation heat treating.

### 2.3.1 Solution Heat Treatment

During the solution heat treatment all solute atoms are dissolved to form a single phase solid solution. Regarding the hypothetical phase-diagram in Figure 2.2, an alloy with initial composition  $C_0$  is considered. As the alloy is heated to a temperature  $T_0$  within the  $\alpha$ -phase and kept there until all of the  $\beta$ -phase is completely dissolved. The specimen is then quickly quenched to temperature  $T_1$  such that no diffusion of the  $\beta$ -phase is present. At this stage, the alloy is in a non-equilibrium state consisting of a single  $\alpha$ -phase solid solution.

### 2.3.2 Precipitation Heat Treatment

The second heat treatment or precipitation heat treatment as it is called happens at an intermediate temperature  $T_2$  within the  $\alpha + \beta$ -phase region. At this temperature  $\beta$ -precipitate will form as finely dispersed particles in the supersaturated  $\alpha$ -solid solution. In the case of heat treating A356 aluminum alloy to a T6 temper, particles of  $Mg_2Si$  and  $Al_2Cu$  will precipitate [15]. After sufficient time at temperature  $T_2$ , the specimen should be cooled down to room temperature to avoid overage and loss of strength. The strengthening is explained by the forming of precipitate particles, which will increase the resistance to dislocation motion by lattice strains.

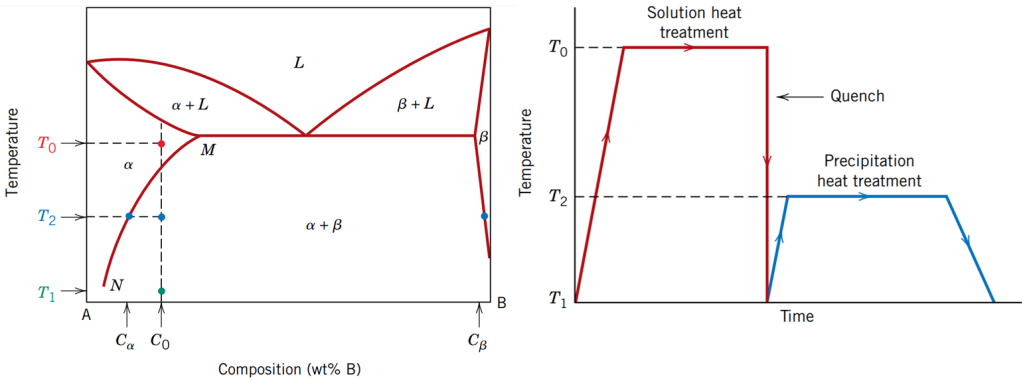


**Figure 2.2:** Phase diagram and heat treatment diagram [14].

## 2.4 Material Mechanics

This section is meant to give a brief introduction to the theory of material mechanics needed in this thesis. The section is mainly based on lecture notes by Hopperstad and Børvik [16, 17]. One should keep in mind that this topic is a substantial part of mechanics and for more in-depth discussions the reader is referred to the cited references. Fundamental mechanical principals are assumed known to the reader.

As a metal material, aluminum may be modeled by well-known relations. A constitutive elastic-viscoplastic model is suitable to describe the relation between stress and strain up to failure. Strain rate sensitivity is included through a viscous term. As temperature effects are not within the scope of this thesis the theory of an elastic-thermoviscoplastic model is not discussed. However, as shown by Hopperstad and Børvik [17], this could easily be included. Further, an appropriate failure criterion is presented since fracture is of interest.

### 2.4.1 Elastic-Viscoplastic Modelling

Assuming Johnson-Cook plasticity the yield function  $f$  can be defined. Strain rate dependencies are taken into account, which suggested by Lee [18] is important for aluminum. Associated rules are:

$$f \leq 0 \Rightarrow \text{elastic deformation}$$

$$f > 0 \Rightarrow \text{plastic deformation}$$

In the elastic domain the relation between stress and strain is defined through the Young's modulus,  $E$ , and the Poisson's ration,  $\nu$  and assumed to be isotropic.

In the plastic domain the yield function is given as:

$$f = \varphi(\sigma_{ij}) - \sigma_Y > 0 \quad (2.1)$$

The constitutive relation is given by:

$$\sigma_{eq} = \varphi(\sigma_{ij}) = (\sigma_0 + R(p)) (1 + \dot{p}^*)^C \quad (2.2)$$

where  $\sigma_0$  is the yield stress.  $R(p)$  is the work-hardening rule where  $p$  is the equivalent plastic strain.  $(1 + \dot{p}^*)^C$  is the viscous term where  $\dot{p}^* = \frac{\dot{p}}{\dot{p}_0}$  is the dimensionless plastic strain rate,  $\dot{p}_0$  being a reference strain rate and the constant  $C$  governs the rate sensitivity of the material.

Several relations for  $R(p)$  may be defined. In this thesis a five parameter Voce hardening rule is adopted, defined as:

$$R(p) = \sum_{i=1}^2 Q_{Ri} \left( 1 - e^{-\frac{\theta_{Ri}}{Q_{Ri}} p} \right) \quad (2.3)$$

This is know as the Modified Johnson–Cook (MJC) model.

### 2.4.2 Strain Rate Sensitivity

The effect of strain rate on strength properties is known as strain rate sensitivity. As the strain rate is increased, so is the resistance to deformation. When plotted, a linear relation in the log-log scale is often seen leading to an expression in its simplest form:

$$Y_f = K \dot{\epsilon}^m \quad (2.4)$$

where  $Y_f$  is the flow stress,  $K$  is the strength constant,  $\dot{\epsilon}$  the strain rate and  $m$  is the strain rate sensitivity exponent. In the constitutive relation (2.2), the effect of strain rate is taken into account by the term  $(1 + \dot{p}^*)^C$ .

### 2.4.3 Ductile Failure Criteria

Using an uncoupled damage criteria is often convenient when doing large-scale simulations of structures. The damage is assumed to evolve as a function of stress state and equivalent plastic strain, but without coupling back to the plastic

behavior. The influence of stress triaxiality,  $\sigma^*$ , on ductility is well established with a clear trend of decreasing ductility with increasing stress triaxiality. More recent studies on the influence of the Lode parameter,  $L$ , suggesting lower ductility in shear-dominated stress states than in axisymmetric stress states [17].

An uncoupled damage evolution rule can be expressed in several ways. One way to define it is to assume a failure surface which defines the failure strain  $p_f$  for stress paths with constant stress triaxiality and Lode parameter,  $p_f = p_f(\sigma^*, L)$ . Secondly one can assume a failure criterion to exist in stress space such that failure occurs when  $\eta = \eta(\sigma^*, L, \sigma_{eq}) = 0$ . Lastly, failure can be modeled by damage accumulation and failure when the damage reaches a critical value of one. The damage evolution is assumed to be driven by plastic straining amplified by a factor taking into account the stress state in terms of stress triaxiality and the Lode parameter. Equation (2.5) shows a general damage evolution where  $\chi(\sigma_{ij})$  governs the damage growth.

$$D = \int_0^p \chi(\sigma_{ij}) dp \quad (2.5)$$

### Cockcroft-Latham Failure Criterion

The Cockcroft-Latham failure criterion falls under the last definition and is based on both the stress and strain state through a plastic work formulation and is defined by:

$$D = \frac{1}{W_C} \int_0^p \max(\sigma_I, 0) dp \quad (2.6)$$

where  $W_C$  is the fracture parameter with failure at  $D = 1$ . The criterion can also be expressed in terms of invariants:

$$D = \frac{1}{W_C} \int_0^p \max\left(\sigma^* + \frac{3-L}{3\sqrt{3+L^2}}, 0\right) \sigma_{eq} dp \quad (2.7)$$

The criterion is in accordance with the effects of stress triaxiality stated earlier. It is seen that a higher triaxiality leads to faster damage evolution and consequently lower ductility. Generalized tension,  $L = -1$ , is the most detrimental followed by generalized shear,  $L = 0$ , and generalized compression,  $L = 1$  showing the effect of the Lode parameter.

### 2.4.4 Probabilistic Failure Modeling

Modeling of probabilistic failure is a challenging topic in FE-simulations. The proposed method, which was adopted by Kittilsen and Swanberg, is to give the

elements of interest an initial damage value between 0 and 1. The values are taken from a statistical distribution representing the scatter in failure strain. Throughout an analysis the damage value is accumulated from that initial value. Using this method, the varying ductility can be captured. Initial damage is pseudo-randomly distributed without correlation to neighboring elements.

One advantage of probabilistic failure modeling is to avoid overly conservative estimates, which could occur when using a minimum value for failure for all elements.

## 2.5 Ductile and Brittle Fracture

The failure mode in which the material is separated into two or more pieces due to stress is classified as a fracture. Fracture occurs when sufficient stress is applied on the atomic level to break the cohesive bonds that hold the atoms together. Theoretical derivations show that the cohesive strength of a material is approximately  $E/\pi$  [19], where  $E$  is the Young's modulus of the material. However, due to the presence of flaws acting as stress concentrations, the global strength is lowered and the fracture stress is significantly lower than the suggested theoretical cohesive strength.

The two main modes of fracture are ductile and brittle fracture. Ductile materials usually fail as the result of void nucleation, growth and coalescence. The evolution of voids initiates at inclusions or second phase particles in the metal or alloy. At the point of fracture, the material has experienced large plastic deformations. As the voids grow, the stress is concentrated to a small part of the specimen, eventually leading to a reduction in the cross section called necking and ultimately complete material failure. A schematic of ductile fracture is seen in Figure 2.3.

Brittle fracture, or cleavage fracture, is characterized by rapid crack propagation across the specimen along a particular crystallographic plane without any significant plastic deformation. If some mechanical energy is dissipated due to plastic deformation, the fracture is defined as quasi-brittle, which is typical for cast material. On the micro scale, brittle fracture is due to atomic decohesion. For cleavage to initiate, a local discontinuity ahead of the macroscopic crack must be present for the stress to exceed the bond strength. Defects may include pores, inclusions, cleavage planes, etc. and may vary in size, orientation and location. As the material is loaded, microcracks are formed in the vicinity of the initial defects which then provides local stress and strain concentration. The microcrack propagates if the stress ahead of the macroscopic crack is sufficient, causing

failure by cleavage [19]. Predicting brittle failure is challenging as the formation of microcracks throughout the material is randomly distributed, and the cracks may have different stress concentration behavior. The non-uniform nature of the cracks results in random variations in both time and location of fracture initiation. A schematic of brittle fracture is seen in Figure 2.4.

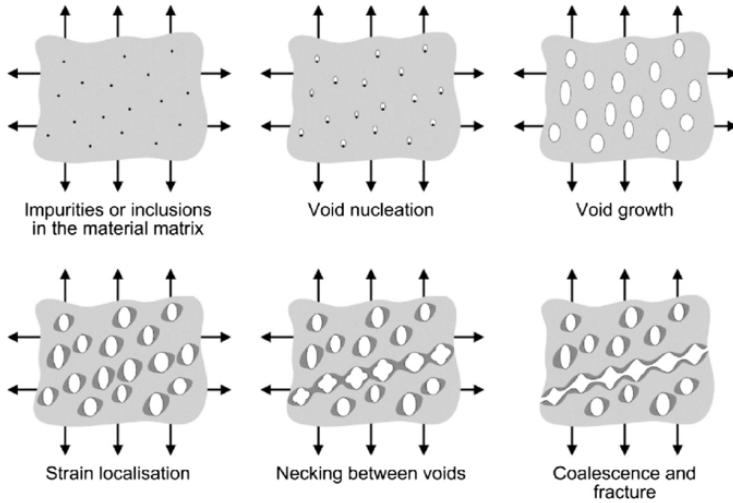


**Figure 2.3:** Schematic of Ductile Fracture showing Void Nucleation, Growth and Coalescence [20].

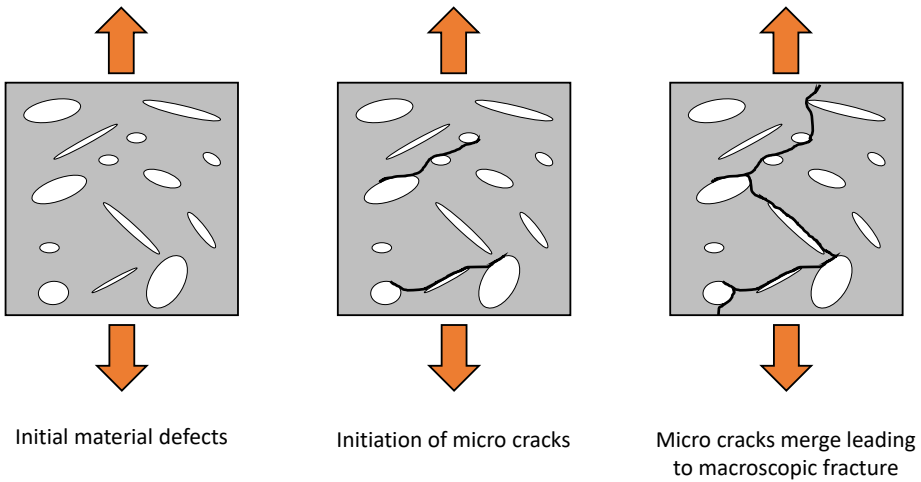


**Figure 2.4:** Schematic of Brittle Fracture.

## 2.6 Digital Image Correlation (DIC)

DIC is a technique used to measure and compute translations, displacement fields and strain fields using image tracking. Only surface values can be studied. Both two dimensional (2D) and three dimensional (3D) DIC are in general available, using one and two cameras respectively. For 2D-DIC the surface is assumed to remain planar during the experiment and the optical axis should be normal to the specimen surface. For this thesis, only 2D-DIC is needed. The presented theory is therefore focused on this. For rigid body translations, point tracking is utilized by tracking a specific marker. For field values the test specimen is coated with a speckle pattern. A subset or a mesh with contrast in greyscale values can be tracked. For instance, contrasts in test specimen and background or crash test markers can be used. Output values are functions of the image sequence and are given in the unit of pixels. A constant reference, such as a known distance between markers, is used to convert from pixel displacements to physical units.

When tracking the movement of an object in a sequence of images, conservation of optical flow is assumed. That is, the observed grayscale pattern can move and deform, but objects cannot appear nor disappear within the region of interest. That means the difference between two images can be uniquely described by a displacement field. This relative displacement field can be found by correlating the grayscale values between the two images. Measurement uncertainties are mainly due to grayscale noise of the images and will vary depending on the camera used. A typical resolution in displacements is less than 0.1 pixels, which will usually give a strain resolution of  $10^{-4}$ . In this thesis, three types of DIC are used: rigid body tracking, edge tracing and strain field computation.

To track the translation of a rigid body using DIC, a common approach is to place crash test markers on the surface of the body, shown in Figure 2.5. The translation is described as displacement in pixels of each marker with reference to the first image.

In edge tracing the location of the edges of a specimen is traced. In the test setup, the photographic technique *contre-jour* is applied, shown in Figure 2.6. In the DIC analysis, the distance, in pixels, between two edges is logged at each image. Typically the minimum distance is of interest.

If the specimen is painted with a speckle pattern a virtual mesh can be placed on the surface, shown in Figure 2.7. Tracking corner displacements and utilizing FE interpolation the strain field is obtained. Further, a vector can be placed on the specimen and elongation can be computed for all images.



**Figure 2.5:** DIC of rigid body motion with subset tracking.

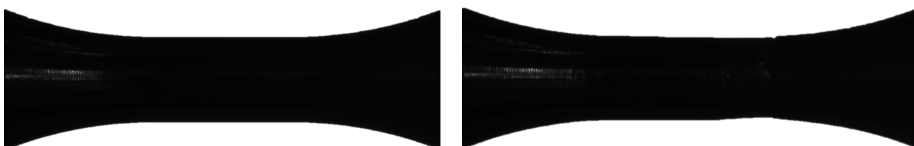


**Figure 2.6:** DIC of edge tracing.

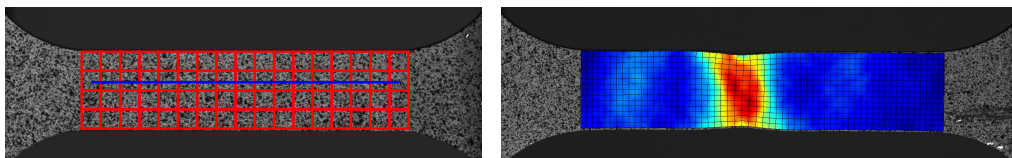


**Figure 2.7:** Exaggerated dummy mesh with vector and strain field from DIC of speckle pattern.

## 2.7 Signal Processing and Filtering

In this section, signal processing and the relevant filtering techniques used in this thesis will be presented. To estimate the rim crushing force, signal data from both DIC measurements and strain gauges must be appropriately filtered to remove noise in order to get reliable results.

### 2.7.1 Moving Average

In digital signal processing, the moving average filter is a very common filter due to its simple yet effective nature. It is an optimal filter to use when reducing random noise while retaining a sharp step response but will lack in the frequency domain as it is not able to distinguish between different frequency bands [21]. The moving average filter works by averaging a subset of the input signal. The

number of points averaged is decided by the window size used. Given  $n$  samples in the subset, the symmetrical average can be expressed as:

$$Y_j = \frac{1}{n} \sum_{i=\frac{1-n}{2}}^{\frac{n-1}{2}} y_{j+i} \quad (2.8)$$

where  $Y_j$  is the averaged output and  $y_i$  is the raw input data. For a symmetrical average,  $n$  must be odd. A moving average filter can be implemented by convolution, sweeping a normalized unit vector over the input signal. Convolution may introduce boundary effects. This can be treated by introducing extensions of the boundary conditions to the signal before convolution and subsequently disregard these domains after the convolution. The effects can be seen in Figure 2.8.

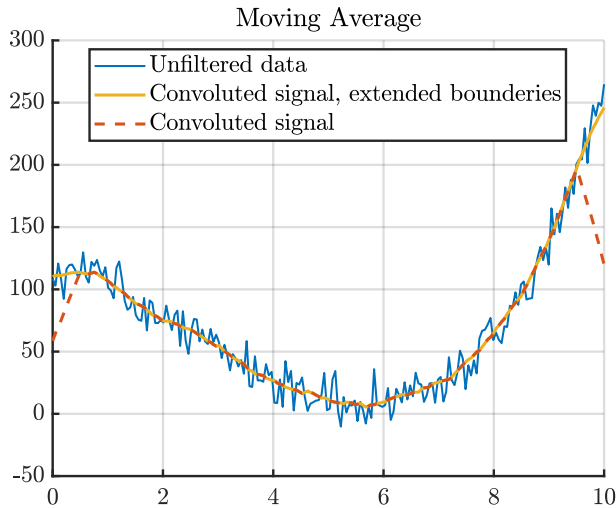


**Figure 2.8:** Example of data smoothed with a simple moving average filter.

### 2.7.2 Savitzky-Golay Filtering

Savitzky-Golay filters are well-adapted low-pass filters used for signal smoothing and noise reduction. The Savitzky-Golay filters achieve this through convolution by fitting subsets of adjacent data points to a polynomial typically of quadratic or quartic order. The polynomial is found through a least-squares fit. Contrary to many other digital filters, the Savitzky-Golay filters do not have the signal properties defined in the frequency domain and subsequently translated to the

time domain. Instead, the data smoothing happens directly in the time domain with the mentioned polynomial fittings [22].

For equally spaced data points an analytical solution to the least-squares fit can be found from tables for a range of window sizes and polynomial orders on the form of convolution coefficients. The window size corresponds to data points in the subset. The convolution coefficients can be easily calculated [23], making the smoothing process computationally inexpensive.

Consider a data set of  $n\{x_j, y_j\}$  points that is to be smoothed with  $m$  convolution coefficients  $C_i$ . The  $j^{\text{th}}$  smoothed data point,  $Y_j$  is then given by:

$$Y_j = \sum_{i=\frac{1-m}{2}}^{\frac{m-1}{2}} C_i y_{j+i}, \quad \frac{m-1}{2} \leq j \leq n - \frac{m-1}{2} \quad (2.9)$$

For instance, for a quadratic polynomial with window size = 7, the smoothed data point is given by:

$$Y_j = \frac{1}{21} (-2y_{j-3} + 3y_{j-2} + 6y_{j-1} + 7y_j + 6y_{j+1} + 3y_{j+2} - 2y_{j+3}) \quad (2.10)$$

Figure 2.9 shows an example of data smoothing with a polynomial order of 3 and a window size of 21. The data is smoothed up to the current fitting polynomial. If the sampled data are irregularly spaced, the generalized convolution coefficients

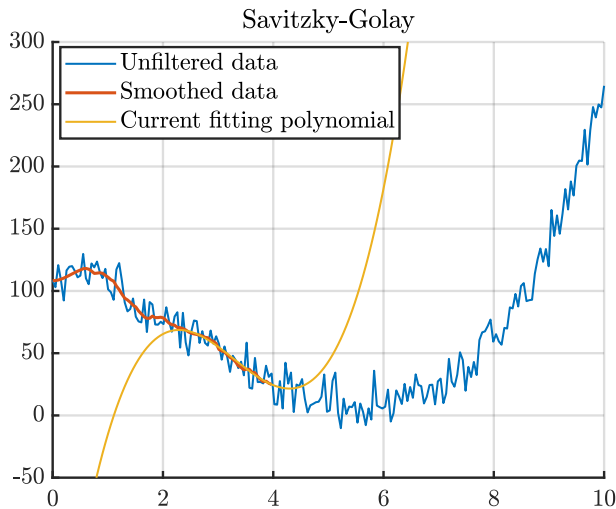


**Figure 2.9:** Example of data smoothed with a Savitzky-Golay filter.

are no longer applicable to more than one point. As a consequence, one must instead do the actual least-squares fit for each data point. For large window sizes and polynomial orders this may become cumbersome.

### 2.7.3 Digital Filtering

Whereas analog filters operate on continuous time signals from electronic devices, a digital filter is realized as an algorithm in a computer from discrete time signals to enhance or reduce certain aspects of a signal. The algorithm is on a recursive form where the filtered output is described by a linear combination of earlier input and output values [24, 25]. Digital filters operate in the frequency domain and are characterized by their transfer function. A transfer function for a linear system states the ratio between the output and input signal in the Laplace domain:

$$H(s) = \frac{Y(s)}{X(s)} = \frac{\mathcal{L}\{y(t)\}}{\mathcal{L}\{x(t)\}} \quad (2.11)$$

where  $H(s)$  is the transfer function,  $x(t)$  is the input signal and  $y(t)$  is the output signal. As such, desired outputs can be achieved by constructing a transfer function with appropriate properties. In this way digital filters are designed.

### Z-Transform

For linear, time-invariant digital filters, the transfer function can be expressed in the Z-domain which is the equivalent to Laplace-domain for discrete signals and systems. The one-sided Laplace transform of function  $f(t)$  is given as:

$$F(s) = \int_0^{\infty} f(t)e^{-ts} dt \quad (2.12)$$

whereas a Z transform is given as:

$$F(z) = \sum_{k=0}^{\infty} f[k]z^{-k}, \quad z \in \mathbf{C} \quad (2.13)$$

Subsequently, the Z-transform of a transfer function can be expressed as:

$$H(z) = \frac{Y(z)}{X(z)} = \frac{b_1z^{-1} + \dots + b_nz^{-n}}{1 + a_1z^{-1} + \dots + a_nz^{-n}} \quad (2.14)$$

where the rightmost expression is the transfer function expressed as linear constant-coefficient difference equation made causal. By rearranging Equation (2.14), the output can be expressed as:

$$Y(z) = -(a_1z^{-1}Y(z) + \cdots + a_nz^{-n}Y(z)) + b_1z^{-1}X(z) + \cdots + b_nz^{-n}X(z) \quad (2.15)$$

By using its time delay property and inverse transform [24], the discrete recursive form of the output is found to be:

$$y[k] = -a_1y[k-1] - \cdots - a_ny[k-n] + b_1x[k-1] + \cdots + b_nx[k-n] \quad (2.16)$$

As stated earlier, the current output value,  $y[k]$ , is now expressed as a linear combination of previous output and input values, which makes it suitable for calculating using a computer. Many digital filters are based on the fast Fourier transform to extract the frequency content and alter it before going back to the time domain by inverse fast Fourier transform.

For finite impulse response (FIR) filters the Z transform simplifies to only include the numerators with coefficients  $b_i$ . An example of an FIR filter with  $n = 101$  is presented later and has coefficients given in Figure 2.10.

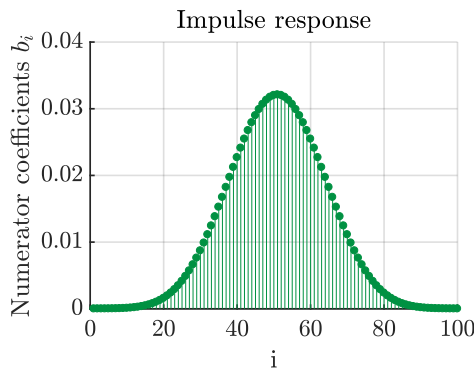


**Figure 2.10:** Input coefficients.

## Zero Phase Filter

Zero phase filters exploit time-reversal properties of the discrete-time Fourier transform (DTFT) to filter forward and backward in time to create a filter with no phase distortion. The time reversal property of the DTFT can be expressed as:

$$x[n] \xrightarrow{\text{DTFT}} X(e^{j\omega}) \iff x[-n] \xrightarrow{\text{DTFT}} X^*(e^{j\omega}) \quad (2.17)$$

where  $X(e^{j\omega})$  is the DTFT of signal  $x[n]$  and  $X^*(e^{j\omega})$  is the complex conjugate to  $X(e^{j\omega})$ . Figure 2.11 shows the block diagram of a zero phase filter:

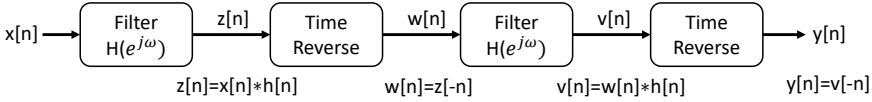


**Figure 2.11:** Block diagram of a zero phase filter.

where  $h[n]$  is the impulse response function.

In the frequency domain the steps correspond to:

1.  $Z(e^{j\omega}) = H(e^{j\omega})X(e^{j\omega})$
2.  $W(e^{j\omega}) = Z^*(e^{j\omega}) = H^*(e^{j\omega})X^*(e^{j\omega})$
3.  $V(e^{j\omega}) = H(e^{j\omega})W(e^{j\omega}) = |H(e^{j\omega})|^2 X^*(e^{j\omega})$
4.  $Y(e^{j\omega}) = V^*(e^{j\omega}) = |H(e^{j\omega})|^2 X(e^{j\omega})$

which gives an effective frequency response,  $H_{eff}(e^{j\omega}) = |H(e^{j\omega})|^2$ , that is real and positive which implies zero phase distortion but with a squared gain of the filter used.

## 2.8 Explicit Finite Element Method

Explicit FEM is a numerical technique used for solving the dynamic equations of motion in the time domain. At the beginning of the simulation, initial conditions are defined. The time domain is discretized and the dynamic equations are integrated forward in time. Nodal accelerations are solved directly without the need for iterations. Conceptually, from accelerations, velocities and displacements are found. From displacements comes strains and from strains comes stresses. This is similar to static FEM.

Explicit FEM can easily be derived by the use of the principle of virtual power (PVP) [26]. The semi-discretized equations of motion are obtained:

$$\mathbf{M}\ddot{\mathbf{r}} = \mathbf{R}^{int} - \mathbf{R}^{ext}(\mathbf{r}) \quad (2.18)$$

Time integration is performed using the central difference scheme. The inverse of the mass matrix is needed and a lumped mass matrix is applied to reduce CPU-expenses. The main advantage of this algorithm is that it is explicit. However, the main disadvantage is that it is only conditionally stable, and a small time step is needed to obtain a stable solution. The critical time step can be calculated from:

$$\Delta t \leq \alpha \min\left(\frac{h_e}{c}\right) \quad (2.19)$$

where  $c = \sqrt{\frac{E}{\rho}}$  and  $\alpha$  is the Courant number which accounts for destabilizing effects of the nonlinearities of the problem.  $h_e$  is the element length. Observe that for a finer mesh the number of elements increases *and* the element length decreases, which again decreases the stable time step. Both contribute towards more CPU-time needed to complete the analysis.



## Chapter 3

# Rim Properties and Material Characterization

### 3.1 Properties

The provided rim for this thesis is the Q7 ALY58988 10-spoke rim from Audi, the same rim used by Kittilsen and Swanberg in their master's thesis, coming from the same manufacturer and batch. No information about the manufacturing process has been disclosed by the rim producer, but through thoughtful assumptions and limited information from Audi, Kittilsen and Swanberg were able to characterize the relevant properties of the rim.

The rim is comprised of two main parts, the spokes and rim bed. There are 10 spokes, five short and five long. The size of the rim is given to be 20 by 9 inches. These measurements are given by the diameter of the tire they accept in combination with its width. Closer inspections of the rim shows dimensions to be 547 by 255 mm, or 21.4 by 9.9 inches at its largest with an approximate weight of 15.7 kg. The rim is seen in Figure 3.1.

The preform, including the entire spoke section, of the rim is produced using the LPDC process described in Section 2.1.1, while the rim bed is flow formed. In the casting process molten aluminum is pushed into the die before cooling and solidification. During the solidification of the metal, shrinkage porosity and other defects may occur in the specimen. Parts subjected to higher temperature gradients throughout the cross section are especially susceptible to shrinkage porosity and the mechanical properties may therefore vary accordingly. When the preform has cooled down, it will undergo the process of flow forming to create the final

shape of the rim bed. During this process the rim bed material will experience strain hardening increasing the strength of the material [7]. This is why the spoke part and rim bed part of the rim exhibit noticeably different mechanical properties. As a final process the rim will be subjected to heat treatment which further increases the yield strength and ductility. A study conducted by Pio [15] showed an increase of 106% and 214% in yield strength and ductility respectively for cast A356 aluminum heat treated to a T6 temper. All together these processes contribute to higher strength and a potential lower weight of each wheel which is important in automotive design.



**Figure 3.1:** Front and side view of the Audi Rim.

## 3.2 Previous Material Characterization

This section is based on the master's thesis written by Kittilsen and Swanberg and summarizes their extensive work to characterize the material properties of the aluminum rim provided by Audi. The thesis had a predominant focus on the characterization of the global systematic and local random variations in material properties due to the casting process. Based on their information from Audi and assumptions about the manufacturing process, the material properties were expected to vary throughout the rim geometry. For material characterization, the

defects may be incorporated by considering them as initial material damage which will decrease the local material ductility. As the global systematic and local random variations vary within each component, a probabilistic distribution of initial damage is given to represent the defects. The development and incorporation of such damage distribution were believed to be important for proper modeling and was therefore a significant part of the thesis by Kittilsen and Swanberg.

### 3.2.1 Material Testing

During the study of Kittilsen and Swanberg, six rims were used for experimental testing to analyze the material behavior. All rims were provided by Audi and came from the same production batch sharing the same geometry. Of the six, two were used for material tests and four for component tests. The material tests conducted were a Vicker's hardness test, optical microscope study and uniaxial tensile tests with both UT60 and UT90 specimens.

#### Microscope Study

An optical microscope was used to inspect grain size and particle distribution from both specimens originating from a spoke and corresponding part of the rim bed. The inspection showed a significantly smaller grain size in the rim bed, which is due to a higher local cooling rate in the casting and heat treatment process as the rim bed is thinner than the spoke section. This prevents diffusion leading to smaller solidified grains [27]. Lower grain size will often lead to an increase in ductility and yield strength of the material [14, 28]. In addition, the grain

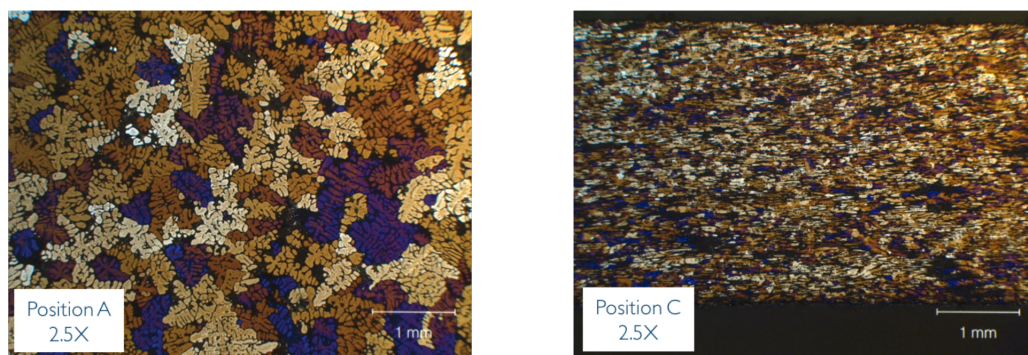


**Figure 3.2:** Grain structure in spoke part (A) and rim bed (C), taken from Kittilsen and Swanberg.

structure of the rim bed is more complex as it is strained in the direction of the flow forming. The distortion and smaller grain size can be seen in Figure 3.2. Thus, in this part of the rim, greater tensile strength is obtained.

### Tensile Tests

In order to determine the presence of global systematic variance in material behavior, a total of 34 UT60 tensile tests were machined from the two rims and extracted from both the spoke part and rim bed. In addition, a specimen from an extruded component of a similar alloy and heat treatment (AlSiMg-T6) was tested to compare with the cast rim. Their findings showed a clear difference in the behavior between the spoke part and rim bed. The rim bed specimens showed more ductile behavior with a higher ultimate tensile strength compared to the spokes. Specimens from the spokes showed high variation in ductility with a fracture strain ranging from 1.4% to 7.9% due to pores and defects. In addition, the specimens from the Audi rims showed significantly higher ultimate strength than the specimen from the extruded component. A comparison of a spoke and rim bed specimen alongside the extruded component is shown in Figure 3.3. A concern was raised regarding the possibility that grain size in the spokes was affecting the results of the small UT60 specimens. By testing with larger UT90 specimens, the grain size effect was deemed insignificant as test results showed similar variation in ductility, confirming the previous results from the UT60 specimens.

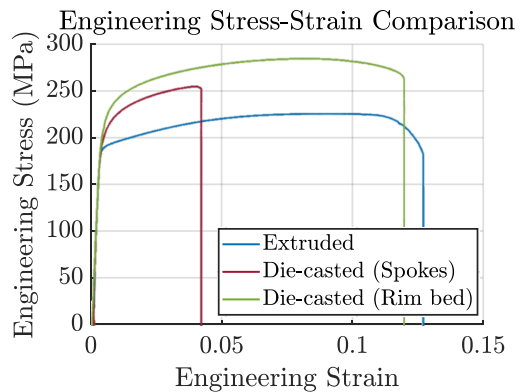


**Figure 3.3:** Stress vs. Strain curves from tensile tests [5].

### Hardness Test

The goal of the hardness test was to investigate the variation in yield strength in different areas of the rim. Yield strength can be estimated based on the hardness value by multiplying with a conversion factor. To get reasonable results, a conversion factor of 2.1 was chosen. The yield strength was found to vary from 148.6 MPa to 214.7 MPa with a slight linear increase moving from the spokes to

the rim bed. This was in accordance with the tensile tests, but the difference was not as predominant. Large local variations in the hardness test were also observed and are believed to be due to measurement inaccuracies and the grain structure. The grain size in the spoke part was measured to 1 mm by microscopy and the indent-diameter was 0.3. This meaning the indentation could be on a single grain or between grains leading to varying results.

### 3.2.2 Global Variation

Kittilsen and Swanberg systematically tested specimens from two different rims to characterize their mechanical properties and investigate global and local variations within the rim. One rim was found to have a generally higher ultimate tensile strength and lower ductility than the other. As one could expect from the manufacturing process, a substantial variation in fracture strain was found in the spoke section. Global systematic variations between the spoke part and rim bed was also found, mainly in ductility but also the strength to some degree. The rim bed specimens generally had higher strength and ductility than the spoke specimens. Due to their limited sample size, no definite conclusions to the presence of systematic variations between short and long spokes could be made. As a result of their material characterization, the spokes and rim bed are considered as two different materials in numerical simulations. Local variations are especially observed for the spokes, and as such, a probabilistic approach was believed to be necessary to capture the correct material behavior and initial damage.

### 3.2.3 Material Characterization

The effect of strain rate was not accounted for when describing the stress vs. strain behavior of the rim. However, strain rate dependency of aluminum alloys have been researched and are found to be present. To accurately predict the tensile properties of LPDC A356 aluminum alloy, the constitutive should take into account strain rate sensitivity [18]. Nevertheless, Kittilsen and Swanberg chose to describe the material with a two-term Voce hardening law, Equation (2.3), which is commonly used when modeling aluminum alloys [8, 29].

Based on the tensile tests described in Section 3.2.1, the Voce parameters were fitted to the stress vs. strain curves for both spokes and rim bed. The parameters used by Kittilsen and Swanberg are listed in Table 3.1.

The Voce parameters were chosen to best represent the response from specimens of both rims. The failure parameter,  $W_c$ , is strongly sensitive to the hardening curve

chosen as it is computed through the integration of the maximum principal stress with regards to equivalent plastic strain up to failure, expressed in Equation (2.6). Choosing a representative hardening law for the material is therefore important.

Section	$\sigma_0$ (MPa)	$Q_{R1}$ (MPa)	$\theta_{R1}$ (MPa)	$Q_{R2}$ (MPa)	$\theta_{R2}$ (MPa)	$W_c$ (MPa)
Spokes	181.3	84.2	1 321.9	47.3	8 381.6	18.57*
Rim bed	208.2	86.2	1 534.4	30.8	7 379.7	39.0

**Table 3.1:** Material parameters found by Kittilsen and Swanberg.  
\*Probabilistic approach

### Rim Bed

For the rim bed, due to the manufacturing process, local variations in defects are insignificant to the material behavior. As such, an average failure parameter was suggested based on the experimental results. A direct average gave a value of 46.5 MPa for  $W_c$ . This was deemed too high as a few outliers greatly affected the value. Instead, an average value for  $W_c$  was calculated from the representative hardening law given by the parameters presented in Table 3.1, resulting in a value of 39.0 MPa. It should be noted that the representative hardening curve is based on the results of only 10 rim bed specimens. Larger sample size would likely give a more accurate result.

### Spokes

In order to describe the random character of the ductility in the spokes as described earlier, the section has a failure parameter corresponding to the maximum experimental value but with elements assigned an initial damage taken from a suitable probability distribution. From the tensile tests the failure parameter ranged from  $W_c^{min} = 2.29$  MPa to  $W_c^{max} = 18.57$  MPa. A damage parameter is defined by normalizing the failure parameter corresponding to Equation (2.6):

$$D = \frac{W}{W_c^{max}} \quad (3.1)$$

$W$  is the instantaneously measured Cockcroft-Latham parameter in the element and  $W_c^{max}$  is the maximum critical Cockcroft-Latham parameter. The damage parameter is accumulated as elements are plastically strained, and the element is

set to fail when  $D=1$  in all integration points of the element. At this point, the element is eroded, deleted, from the mesh in numerical simulations. The variation in ductility is taken into account by assigning initial damage to elements:

$$D_i = 1 - D_c \quad (3.2)$$

The initial damage was distributed to the spoke elements by a normal distribution with expected value,  $\mu = 0$ , and standard deviation  $\sigma = 0.25$ . A MATLAB script generates initial damage from the distribution and generates an `.inp` file with the initial damage and element numbering. An Abaqus subroutine was applied which calculates and updates the damage in each element. Figure 3.4 shows where the two material characterizations are assigned to the rim in the Abaqus model.

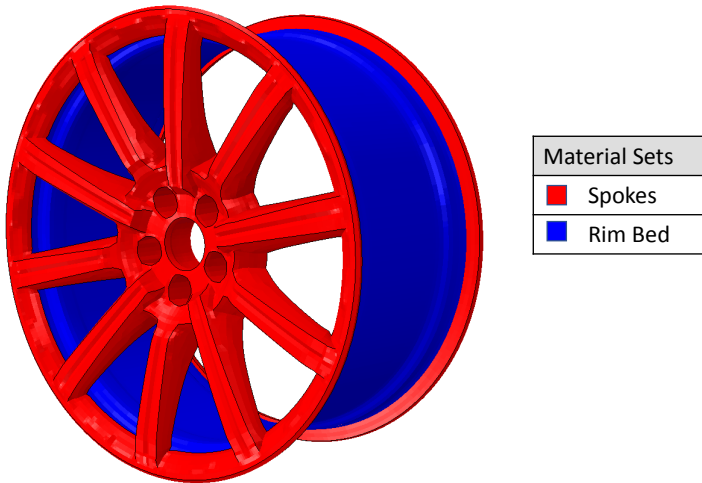


**Figure 3.4:** FE-model with material sections.

### 3.3 New Material Tests

To assess the previously determined material characterization and ensure its applicability in this year’s study, new material tests have been conducted. The tests are not as quantitative as those carried out by Kittilsen and Swanberg. Both tensile specimens and Split-Hopkinson Tension Bar (SHTB) specimens are tested. Tensile tests are used to determine quasi-static parameters, while SHTB tests are used to determine strain-rate sensitivity. The latter is suggested by Lee [18] to be of importance in numerical modeling of rims. However, this was not assessed by Kittilsen and Swanberg and is a new contribution in this year’s study. All samples were taken from only one rim. This was done by the intention to save as many rims as possible for later dynamic component testing.

A total number of six tensile and ten SHTB specimens were cut and machined. The location of where the specimens were taken from is shown in Figure 3.5. Three tensile specimens were taken from the spokes and three were taken from the rim bed. This was considered to be enough to assess the previously determined material characterization. However, the statistical fracture property cannot be determined from this number of samples. Further, all SHTB specimens were taken from spokes. Due to the geometrical limitation, they could not be taken from the rim bed. The specimen numbering system is adopted by Kittilsen and Swanberg and extended to suit this study.

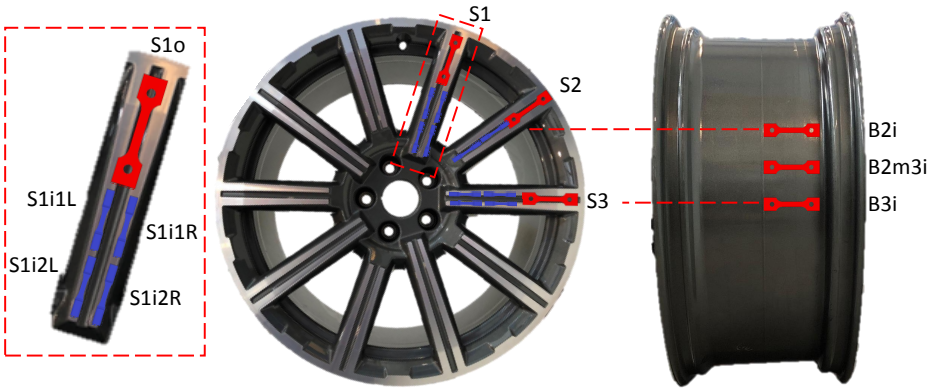


**Figure 3.5:** Where specimens are taken from.  
 Red = Tensile specimens.  
 Blue = SHTB specimens.

### 3.3.1 Tensile Tests

All tested uniaxial tensile specimens were UT60 and tested using the same setup used by Kittilsen and Swanberg. Exact geometry can be found in Figure 3.6. The experimental setup is shown in Figure 3.7. A 10 kN Instron load cell was used. Both ends were connected to the testing machine using pins. One end was fixed while the other was pulled. The machine applied a displacement at a rate of 0.6 mm/min, i.e., a strain rate of  $0.03 \text{ min}^{-1}$ . All tests were carried out until fracture.

Prior to testing a black and white speckle pattern was painted on the specimens to allow precise capturing of strains using DIC. The cameras were set to record one image every second. The software eCorr v4.0 was used to perform DIC analyses. A mesh size of 25 pixels was applied and a vector was defined to capture elongation.

The engineering stress vs. strain curves from this year's tests, as well as the results from Kittilsen and Swanberg, are shown and compared in Figure 3.8. Results from spokes and rim bed are plotted separately. R1 and R2 are respectively rim 1 and rim 2 tested by Kittilsen and Swanberg.

Seen from Figure 3.8a, the results from the three spoke specimens are not in accordance with previous tests. Yielding occurs at a higher stress level, hardening is more influential for lower strains and fracture occurs on average at a lower strain. One should remember that these statements are based on *only* three tests, and the possibility that these tests are not representative should be kept in mind. However, in later numerical studies, material parameters will be assessed.

From Figure 3.8b, a similar comparison for the rim bed is shown. Clearly seen, for the rim bed, the new material tests are in accordance with the previous tests. The previously defined material characterization for the rim bed is therefore kept as is without further investigation.

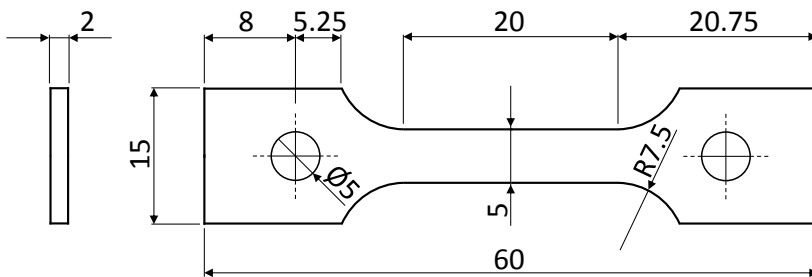


**Figure 3.6:** UT60 dimensions.

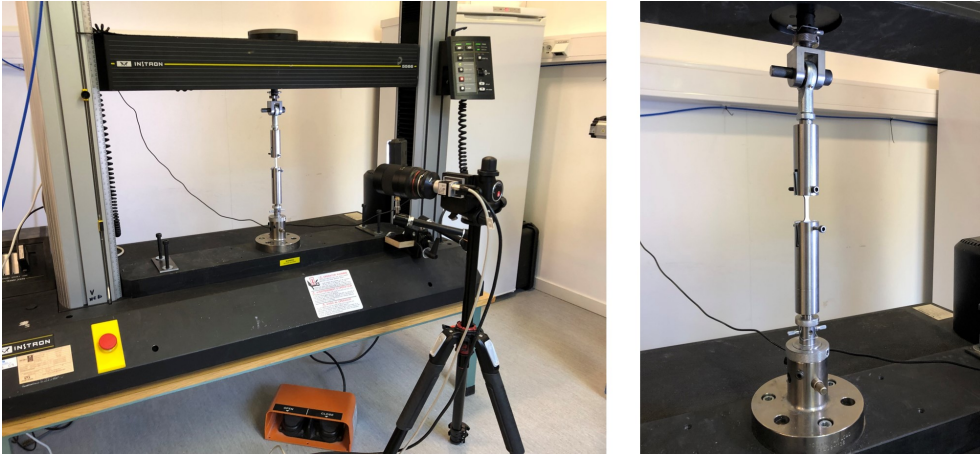


Figure 3.7: Experimental setup for tensile tests (UT60).

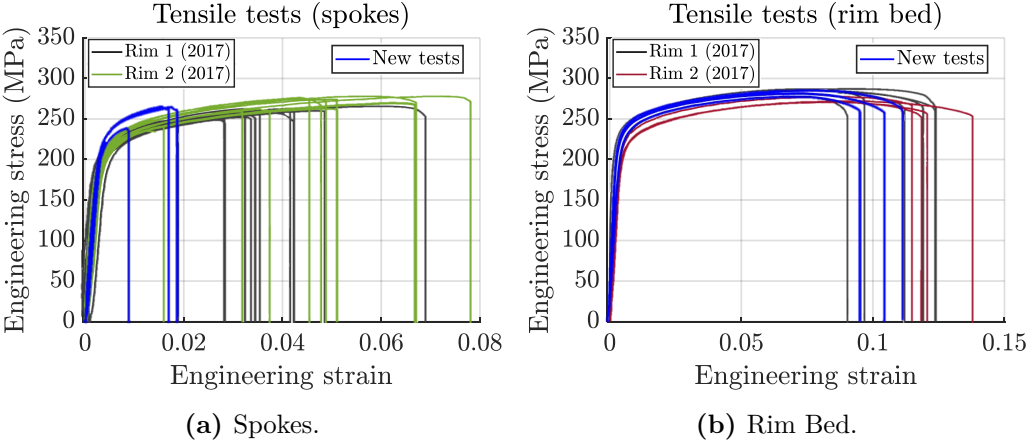
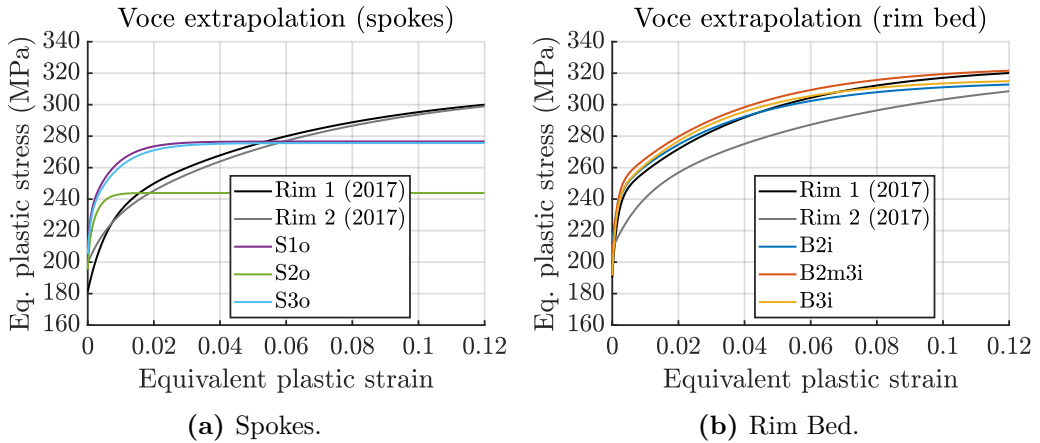


Figure 3.8: Engineering stress vs. strain curves of new tests compared to results found by Kittilsen and Swanberg.

Based on the experimental results shown in Figure 3.8 Voce parameters, taken by Equation (2.3), are fitted using the least square method. The extrapolation, beyond necking, for all six tensile tests are shown in Figure 3.9. In the same figure, the representative material model for rim 1 and rim 2 developed by Kittilsen and Swanberg are shown.

From Figure 3.9a the Voce extrapolation for the spokes from the new material tests clearly deviates from the previous ones. Yielding is increased and for low strains, the material hardens more. A problematic observation is the flat extrap-



**Figure 3.9:** Voce extrapolation, new tests compared to results found by Kittilsen and Swanberg.

olation after about 0.02 equivalent plastic strain. This is explained by the fact that necking occurred at less than 0.015 equivalent plastic strain for all three spoke tests. Thus, the least square fit is based on this small region only, and extrapolation far beyond necking is associated with considerable uncertainty.

The Voce extrapolation for the samples taken from the rim bed is shown in Figure 3.9b. In these tests, necking occurred at strains at about 0.07. Thus, a larger region for the least square fit, and a better extrapolation. The new material tests are in accordance with the material characterization by Kittilsen and Swanberg.

The Voce parameters describing all the curves in Figure 3.9 are listed in Table 3.2 and Table 3.3.

	$\sigma_0$ (MPa)	$Q_{R1}$ (MPa)	$\theta_{R1}$ (MPa)	$Q_{R2}$ (MPa)	$\theta_{R2}$ (MPa)
R1 (2017)	181.3	47.3	8 372.1	84.2	1 323.5
R2 (2017)	199.5	23.0	3 637.7	91.3	1 383.7
S1o	209.1	20.2	26 762.1	47.3	6 429.6
S2o	195.3	12.3	27 579.0	36.4	14 204.5
S3o	205.0	23.1	28 634.4	47.5	5 565.7

**Table 3.2:** Voce parameters of spoke section.

	$\sigma_0$ (MPa)	$Q_{R1}$ (MPa)	$\theta_{R1}$ (MPa)	$Q_{R2}$ (MPa)	$\theta_{R2}$ (MPa)
R1 (2017)	190.1	49.7	33 944.5	85.4	2 007.9
R2 (2017)	208.2	30.8	3 685.9	86.2	1 181.1
S1o	211.4	31.5	19 150.5	72.1	2 090.6
S2o	202.6	44.9	33 625.0	77.1	2 079.1
S3o	191.4	49.9	43 232.8	75.2	2 403.2

Table 3.3: Voce parameters of rim bed section.

### 3.3.2 Split-Hopkinson Tension Bar

The Split-Hopkinson tension bar (SHTB) is a commonly used test setup for high strain rate testing. The test can achieve strain rates of the order  $10^2$ - $10^4$  s<sup>-1</sup> and is therefore well suited for testing material strain rate sensitivity.

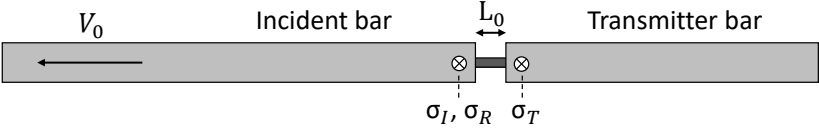


Figure 3.10: Simple Split-Hopkinson tension bar schematic [30].

Figure 3.10 shows a simplified SHTB setup where the test specimen is wedged between an incident bar and a transmitter bar. A closer view of the test specimen along the stress pulses is shown in Figure 3.11. Incident and reflected stress are measured through strain gauges at the incident bar while transmitted stress is measured at the transmitter bar.

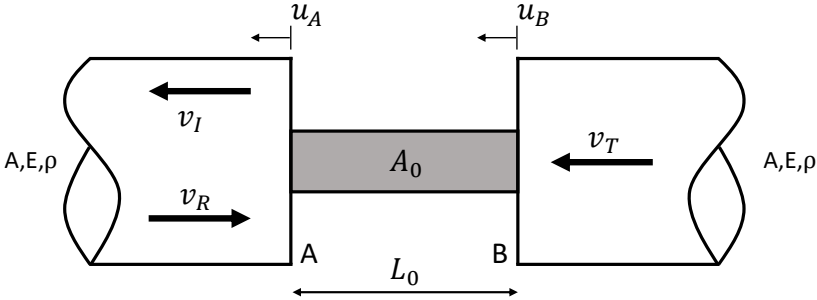


Figure 3.11: Schematic of test specimen and stress pulses.

As  $u_A > u_B$ , the test specimen will be subjected to tension and undergo plastic

deformation. The average stress, strain and strain rate of the test specimen can be calculated through simple relations and assumptions. Nominal strain is given as:

$$e_s = \frac{u_A - u_B}{L_0} \quad (3.3)$$

with strain rate:

$$\dot{e}_s = \frac{\dot{u}_A - \dot{u}_B}{L_0} = \frac{(v_I - v_R) - v_T}{L_0} \quad (3.4)$$

Using

$$\begin{aligned} v_I &= c \cdot e_I \\ v_R &= c \cdot e_R \\ v_T &= c \cdot e_T \\ c &= \sqrt{E/\rho} \end{aligned}$$

where  $c$  is the characteristic wave speed in the bars, Equation (3.3) can be rewritten as:

$$\dot{e}_s = \frac{c}{L_0}(e_I - e_R - e_T) \quad (3.5)$$

The specimen is subjected to forces at both boundaries A and B:

$$P_A(t) = EA(e_I + e_R) \quad P_B(t) = EAe_T \quad (3.6)$$

The average stress can be calculated:

$$\sigma_s = \frac{P_A + P_B}{2A_0} = \frac{EA}{2A_0}(e_I + e_R + e_T) \quad (3.7)$$

Assuming  $P_A = P_B$  gives  $e_T = e_I + e_R$ . In actual experiments, stress waves will reflect in the specimen and it will only obtain a quasi-equilibrium after some time where  $P_A \approx P_B$ . Therefore, the initial part of the stress vs. strain curve does not reflect the actual material behavior. Equations (3.7) and (3.5) reduce to:

$$\sigma_s = \frac{EA}{A_0}e_T \quad (3.8)$$

$$\dot{e}_s = -\frac{c^2}{L_0}e_R \quad (3.9)$$

Integrating the strain rate gives the average strain of the specimen:

$$e_s = -\frac{2c}{L_0} \int_0^t e_R dt \quad (3.10)$$

### Calculating Strain Rate Sensitivity

The objective of the Split-Hopkinson tests is to calculate the strain rate sensitivity constant,  $C$ , from Equation (2.2). The full equation becomes:

$$\sigma_{eq} = \left( \sigma_0 + \sum_{i=1}^2 Q_{Ri} \left( 1 - e^{-\frac{\theta_{Ri}}{Q_{Ri}} p} \right) \right) (1 + \dot{p}^*)^C \quad (3.11)$$

To do so, tests at different strain rates must be done as well as several quasi-static tests. From the quasi-static reference, one can determine the Voce parameters for the SHTB specimens. From these results, the true stress vs. logarithmic plastic strain can be plotted for different values of true plastic strain and the true equivalent stress can be fitted to Equation (3.11) to find  $C$  with a least square method.

#### 3.3.3 SHTB Tests

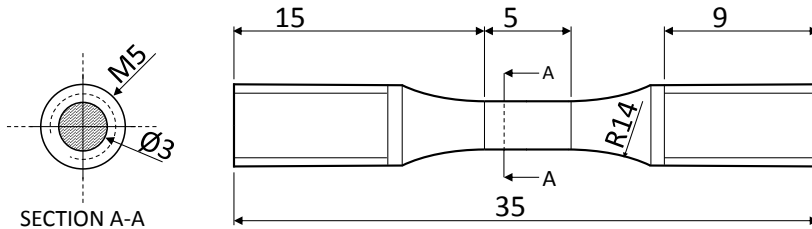


**Figure 3.12:** SHTB 3 mm dimensions.

The geometry of the specimens tested for the Split-Hopkinson tests is shown in Figure 3.12. As previously written, ten specimens were machined, all from spokes. However, during testing, one specimen was accidentally destroyed before testing. The remaining nine were divided into three groups. Three samples were tested at strain rate equal to  $5 \cdot 10^{-4} \text{ s}^{-1}$  for quasi-static reference, three around  $300 \text{ s}^{-1}$  and three around  $900 \text{ s}^{-1}$ .

#### Quasi-Static Tests

To determine the Voce parameters taken in the estimation of the strain rate sensitivity parameter, three quasi-static tests were performed using the same 10 kN Instron load cell and machine as the UT60 tests. For the Split-Hopkinson tests,

the clamping was changed to fit the cylindrical specimens and the displacement speed was lowered to give a strain rate of  $5 \cdot 10^{-4} \text{ s}^{-1}$ . Edge tracing using DIC was utilized to capture strains precisely.

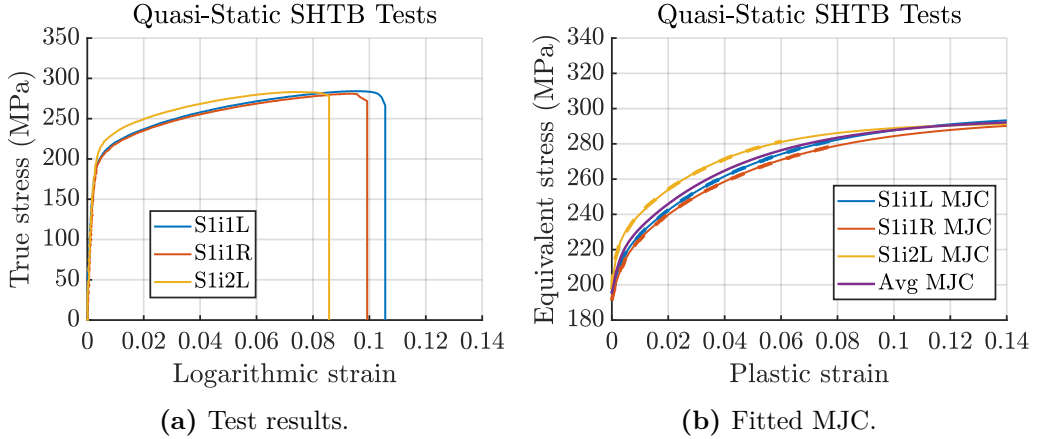


**Figure 3.13:** Quasi-Static Testing of SHTB Specimens.

Test	$\sigma_0$ (MPa)	$Q_{R1}$ (MPa)	$\theta_{R1}$ (MPa)	$Q_{R2}$ (MPa)	$\theta_{R2}$ (MPa)
S1i1L	194.4	18.3	6 448.8	84.8	1 822.7
S1i1R	191.8	19.7	5 718.4	83.2	1 740.8
S1i2L	199.0	22.6	1 3981.0	70.6	2 164.4
Average	195.1	20.2	8 490.7	79.5	1 937.4

**Table 3.4:** Quasi-Static reference Voce parameters.

Figure 3.13a shows the true stress vs. strain curves of the quasi-static tensile SHTB specimen tests. From this, the equivalent plastic stress up to necking can be extracted. In Figure 3.13b the equivalent stresses are plotted with a dashed line while the full line represents the curve fitted Voce extrapolation beyond necking for each test along with an average. Characteristic values are listed in Table 3.4. Specimen S1i2R was destroyed prior to testing. Consequently, no testing was performed on this specimen.

## Dynamic Tests

In total, six dynamic SHTB tests were carried out at elevated strain rates in order to determine the strain rate sensitivity of the cast aluminum. The test



Figure 3.14: Dynamic SHTB setup.

setup is shown in Figure 3.14. The tension bar is made of steel with a diameter of 10.00 mm. The Young’s modulus is 200 GPa resulting in a wave speed of 5100 m/s. All specimens are taken from the rim bed and are therefore not cold worked like the rim bed. Using Equations (3.8), (3.9) and (3.10), the stress, strain and strain rate is estimated.

Figure 3.15a shows the true stress vs. strain curves of the dynamic SHTB tests. Testing of specimen S2i1 was not performed correctly and is therefore disregarded when estimating the strain rate sensitivity coefficient. From Figure 3.15, it is observed that the equivalent plastic strain is higher than the quasi-static tests

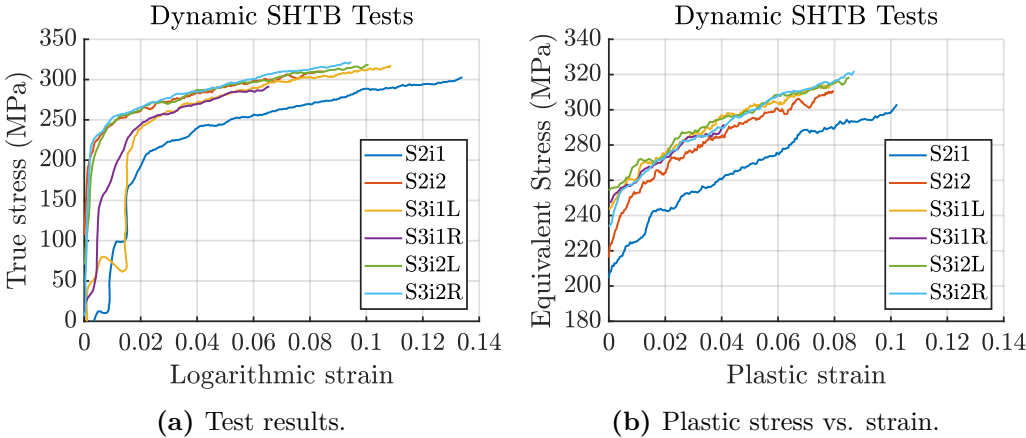


Figure 3.15: Dynamic Testing of SHTB Specimens.

for the same plastic strain levels. This suggests that the material is strain rate dependent and that the stress increases for increased strain rate. To take this into account in the material model, an average strain rate sensitivity constant  $C$  is estimated based on the tests.

To do so, Equation 3.11 is normalized with the quasi-static reference stress at several strain rates taken from the average Voce parameters in Table 3.4. The strain rate sensitivity constant is then fitted with regards to Equation (3.12) with a least squares method for each strain rate.

$$\frac{\sigma_{eq}}{\left(\sigma_0 + \sum_{i=1}^2 Q_{Ri} \left(1 - e^{-\frac{\theta_{Ri}}{Q_{Ri}} p}\right)\right)} = \left(1 + \frac{\dot{p}}{\dot{p}_0}\right)^C \quad (3.12)$$

The quasi-static reference strain rate used is  $5 \cdot 10^{-4} \text{ s}^{-1}$ . Taking the stress and plastic strain rate at plastic strains ranging from 1% to 6% results in values plotted in Figure 3.16. The values are also listed in Appendix A, Table A.1.

It is clear that the material taken from the spoke section of the rim is strain rate dependent. The lines plotted corresponds to the equivalent stress from Equation (3.11) with the corresponding  $C$  for each strain level. As the data is presented with a log-scale for the x-axis, the plot appears linear with a slope equal to the

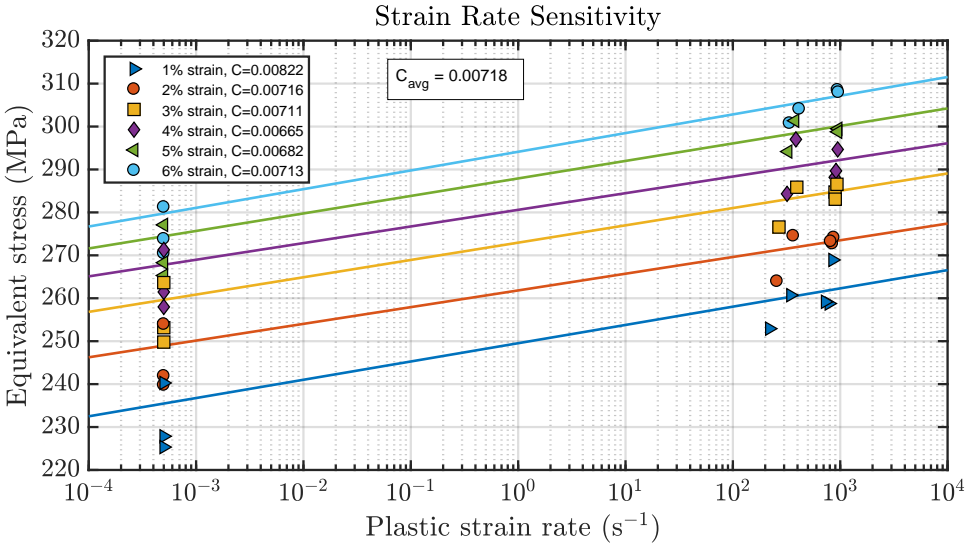


**Figure 3.16:** True stress vs. logarithmic plastic strain at elevated strain rates.

non-normalized  $C$ . The sensitivity constant is averaged for the sampled strains and a value of  $C = 0.00718$  is obtained. This value fits well within values found from tests by Chen et al. [29]. Various aluminum alloys in T6 temper were tested and a  $C$  varying from 0.0015 to 0.0116 was found.

### 3.4 Final Material Characterization

Based on the new material tests, an updated material characterization was decided to be implemented in numerical simulations. The yield stress of the spokes has been increased from 181.3 MPa to 200 MPa while the hardening parameters remain the same. Strain rate sensitivity is included using  $C = 0.00718$  for the spoke section. As strain rate sensitivity of aluminum has been observed in studies before, a small sensitivity is included for the rim bed section as well.  $C = 0.001$  was chosen as a lower bound.

Section	$\sigma_0$ (MPa)	$Q_{R1}$ (MPa)	$\theta_{R1}$ (MPa)	$Q_{R2}$ (MPa)	$\theta_{R2}$ (MPa)	$W_c$ (MPa)	$C$ (-)
Spokes	200.0	84.2	1 321.9	47.3	8 381.6	18.57*	0.00718
Rim bed	208.2	86.2	1 534.4	30.8	7 379.7	39.0	0.001

**Table 3.5:** Final material parameters.  
\*Probabilistic approach

## Chapter 4

# Force Estimation Scheme

### 4.1 Test Design

A concept for dynamical testing of cast aluminum rims has been developed and is described in Martinsen's thesis. The concept is designed to be used the kicking machine [31] available at NTNU. To estimate the rim crushing force, a force estimation scheme was proposed. In this chapter, the estimation scheme is presented including modifications from the concept initially developed. The purpose of the dynamic tests is to measure the crushing force acting on the rim as a function of the rim displacement. In practice, the crushing force and the displacement are both functions of time, and estimation may therefore be carried out in the time domain before being mapped to the displacement domain.

Due to the rim geometry being fundamentally unsymmetrical, extensive work has been put into the development of a test setup which takes this into account. Traditional setups, like what may be used for testing of crash boxes, for instance, described by Langseth and Hopperstad [32], is not appropriate to apply in this study. The impact area of the rim is larger than the frontal area of the load cells available, and thus, demands a more sophisticated test setup than a load cell crushing the rim directly. Further, as the rim deforms axially, it is desirable that no transverse forces act on the rim. The solution found is to place an impact box between the trolley and the rim.

A schematic illustration of the test setup is shown in Figure 4.1. The crushing force acting on the rim is denoted  $F(t)$  and is shown in the green box. The concept is designed for impacts where the trolley travels at a velocity of 5 m/s before hitting the impact box, initially at rest.

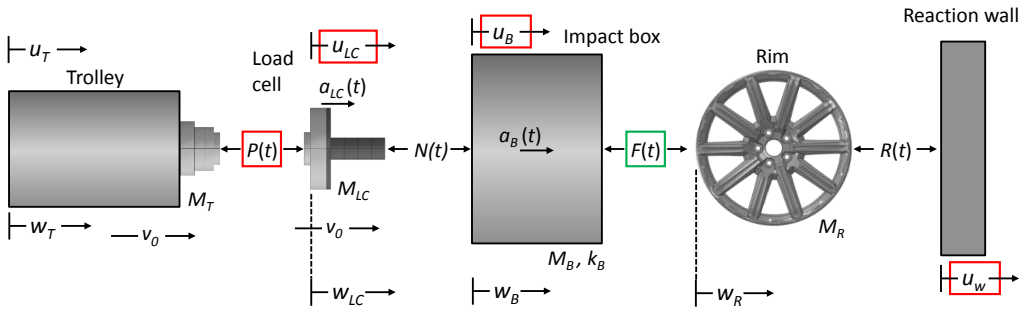


**Figure 4.1:** Free body diagram of the test setup.

The symbols denote the following:

- $P(t)$  - Internal force in the load cell where strain gauges are glued on
- $N(t)$  - Contact force between the nose and the impact box
- $F(t)$  - Contact force between the impact box and the rim
- $R(t)$  - Contact force between the rim and the reaction wall
- $v_0$  - Initial velocity of the trolley and load cell
- $u_T$  - Rigid body translation of the trolley
- $u_{LC}$  - Rigid body translation of the load cell
- $u_B$  - Rigid body translation of the impact box
- $u_w$  - Rigid body translation of the reaction wall
- $a_{LC}$  - Acceleration of the load cell
- $a_B$  - Acceleration of the impact box
- $w_T$  - Deformation of the trolley
- $w_{LC}$  - Deformation of the load cell
- $w_B$  - Deformation of the impact box
- $w_R$  - Deformation of the rim
- $M_T$  - Mass of the trolley
- $M_{LC}$  - Mass of the load cell
- $M_B$  - Mass of the impact box
- $M_R$  - Mass of the rim
- $k_B$  - Stiffness of the impact box

In Figure 4.1 the crushing force of interest,  $F(t)$ , is placed in a green box. From an experimental point of view, the measurable metrics are placed in red boxes.  $P(t)$  can be logged by a load cell. The available load cell has a maximum acquisition frequency of 250 kHz. Accelerations are not logged directly but computed from the second derivative of the translations. Both the load cell and the impact box are intended to move in one direction only with no rotation. 2D-DIC with point tracking is therefore sufficient. The high-frequency cameras available at NTNU

have an acquisition frequency of 30 kHz when the image size is appropriate to capture the expected translations. Assuming the total time of impact is no longer than 100 ms, the approximate maximum number of data points is 25 000 from the load cell and 3 000 pictures from each DIC camera. This is considered enough data points to sufficiently capture the force vs. displacement history of the rim.

## 4.2 Assumptions and Simplifications

To estimate  $F(t)$ , the following assumptions and simplifications are made:

1. *The reaction wall is rigid.* In numerical simulations, this is achieved by the use of an analytical rigid or meshing the wall using rigid elements. For the experimental setup, a sufficiently strong wall is required. The reaction wall in the kicking machine is considered to be rigid. The rigid wall is assumed not to deform. However, translations of the reaction wall may occur and can be accounted for by subtracting this translation from the translations of the impact box and the load cell.
2. *The trolley and load cell do not deform plastically.* This can easily be checked in numerical simulations and by visual inspection in the experimental setup.
3. *The impact box does not deform plastically.* If this is not fulfilled, some of the initial kinetic energy in the system will be dissipated through plastic deformation during impact. The design of an impact box capable to withstand the acting forces was an essential part of Martinsen's thesis. All numerical simulations and physical tests should be thoroughly checked to ensure that the design is in accordance with this assumption.
4. *The impact box is for practical purposes considered rigid.* The stiffness contribution of the impact box to the estimation of the crushing force can be neglected.
5. *Rotational and three-dimensional effects can be neglected.* To be able to measure the system with the available equipment, only a limited number of metrics can be measured. Experimentally, the impact box is constrained to move in the longitudinal direction only.
6. *Translation of the trolley equals the translation of the load cell.* In the numerical model, the two parts should be tied together. In the experimental setup, the load cell is mounted to the trolley by heavy machine bolts.

7. *Rim displacement is equal to impact box translation.* The displacement of the rim is assumed to be the same as the translation of the impact box until maximum displacement. Continuous contact between the box and the rim is assumed until rebound of the box.

### 4.3 Estimation of Rim Contact Force

To estimate the contact force,  $F(t)$ , mechanical equilibrium is applied to the free body diagram in Figure 4.1. D'Alembert's principle is utilized to take the inertia into account.

Equilibrium of the load cell:

$$P(t) = N(t) + M_{LC}a_{LC}(t) \quad (4.1)$$

Equilibrium of the impact box:

$$N(t) = F(t) + M_B a_B(t) + k_B w_B(t) \quad (4.2)$$

From Assumption 4, the deformation of the impact box is zero,  $w_B = 0$ . Using this, in addition to rearranging Equation (4.1) and (4.2), the following expression for the crushing force acting on the rim,  $F(t)$ , is obtained:

$$F(t) = P(t) - M_{LC}a_{LC}(t) - M_B a_B(t) \quad (4.3)$$

## 4.4 Translation from Integrated Force

### 4.4.1 Trolley Translation from Integrated Load Cell Force

The load cell and the trolley is assumed to follow the same translation. In experiments, the translation can be monitored by DIC. This translation can also be computed from the integrated force measured in the load cell. Applying mechanical equilibrium to the trolley the equation of motion, with initial conditions, reads:

$$M_T a_T(t) = -P(t) \quad \dot{u}_{T,0}(t) = v_0 \quad u_{T,0}(t) = 0 \quad (4.4)$$


---

Denoting the acceleration as the second derivative of the translation,  $a_T(t) = \ddot{u}_T(t)$ , and integrating twice forward in time yields the following expression:

$$u_T(t) = v_0 t - \frac{1}{M_T} \int_0^t \int_0^t P(\tau) d\tau d\tau \quad (4.5)$$

#### 4.4.2 Impact Box Translation from Integrated Forces

A similar derivation as described in Section 4.4.1 can be done for the impact box. Note the difference in initial conditions. The impact box is initially at rest. Thus, the following expression is obtained:

$$u_B(t) = \frac{1}{M_B} \int_0^t \int_0^t P(\tau) - M_{LC} a_{LC}(\tau) - F(\tau) d\tau d\tau \quad (4.6)$$

### 4.5 Calculation of Forces

In the proposed test setup, noise is expected to be present for the measured quantities both in the numerical analyses and in the physical experiments. All time domain quantities must therefore be filtered properly. Displacements must be filtered before being differentiated to ensure meaningful time series data for the accelerations. The measured force in the load cell should be filtered using the same filter to ensure consistency. All filters used in this thesis with complete filter definitions are listed in Appendix B. Finally, a moving average should be applied to the estimated impact force,  $F(t)$ , to provide a smoother estimation of the force.

#### 4.5.1 Signal Processing Flow

- **Numerically:** The proposed signal processing algorithm describing numerical estimation of the rim crushing force is found in Algorithm 1. A schematic representation of this algorithm is presented in Figure 4.2.
- **Experimentally:** The proposed signal processing algorithm describing experimental estimation of the rim crushing force is found in Algorithm 2. A schematic representation of this algorithm is presented in Figure 4.3.

### 4.5.2 Numerical vs. Experimental Estimation

The main difference between numerical and experimental estimation is the data available. In a simulation, significantly more output data is available compared to what is practically measurable in physical tests. The crushing force acting on the rim is an important example of this. In numerical simulations,  $F(t)$  can be defined as the contact force between the impact box and the rim. Thus, the *estimated* and *actual* crushing force can be compared. This is not possible in experiments where the force can only be *estimated*. To ensure the validity of the force estimation scheme presented; in Chapter 5, it is shown that the contact force can be estimated using the proposed method. To do so, numerical simulations are carried out where the estimated and actual crushing force are compared.

Achieving a symmetric impact is easy in a numerical model where parts can be placed exactly centric with respect to each other. For a physical setup, this is practically impossible. Assessment of the underlying assumptions should therefore be thoroughly investigated in experiments.

In numerical simulations, the reaction wall can easily be modeled using a rigid plate, constrained against rigid body motion. This is not equivalent to the experiments where the test rig itself might translate. Displacements of the impact box and the load cell must therefore be adjusted for this experimentally.

**Algorithm 1:** Numerical Estimation of Rim Crushing Force,  $F(t)$ 

1. Extract the displacement of the load cell,  $u_{LC}$ , and impact box,  $u_B$ , as functions of time. These displacements are representative element displacements. Extract the strain in representative elements in the load cell, multiply with the cross-sectional area,  $A$ , and Young's modulus,  $E$ , to compute  $P(t)$ .
2. Find the instance in time when the impact box starts moving. That is the index before the first clear non-zero element in the array containing  $u_B$ . Set  $t = 0$  at this instance.
3. Shift all displacements such that at  $t = 0$ , all displacements are zero.
4. Determine how many elements to keep in the arrays *before*  $t = 0$ . Typically keep 7-10 elements to achieve proper filtering.
5. Filter  $u_B$ ,  $u_{LC}$  and  $P(t)$  using the *same* filter, choose between
  - (a) a Savitzky–Golay filter
  - or*
  - (b) a Zero-Phase Digital filter
6. Differentiate  $u_{LC}$  and  $u_B$  twice to obtain  $a_{LC}$  and  $a_B$ .
7. Assign the mass of the load cell,  $M_{LC}$ , and the impact box,  $M_B$ .
8. Estimate the crushing force acting on the rim according to Equation (4.3). Use a moving average to reduce noise. Typically a wide banded average should be applied.
9. Smooth the final signal using a moving average. Use a narrow banded average to only smooth the curve.
10. Set the force equal to zero at time equal to zero. Adjust the beginning of the force array such that boundary effects from the filter are minimized.

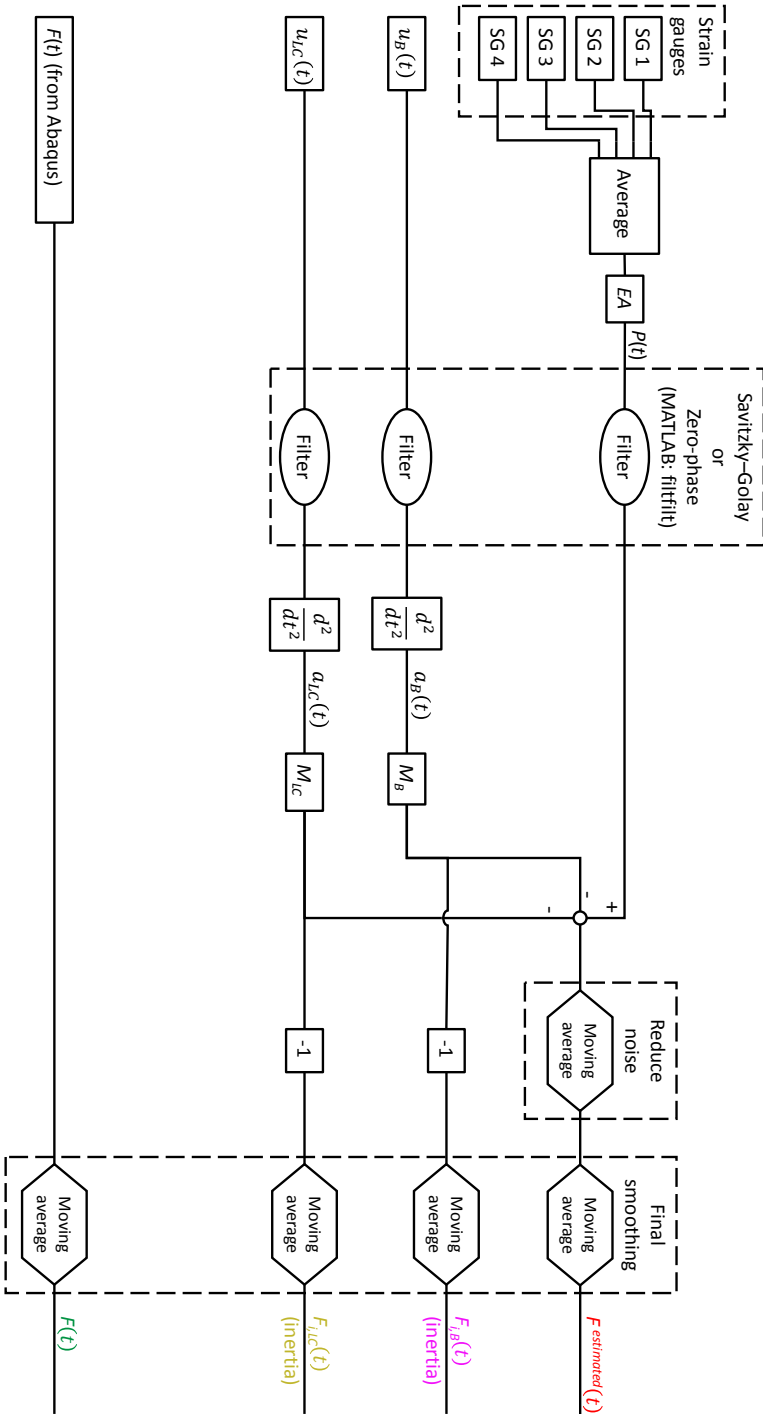


Figure 4.2: Flow chart of signal processing from numerical analyses.

**Algorithm 2:** Experimental Estimation of Rim Crushing Force,  $F(t)$ 

1. From DIC, extract displacement from all markers on the impact box,  $u_B^i$ , load cell,  $u_{LC}$ , and reaction wall,  $u_W$ . Treat each marker separately until later averaging. Extract the force recorded in the load cell at the instances of time when images used for DIC are taken.
2. Find the instance in time when the impact box starts moving. That is the index before the first clear non-zero element in the array containing  $u_B$ . Set  $t = 0$  at this instance.
3. Shift all displacement such that the instance the impact box starts moving all displacements are zero.
4. Determine how many elements to keep in the arrays *before*  $t = 0$ . Typically keep 7-10 elements to achieve proper filtering.
5. Shift the force recorded by the load cell,  $P(t)$ , such that before the first impact (and after the crushing has finished) the force is zero. Adjust for zero point drift if necessary.
6. Filter  $u_B^i$ ,  $u_{LC}$ ,  $u_W$  and  $P(t)$  using the *same* filter, choose between
  - (a) a Savitzky–Golay filter

*or*

  - (b) a zero-phase digital filter
7. Adjust the displacements  $u_B^i$  and  $u_{LC}$  by subtracting  $u_W$ . This is necessary to get the relative displacement with respect to the wall.
8. Differentiate  $u_{LC}$  and  $u_B$  twice to obtain  $a_{LC}$  and  $a_B$ .
9. Average the displacements and obtain accelerations for all markers on the impact box.
10. Assign the mass of the load cell,  $M_{LC}$ , and the impact box,  $M_B$ .
11. Compute the crushing force on the rim according to Equation (4.3). Use a moving average to reduce noise. Typically a wide banded average should be applied.
12. Smooth the final signal using a moving average. Use a narrow banded average to only smooth the curve.
13. Set the force equal to zero at time equal to zero. Adjust the beginning of the force array such that boundary effects from the filter are minimized.

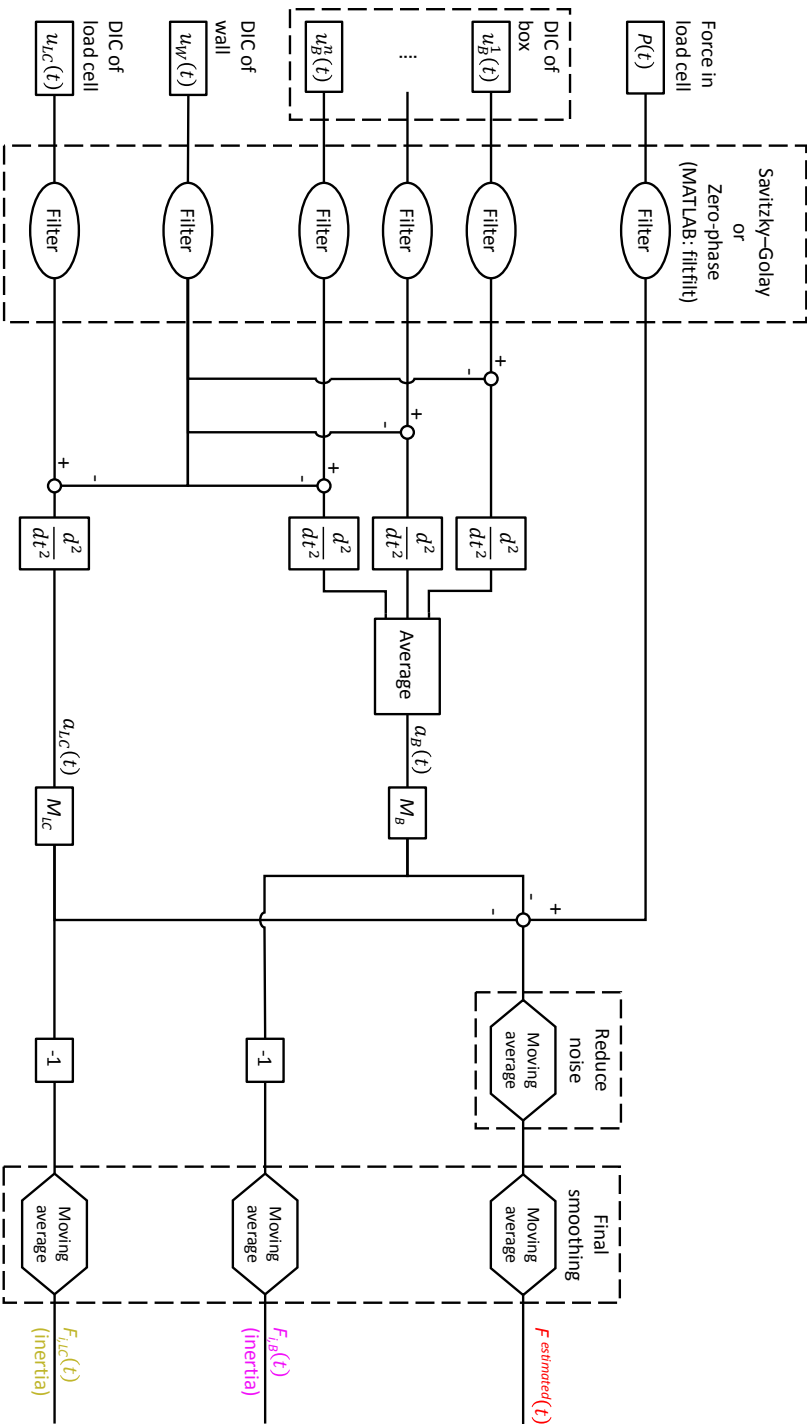


Figure 4.3: Flow chart of signal processing from experimental tests.

## Chapter 5

# Numerical Modeling

### 5.1 Base Model

A numerical base model has been established in Abaqus/CAE based on the designed test rig. Analyses are computed using Abaqus/Explicit. The base model is built around an orphan mesh of the rim provided by Audi. The original Abaqus model was developed by Martinsen and takes the material characterization found by Kittilsen and Swanberg for the rim. For this thesis, modifications have been made to the numerical model to make it more representative of the physical test rig for later validation. In this chapter, the base model is presented. All numerical simulations carried out for this thesis are based on this model. At first, the purpose of the base model is to numerically validate the force estimation scheme presented in Chapter 4. In Chapter 7, numerical analyses are compared to experimental tests to investigate the validity of the numerical model.

#### Parts

An assembly of the Abaqus model is shown in Figure 5.1, consisting of all the parts included in numerical simulations. The FE model takes only the relevant parts into account. In Figure 5.2, a CAD model of the impact section is shown with a more realistic assembly compared to the experimental setup. However, to make the FE simulations less computationally expensive, the support parts of the physical setup is not modeled in Abaqus but instead included through boundary conditions and constraints.

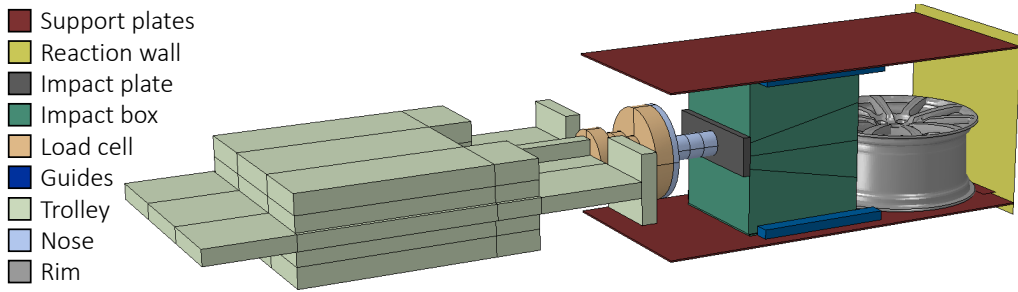


**Figure 5.1:** Assembly of Abaqus FE model.

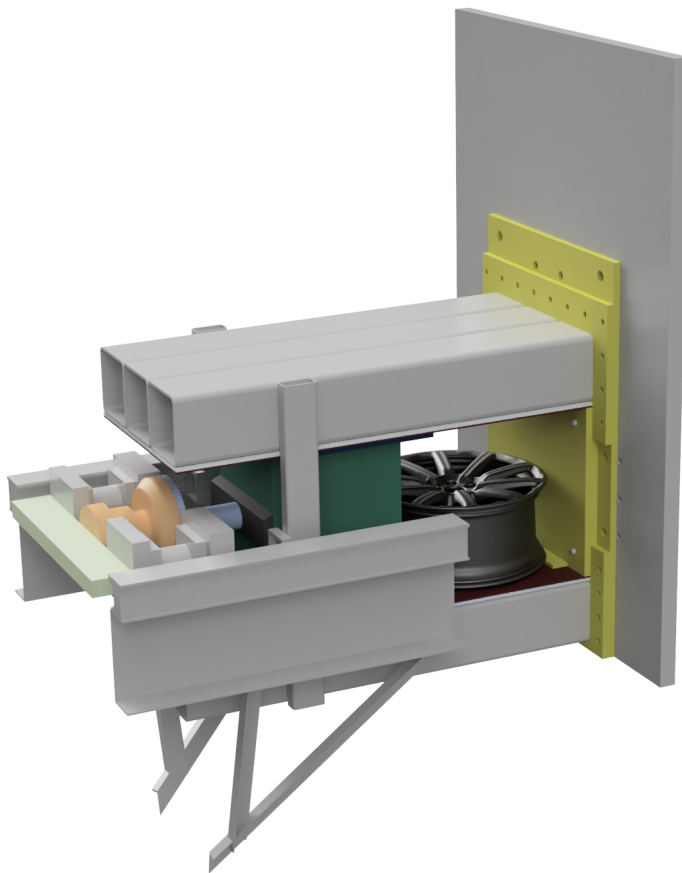


**Figure 5.2:** CAD model of the assembly with part of trolley and kicking machine rails.

## Mesh

The FE model is build up using solid and shell elements. The following parts are meshed with conventional reduced integrated eight-node solid elements (C3D8R): trolley (approximate element size of 15 mm), load cell (5 mm), nose (5 mm), impact plate (5 mm), guides (10 mm), top and bottom plate of impact box (10 mm) and support plates (10 mm). The following parts are meshed with conventional reduced integrated four-node shell elements (S4R): the impact box (10 mm) and the side plates of the impact box (5 mm). The reaction wall is meshed with four-node discrete rigid elements (R3D4) given an approximate element size of 60 mm. The reaction wall is meshed using multiple rigid elements instead of an analytical rigid to be able to monitor forces at different locations of the reaction wall. The rim was provided by Audi as an orphan mesh. The rim bed consists of shell elements and the spokes consist of solid elements, respectively S4R and C3D8R.

## Materials

Different parts of the numerical model have been given different material properties. All materials used with their elastic and viscoplastic properties are listed in Table 5.1. The Voce parameters for the aluminum rim are based on the work of Kittilsen and Swanberg. Rim bed and spoke sections are shown in Figure 3.4. Yield stress,  $\sigma_0$ , for the spokes is set to 200.0 MPa, not 181.3 as used in previous master theses corresponding with the result of the this year’s material tests, described in Section 3.3. Strain rate dependency is included for the spokes and the material parameter,  $C$ , is based on the SHTB tests, described in Section 3.3.3. Strain rate sensitivity for the rim bed is set to  $C = 0.0001$  a lower bound for cast aluminum. The other parameters are the same as used by Martinsen. The trolley

Material	$E$ (GPa)	$\nu$ (-)	$\sigma_0$ (MPa)	$Q_{R1}$ (MPa)	$\theta_{R1}$ (MPa)	$Q_{R2}$ (MPa)	$\theta_{R2}$ (MPa)	$C$ (-)	$\dot{p}_0$ (1/s)
Steel - S355	210	0.33	355	71.8	3 442.0	200.5	2 022.0	0.016	0.001
Steel - S420	210	0.33	420	178.5	4 610.0	630.9	508.4	0.016	0.001
Steel - S500	210	0.3	500	127.9	4 595.0	13 650	303.0	0.011	0.001
Steel - Bolt	210	0.3	874	127.9	4 595.0	13 650	303.0	0.011	0.001
Al - Rim bed	70	0.3	208.2	86.2	1 534.4	30.8	7 379.7	0.001	0.0005
Al - Spokes	70	0.3	200.0	84.2	1 321.9	47.3	8 381.6	0.00718	0.0005
PA6	3.2	0.39	- not used -						

**Table 5.1:** Materials used in the Abaqus base model and their properties.

is assigned S355, the impact box is assigned S420, the impact plate is assigned S500, the load cell and nose is assigned Bolt and the guides and the support plates are assigned PA6. PA6 is nylon polymer material intended to experimentally reduce friction when the impact box slides in the direction of impact. Densities are  $7900 \text{ kg/m}^3$  for S355, S420 and S500,  $7850 \text{ kg/m}^3$  for Bolt,  $2700 \text{ kg/m}^3$  for aluminum and  $1140 \text{ kg/m}^3$  for PA6.

### Boundary Conditions, Constraints, Initial Conditions and Contact

The numerical model is given boundary conditions, constraints, initial conditions and contact formulations to represent the physical system. The following applies:

- The reaction wall is encastered, consequently setting all translational and rotational degrees of freedom to zero throughout the simulation.
- The top surface of the upper support plate and the bottom surface of the lower support plate are encastered. This makes it unnecessary to model the top and bottom HUP beams.
- The edges of the trolley where it runs on rails are constrained to allow only translation in the direction of impact. Consequently setting all translational degrees of freedom in the vertical and transverse direction of the movement of the trolley to zero.
- The parts in the physical experiment that are bolted or welded together are in Abaqus tied together using constraint type *tie*.

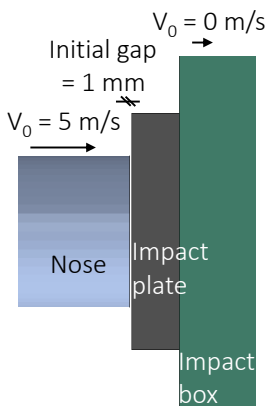


**Figure 5.3:** Initial gap.

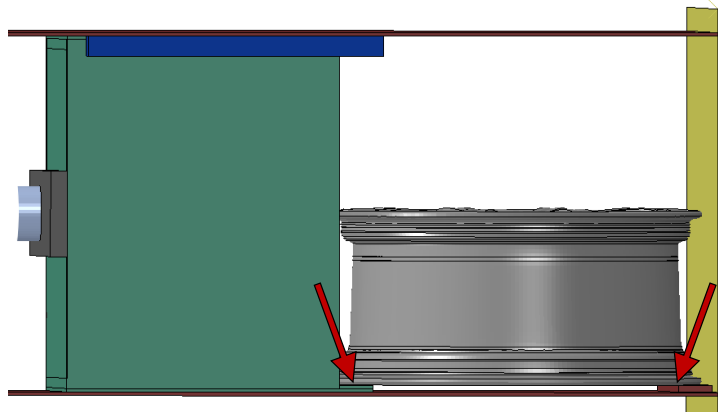


**Figure 5.4:** The rim is placed on supports.

- The trolley, load cell and nose are given an initial velocity of 5 m/s in the direction of impact.

At the beginning of the numerical simulation the nose is displaced by a distance of 1 mm from the impact plate, seen as the initial gap in Figure 5.3. As already stated, and seen from the figure, the nose hits the impact plate with a velocity  $v_0$ . In the base case this velocity is set to 5 m/s. This situation is meant to represent the instance in time right before the impact. The initial gap of 1 mm was chosen, making it unnecessary to model the acceleration phase of the trolley, which would be computationally demanding. At the same time, the gap ensures no numerical instabilities in the initial phase of the simulation. The rim is placed on supports similar to the experimental setup. This is shown in Figure 5.4. Contact is included through a *General Contact, All with self* and a penalty friction formulation with hard pressure-overclosure contact. Contact pairs for the spoke section are defined to take inner element surfaces into account when elements are eroded.

## Damage

Damage is taken into account in the numerical model through the Cockcroft-Latham criterion, defined in Equation (2.6). Damage is only considered for the rim since all other parts are intended to only undergo elastic deformation. Failure is modeled in Abaqus using element erosion. The numerical value for the failure parameter,  $W_c$ , is taken to be the value found by Kittilsen and Swanberg. This is  $W_c = 39$  MPa for the rim bed and  $W_c = 18.57$  MPa for the spokes.

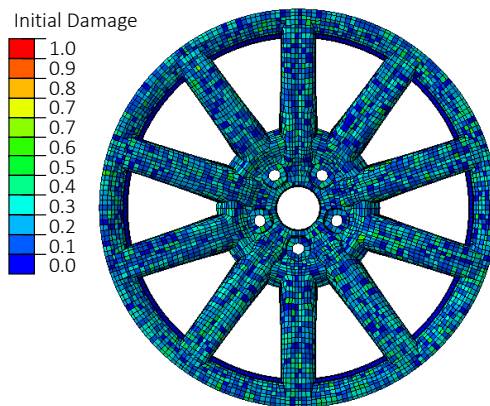


**Figure 5.5:** Initial damage distribution in spoke elements.

## Probabilistic Failure Modelling of the Rim

The probabilistic failure of the rim is taken into account by utilizing the method developed by Kittilsen and Swanberg. The same probability distribution as in previous master theses, with a mean value of  $\mu = 0$  and a standard deviation of  $\sigma = 0.25$ , were used. Running a pseudo-random MATLAB code the initial damage distribution for the spoke elements is obtained, seen in Figure 5.5. Keep in mind, if the MATLAB code were run again, another distribution would be obtained. As the results from the numerical simulation are dependent on the initial damage distribution, the stochastic behavior of the cast aluminum could be investigated numerically.

## Running Simulations

The numerical model is computational demanding because it consists of many small elements. Thus, a low critical time step is needed, as well as demanding integration and assembling of the stiffness matrix at each time step. Running on a cluster using 12 CPUs, 0.1 seconds of simulation takes approximately 7.5 hours.

The model requires two user-defined subroutines. `vuhard` is used to implement the modified Johnson–Cook model. `vusdfld` is used for the damage criterion.

The model is established in Abaqus/CAE 2017 and used to write the input file (`.inp`) needed to run simulations. However, due to the implementations of subroutines, both Abaqus/Explicit 2017 and Abaqus/Explicit 6.14 have been used to carry of simulations. The subroutines and version used depend on the desired output of the simulation.

## 5.2 Numerical Validation of the Force Estimation Scheme

### 5.2.1 Force Comparison

The objective of the numerical validation of the force estimation scheme is to investigate the robustness of the concept presented in Chapter 4, and check that what is conceptually presented in Figure 4.1 can be utilized for this three-dimensional problem. That means estimating the crushing force acting on the rim,  $F(t)$ , from the load cell registered force,  $P(t)$ , and the impact box and load cell accelera-

tions, respectively  $a_B$  and  $a_{LC}$ . In numerical simulations this is possible as  $F(t)$  is defined as a contact force output.

For this numerical validation the Abaqus base model presented in Section 5.1 is used. All history outputs from the FE analysis are logged at 30 kHz, implying 3000 data points for the 0.1 second long simulation. This is the same frequency used to log the experimental tests. Post-processing is done in MATLAB. Following the flow chart in Figure 4.2, the filter used for strains and displacements is a minimum-order lowpass finite impulse response zero-phase filter with normalized passband frequency  $0.011\pi$  rad/s, stopband frequency  $0.1\pi$  rad/s, passband ripple 1.0 dB, stopband attenuation 130 dB and using equiripple design method. The response, gain (magnitude) and phase, and impulse response of this filter is seen for filter 5 in Appendix B. The moving average used to reduce noise is a convolution of the signal and a vector of length 35 with equal values of  $1/35$ . The final smoothing is also a convolution similar to the first but with a vector length of 15 with equal values of  $1/15$ . The reader should be informed that the zero-phase filter and the moving averages used were obtained by extensive trial and failure.

In Figure 5.6 the rim crushing force from the numerical simulation is seen. Figure 5.6a shows the crushing force for a given displacement. Figure 5.6b shows the mean crushing force up to a given displacement. Both are plotted up to maximum displacement. The green curve is the crushing force taken as a direct contact output. The red curve is the estimated crushing force using the force estimation scheme. Clearly seen, the estimated force is similar to the actual force. The estimated force captures the peaks and overall trend of the actual force.

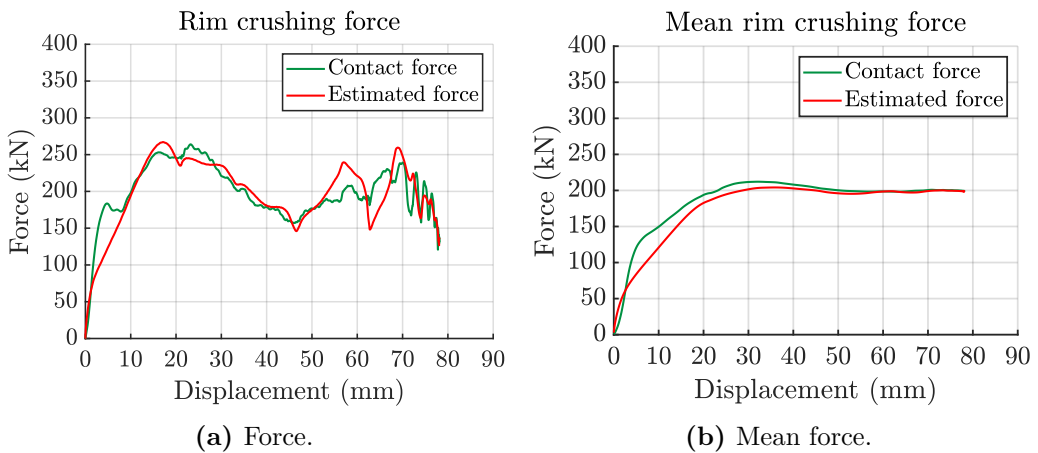


**Figure 5.6:** Comparison of actual and estimated contact force.

The main difference between the estimated and actual force is initial stiffness, which is the slope of the curves before 10 mm displacement. Due to filter boundary effects some stiffness is filtered out. However, when using the same filter, analyses can be compared to experimental tests.

Based on Figure 5.6 it is evidential that the force estimation scheme presented in Chapter 4 is a possible approach to estimate the crushing force. Although the actual force and the estimated force are not completely corresponding, the estimate is considered to capture the peaks and trends of the force to a significant extent. Based on the numerical results one can conclude that the scheme is valid and can be used in physical experiments where the crushing force can only be estimated.

To further study the three contributions that sums to the estimate of the crushing force,  $F = P - M_{LC}a_{LC} - M_B a_B$ , they are plotted separately in Figure 5.7. Filtered values are plotted.  $P$ , being the force in the load cell, is the blue line. The inertial forces of the impact box and the load cell are plotted as the purple and yellow line respectively. All in correspondence with Figure 4.2. From Figure 5.7 it is clear that  $P$  and  $M_B a_B$  contribute significantly more than  $M_{LC} a_{LC}$ . Neglecting inertia of the load cell would not significantly change the estimated crushing force. However, for consistency and accuracy of the estimation, and the fact that it is easy to include, the load cell inertia is taken into account. The peaks throughout the analysis is a consequence of the kinematics of the system. The nose of the trolley hits the impact plate multiple times during the crushing. These repeated impacts are explained by the significant difference in mass between the trolley

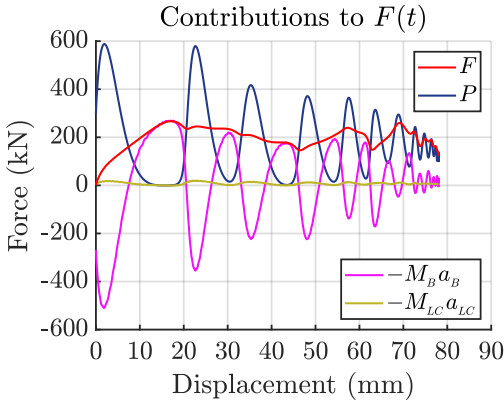


**Figure 5.7:** Contributions to estimated crushing force, showing filtered values.

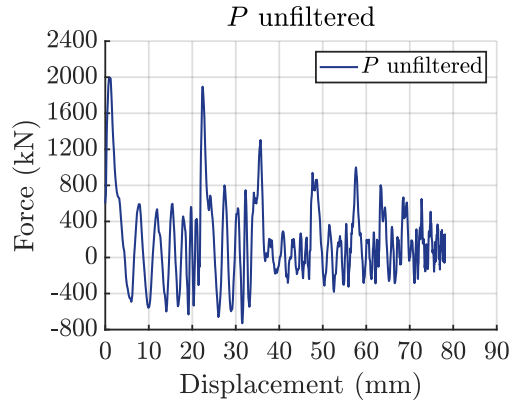


**Figure 5.8:** Unfiltered load cell force.

and the impact box. When the trolley impacts the box it shoots off with a higher velocity than the trolley. Consequently, a gap between the nose and the box is established. After this, as the rim deforms, the box slows down before once again being hit by the trolley.

Although Figure 5.7 overall looks satisfying, the reader should be informed that the magnitude of the peaks in load cell force and inertia forces are *not* correct. They are all filtered and consequently peak values are smoothed. However, the estimated crushing force,  $F$ , becomes correct as the peaks of the  $P$  and  $M_B a_B$  are smoothed equally but on opposite sides of the x-axis, such that the sum of forces is preserved. The error is canceled out. The unfiltered load cell force is shown in Figure 5.8. Between the impacts, the main peaks, significant oscillations are seen. Filtering is therefore essential to achieve a meaningful estimation. Note that the maximum value recorded in the load cell is almost ten times greater than the maximum rim crushing force, 2000 kN compared to 200 kN. Thus, the impact force between the nose and the impact box is severely higher than the impact force between the impact box and the rim.

### 5.2.2 Different Filters

As part of the numerical validation of the force estimation scheme, different filters have been tested. In Figure 5.9, force and mean force curves using two additional filters are compared to the one already presented. The additional filters are two Savitzky-Golay filters, defined as filter 1 and filter 4 in Appendix B.

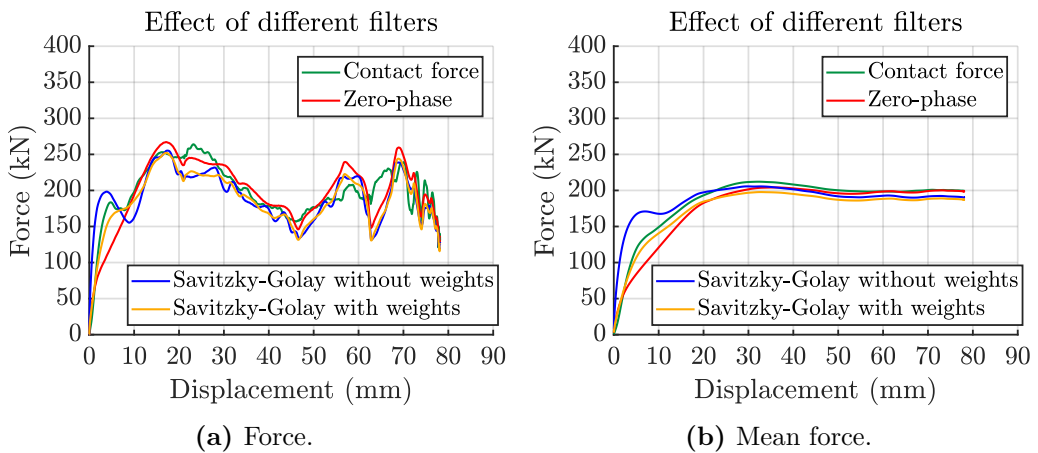


**Figure 5.9:** Comparison of different filters.

The first, the blue curve, is a simple filter without weights. It uses a polynomial order of 3 and a frame length of 95. The second, the orange curve, uses weights. It uses a polynomial order of 3 and a frame length of 87. The weights come from a normal distribution with  $\mu = 0.5$  and  $\sigma = 0.34$ .

Clearly seen from Figure 5.9, the initial part of the estimated crushing force depends significantly on the chosen filter. However, this dependency is limited only to the early phase of the force vs. displacement curve. This strengthens the conclusion that the force estimation concept can be used to estimate the impact force as long as the initial phase is disregarded. At maximum displacement the mean force is captured most accurately using the zero-phase filter. For this reason, when experimental tests are later compared to the numerical model, this filter will be used.

The force vs. displacement and mean force vs. displacement curves for all filters defined for this thesis are shown in Appendix C.

## 5.3 Energies

The energies of interest are taken as outputs from the simulations and are plotted in Figure 5.10. They are plotted as functions of time. The total energy is conserved, which is as expected from a dynamic analysis. As the rim deforms the total kinetic energy drops, and reaches zero at the time when the rim experience maximum deformation. This is seen in Figure 5.10 when the green line touches the time-axis at about 35 ms. The slight increase in kinetic energy after this point is due to the rebound of the impact box and trolley after impact.

The disturbing observation from Figure 5.10 is the significant amount of artificial strain energy compared to internal energy. In Figure 5.11 the percentage of artificial strain energy of internal energy is plotted throughout the simulation. The initial peak is not of interest since both internal and artificial energies are very low. However, as the rim reaches its maximum deformation the percentage goes towards 10%. This is significantly more than the best practice of less than 1% for explicit FEA.

To further investigate the contributing sets of the Abaqus model to artificial strain energy, three rim sets were defined. The contribution from these sets can be seen in Figure 5.12 and the geometrical sets can be seen in Figure 5.13. It is clear that the spokes contribute significantly more than the other sets and the rest of the model. These elements are reduced integrated solid elements.

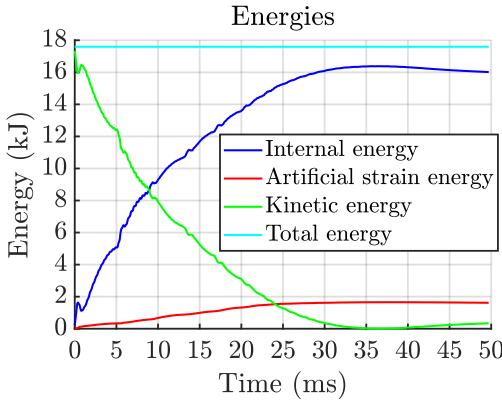


**Figure 5.10:** Comparison of energies throughout the simulation.

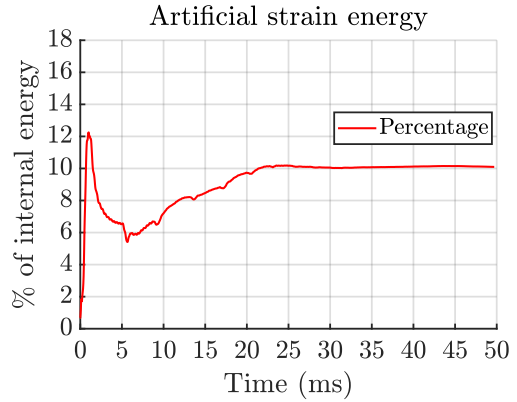


**Figure 5.11:** Percentage artificial compared to internal energy.

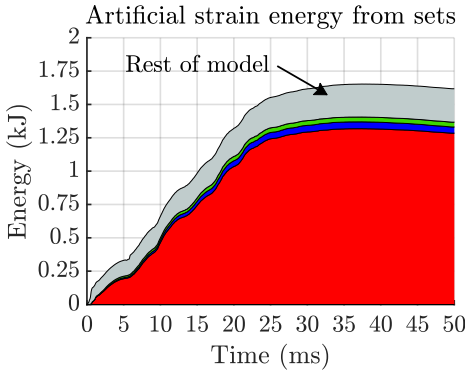


**Figure 5.12:** Contribution of different sets.

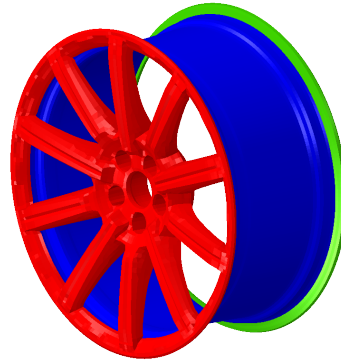


**Figure 5.13:** Rim sets.

In an attempt to reduce the amount of artificial strain energy, reducing hourglass stiffness has been tried. This has not been successful. Applying an hourglass scaling factor of 0.2 for the elements in the spokes yields only minor changes in terms of the energies. As the rim deforms the percentage of artificial strain energy is found to be about 10%, the same as for the original simulation.

While a significant amount of artificial strain energy is usually an alarming result, there are reasons to believe that for validation of the force estimation scheme it is acceptable. The Cockcroft-Latham failure criterion and element erosion is a part of the model. Most elements eroded throughout the simulation are part of the red spoke set in Figure 5.13. As fracture occurs and elements erode, artificial strain

energy is introduced. A simulation not including the failure criterion, and thus not eroding any elements, resulted in the percentage of artificial strain energy to be just below 6%. This shows that out the 10% in the base model a substantial amount comes from element erosion, although the deformation mode change when fracture is no longer included and the two simulations are not directly comparable. However, as long as fracture is a part of the model it is inevitable to produce this artificial strain energy. Although it would be desirable to reduce the amount of artificial strain energy it might not be a problem for the validation of the force estimation scheme. The crushing force acting on the rim can still be estimated and compared to the actual force.

The more alarming concern from this energy discovery is the applicability of the base model when validating the numerical model with experimental tests. More than 10% numerical energy dissipation, which is not physical, is a concern when comparing the experimental tests for validation of the numerical model. Later discussions in this thesis address this issue.

## Chapter 6

# Experimental Work

### 6.1 The Kicking Machine



**Figure 6.1:** The kicking machine.

The kicking machine available at the Department of Structural Engineering at NTNU is a device made for dynamic impact testing of structural components. The kicking arm is connected to the piston rod of a hydraulic/pneumatic actuator which is connected to a hydraulic piston accumulator. The hydraulic/pneumatic actuator system provides the moving force which rotates the arm and in effect accelerates the trolley which transverses the length of the rails until hitting a test specimen [31]. The maximum working pressure of the accumulator is 200 bar resulting in a maximum energy output of 720 kJ. The trolley will lose contact with the arm after about 2/3 of the stroke which leads to a maximum energy delivered to the trolley of approximately 500 kJ. Thus, with a trolley mass of 1500 kg, a maximum speed of about 26 m/s can be obtained.

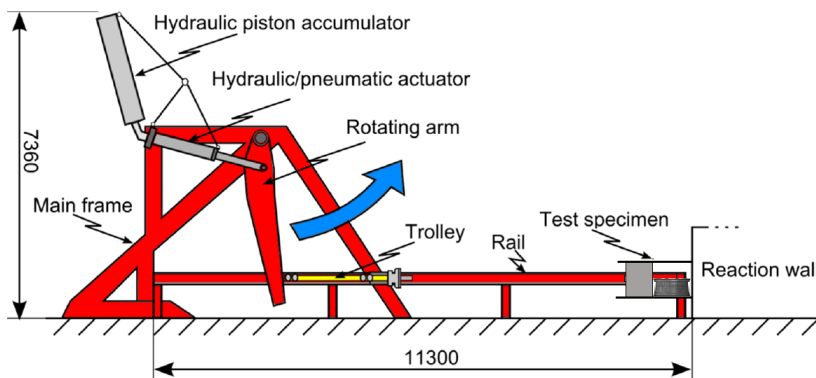


**Figure 6.2:** Illustration of the kicking machine at NTNU.

## 6.2 Design of a Test Rig for Rims

The culmination of Martinsen's master thesis was in large the design of a suitable crash rig module for crash testing of cast aluminum rims in the kicking machine. Martinsen was subsequently employed as a "vitenskapelig assistent" (scientific assistant) to further work on the test rig. During his six months of employment, some design alterations were done. In this section, a summary of the final rig design will be presented. For more in-depth information on the design process and calculations on the final geometry of the rig, one should see Chapter 4 of Martinsen's thesis.

The kicking machine accelerates a trolley along rails until it impacts a test specimen at the reaction wall. For most experiments, the test specimen, for instance a crash box, is fixed to the reaction wall. Due to the nature of the rim test and rim geometry, the rim must be placed in a rig to securely mount it to the kicking machine.

As the rim is fundamentally unsymmetrical, due to the spoke section, an impact from the rim bed side of the rim will create a moment about the lateral horizontal axis of the impactor. This moment makes it challenging to measure the crushing force acting on the rim and may also damage the equipment, derail the trolley or break the load cell. The main design idea was therefore to design a two-part system where the moment will be transferred to a box between the rim and impactor such that the trolley will only experience longitudinal forces. In addition, the rig was designed to minimize the vertical forces acting on the top and bottom plate. The final design of the crash rig is seen in Figure 6.3.

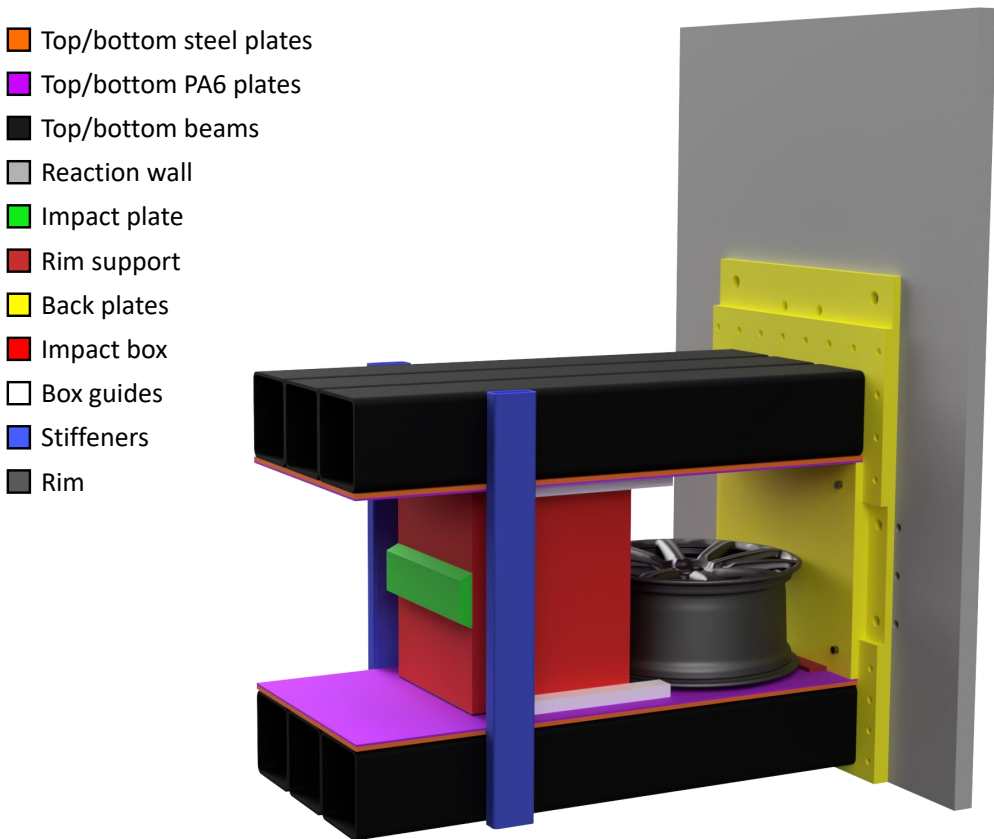


**Figure 6.3:** Crash rig assembly.

Grimsmo et al. [33] conducted high-energy impact tests in the kicking machine. In his experiments a trolley with mass 727 kg and velocity up to 12 m/s was used giving a kinetic energy of 52.3 kJ. Martinsen concluded that using a similar nose and load cell would work, but changing the mass of the trolley to 1500 kg and decrease the speed to 5m/s essentially applying initial kinetic energy of 18.8 kJ to the system. This was estimated to be enough energy to activate the deformation of both spokes and rim bed. A lower velocity was chosen to increase the total crushing time and by that making it easier to study the impact. Further, the velocity could be increased in future testing if more deformation is found to be desired. Assuming elastic behavior, the impact stress on the nose can be found through:

$$\sigma = \rho cV, \quad c = \sqrt{E/\rho} \quad (6.1)$$

where  $\rho = 7850 \text{ kg/m}^3$  and  $E = 210 \text{ GPa}$ . This gives a stress and corresponding impact force of 203 GPa and 1020 kN respectively. The designed nose is made of a high strength steel capable of withstanding this load and is extended to a length of 200 mm to allow for larger deformation of the rim.

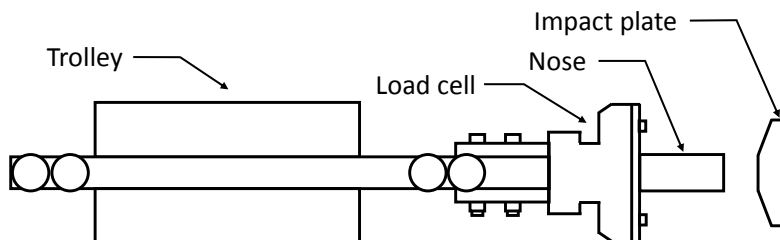


**Figure 6.4:** Trolley setup used. Similar to high-energy impact tests by Grimsmo et al. [33].

An essential part of the crash rig design is the impact box which transfers the load from the trolley to the rim. The design was optimized such that plasticity is avoided in the box for the given trolley mass and speed as well as minimizing the vertical forces acting on the top and bottom plates. The box consists of high-strength steel plates with six outer plates and three inner plates with the rim impact surface in front, shown in Figure 6.5. Several design iterations with different inner sections were proposed and tested numerically before the final fan design was found. The idea behind the design was to distribute the impact forces across the length of the box. The impact plate will diffuse the stresses from the nose avoiding highly local stresses on the box. On the rim side of the box, a simple support for the rim was added. This was done to prevent parts of the rim from getting stuck between the box and bottom plate, as was the case in preliminary numerical analyses. The dimensions of the box can be found in Figure 6.5.

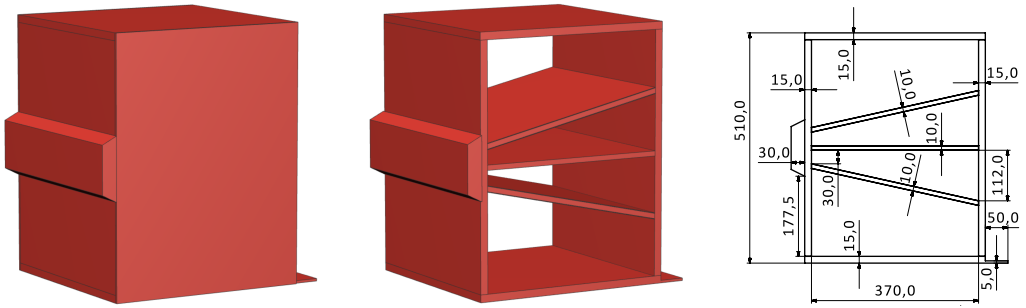


Figure 6.5: View and dimension of impact box with inner plates and impact plate.

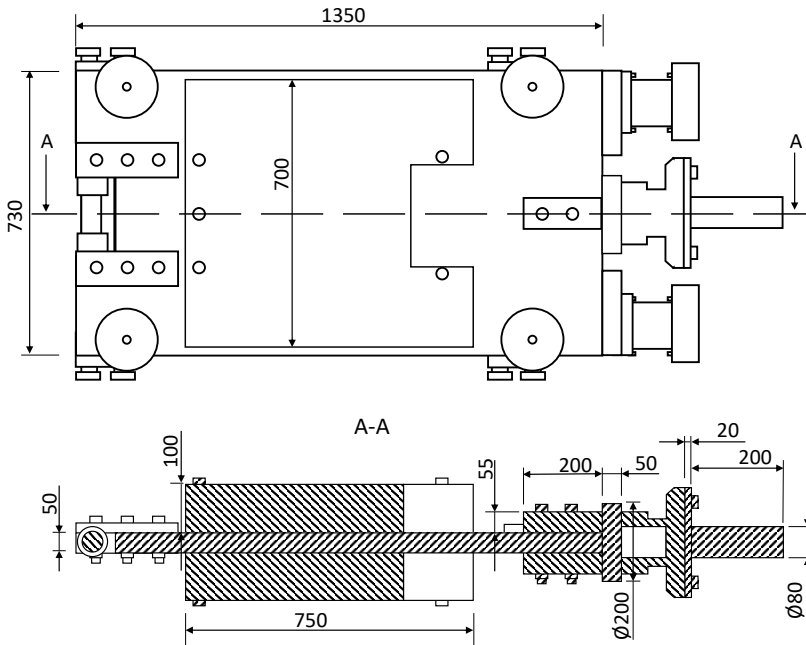
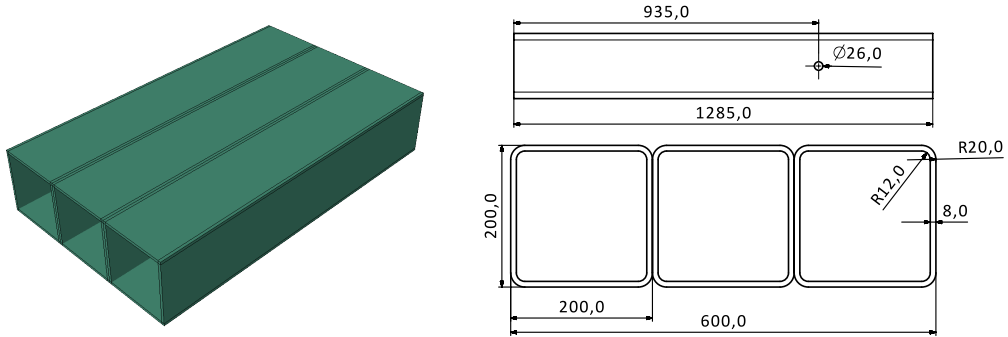


Figure 6.6: Trolley setup used in high-energy impacts.



**Figure 6.7:** Dimension of top and bottom plate.

In addition to the box, the crash rig consists of top and bottom beams made up of three HUP200 steel sections acting as supports for both the rim and box seen in Figure 6.7. The plates were designed to stay within a serviceability limit state stating that the maximum deflection of a beam or plate should not exceed  $1/250$  of the total span. A geometry was designed to give a sufficient moment of inertia based on Euler-Bernoulli beam theory. The beam sections are fitted with a steel plate which then is covered by a PA6 plate. The polymer is meant to reduce friction forces between the plates and the box.

To avoid out of plane deflection of the top and bottom plate, stiffeners are introduced as can be seen in Figure 6.3. Guides are also included to avoid lateral displacement of the box. The guides are made of PA6.

Depending on the mass and speed of the trolley, the rim may not have sufficient energy absorption meaning the trolley would not stop before the box and rim hits the reaction wall. To avoid potential damage to the rig, a secondary energy absorption system was discussed. Crash boxes mounted on the stiffeners or the rails of the kicking machine was proposed but not designed. Estimations indicated that the stiffeners were too weak to withstand the forces from a secondary energy absorption system. Thus, for all tests carried out for this thesis, such a system was not used.

To mount the rig to the reaction wall, the back plates were designed to fit with existing bolt patterns on the reaction wall. The top and bottom beams are mounted on the back plate.

### 6.2.1 Modifications on Final Rig

The rig was produced by Nomek from technical drawings provided by Martinsen. Some features of the rig were changed due to miscommunication or difficulties in production. The plates making up the fan structure in the impact box were manufactured to a thickness of 12 mm instead of the original 10 mm. This will only lead to a stiffer structure which is beneficial for the rim tests as the box is assumed to be rigid in the estimation of the rim crushing force. The expense is a slightly added weight which must be taken into account through inertial forces. The total mass of the impact box was weighed to 150 kg. In addition, the chamfer that was designed on the impact plate is not included in the final product.

The final assembly allows for a maximum deformation of 400 mm of the rim before the trolley makes contact with the stiffeners. With a trolley speed of 5 m/s, the deformation of the rim is far below this limit and the need for additional crash boxes was concluded unnecessary.

With available trolley modifications, a mass of 1 407.2 kg was achieved including the load cell and nose. The current trolley configuration is seen in Figure 6.6. To minimize the friction acting on the impact box, a 1 mm gap was added between the top PA6 plate and the box. In addition, the bottom PA6 plate is coated with a Teflon spray.

## 6.3 Test Setup

A test setup was proposed and later adopted to include four high-speed cameras, two optical sensors and a load cell. Two cameras with point tracking DIC were used to measure translations from which the accelerations were calculated of both the impact box and load cell. One camera was used with point tracking DIC with the purpose of measuring the translation of the top beam in order to get the true translation of the impact box and load cell relative to the reaction wall. This is needed as the massive reaction wall is resting on a rubber foundation which leads to movement of the wall. The last camera is used to film the deformation of the rim.

Two optical sensors were mounted on one of the rails of the kicking machine. These are triggered when the trolley passes through and the time between the two triggers is logged. With the known distance between the sensors, the initial velocity of the trolley can be accurately determined. The optical sensors also act as a start trigger for the high-speed cameras. For each picture captured by the

cameras, a trigger signal is sent to the load cell to sample the force measured at this instance in time. This is important as the force is needed at the same time instance as the corresponding accelerations. A schematic overview of the test setup is shown in Figure 6.8.

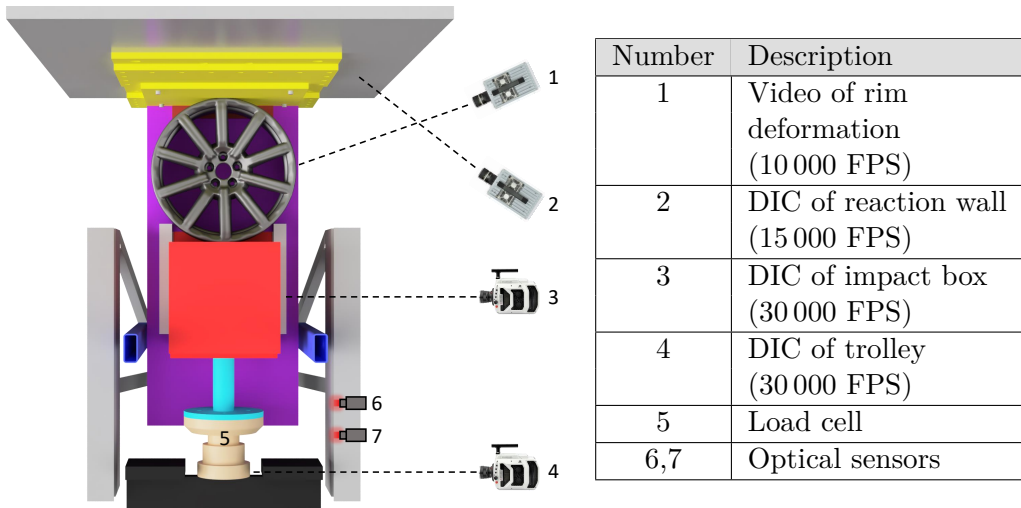


Figure 6.8: Overview of test setup.

Table 6.1: Sensor description.

### 6.3.1 Cameras

The cameras used in the experimental work, as well as their key features and potential resolution, are presented in Figure 6.9, 6.10 and 6.11. The bold numbers represent the configuration used during the tests.

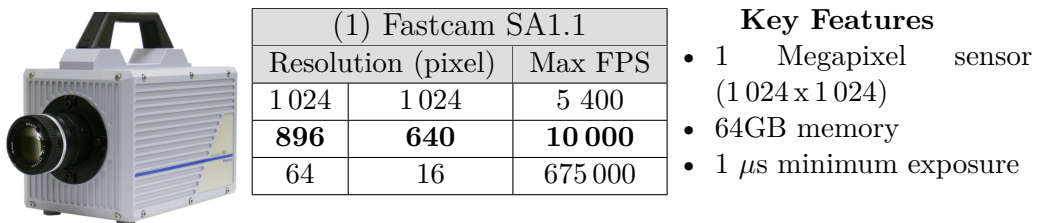


Figure 6.9: Key specifications for Fastcam SA1.1.



(2) Fastcam APX-RS		
Resolution (pixel)		Max FPS
1 024	1 024	3 000
<b>640</b>	<b>256</b>	<b>15 000</b>
128	16	250 000

**Key Features**

- 1 Megapixel sensor (1 024 x 1 024)
- 16GB memory
- 2  $\mu$ s minimum exposure

**Figure 6.10:** Key specifications for Fastcam APX-RS.



(3,4) Phantom v2511		
Resolution (pixel)		Max FPS
1 280	800	25 600
<b>1280</b>	<b>672</b>	<b>30 000</b>
128	32	1 000 000

**Key Features**

- 1 Megapixel sensor (1 280 x 800)
- 25Gpx/s throughput
- 1  $\mu$ s minimum exposure

**Figure 6.11:** Key specifications for Phantom v2511.

### 6.3.2 Load Cell

The load cell known as the "Large Load Cell 300 mm" has been used in all experiments in the kicking machine. Force is obtained by averaging the voltage signal from two strain gauges and multiplying with a calibration factor. The strain gauges are glued to the outside of the narrowest part of the load cell. They are placed circumferentially to each other. The load cell is capable of measuring constant loads of up to 500 kN and peak loads of more than 2 000 kN. The load cell chosen was the same used in impact tests by Grimsmo et.al [33] where similar force levels occurred. The load cell can record at frequencies of up to 250 kHz.

6.3.3 Images of Test Setup



Figure 6.12: Various images of the test setup.

## 6.4 Calibration of the Test Setup

### 6.4.1 Calibration of the Load Cell

The purpose of calibrating the load cell is to find the calibration factor to use when converting from recorded voltage to force. This is found to be problematic for the load cell used. Several calibrations have been carried out which suggest a broad range of calibration factors. When a calibration is done, the load cell is compressed in a machine with a known applied force. For several given compression forces, the voltage in the load cell is recorded. Thereafter, a least square fit is used to find the best line through the points. The slope of this line is the calibration factor. Consequently, the conversion from voltage to force is linear for all voltages. At low force levels, typically below 15 kN, it is expected to be some errors while for higher force levels the calibration is expected to be good.

Initially, a calibration of the load cell was carried out using the Instron 500 kN. Due to suspicious results, an additional four calibrations using the Instron 100 kN machine were carried out. For these four calibrations the curve was fitted to **a**) five values (0, 10, 20, 50 and 90 kN) and **b**) two values (0 and 90 kN). The load cell has also been used in the kicking machine in earlier experiments. The calibration factor used previously, as well as the ones found this year, are listed in Table 6.2.

Date	Machine	Setup	Calibration factor
June 2014	Unknown	Unknown	1 018.0
Nov. 2014	Dartec 500 kN	Unknown	1 095.9
10. April 2019	Instron 500 kN	Using a spherical bearing to absorb potential curvature	1 394.4
7. May 2019	Instron 100 kN	Using a spherical bearing to absorb potential curvature	a) 1 337.5 b) 1 358.8
7. May 2019	Instron 100 kN	No spherical bearing	a) 1 257.3 b) 1 250.9
7. May 2019	Instron 100 kN	No spherical bearing different logger	a) 1 257.4 b) 1 251.5
7. May 2019	Instron 100 kN	Using a thick steel plate to absorb potential curvature	a) 1 247.0 b) 1 263.9

**Table 6.2:** Calibration factors.

By inspecting the calibration factors listed in Table 6.2 it is clear that something is wrong with the calibration. Results should be more or less the same regardless of the machine used and setup. The June 2014 result may not be representative when comparing to the later results as the strain gauges might have been replaced between June 2014 and November 2014. However, the November 2014 result is comparable to the later results. Further, the calibration factor is only expected to change a couple of percentages over the years, not 27 % as in this case. No further assessment of the calibration of the load cell has been carried out. Instead, an alternative approach to transform from voltage signal to force is used, presented in Section 6.5.5.

### 6.4.2 Calibration of the Cameras and DIC Setup

2D-DIC has been used to track the rigid body motion of the impact box and load cell to measure displacement and calculate velocity and acceleration. For accurate results, the optical axis is ensured to be normal to the test specimen surface and direction of motion. The precise setup of the cameras is necessary to get physical results. Once the cameras were set up, a pixel to physical length ratio was calculated. This was done by measuring the physical distance between two markers and the virtual pixel distance in the DIC software. Depending on the desired output frame rate, the field of view of the cameras were cropped accordingly. The DIC setup is shown in Figure 6.13. From the left image, all the DIC markers are shown. On the nose, three markers are used. The trolley displacement is assumed to be the same as the nose displacement. Four markers are placed on the impact box and two markers are placed on the top support. The rigid body translation of the reaction wall is assumed to be the same as the displacement on the top support.



**Figure 6.13:** DIC overview and camera setup.

## 6.5 Ensuring Trustworthy Measurements from the Test Setup

To be able to present any results in a trustworthy manner, the metrics recorded in an experiment have been thoroughly checked. The purpose of this is to ensure that the measurements represent the actual responses. This section is based on a crash box test which is to be further discussed in Section 6.9. Crash boxes were chosen for validation for several reasons among their well know behavior. Easy and cheap testing were also determining factors.

### 6.5.1 Translation Measured by DIC

Several methods could be used to verify the translations from DIC. One sophisticated approach would be to compare DIC translations with laser recorded translations. This would require additional equipment in the test setup. For practical purposes, this has not been done.

A more straightforward approach was therefore used. 1) The maximum translation of the impact box was assumed to be the same as the maximum displacement of the crash box. 2) After the experiment, the length of the crash box was measured by hand. Subtracting this from its original length is considered to be the maximum displacement. Thus, elastic release after impact is neglected. For the crash box investigated the maximum displacement from DIC matches the measured deformation of the crash box. Based on this, the recorded DIC displacements are considered to be accurate and are used for further calculations.

### Impact Box

One of the fundamental assumptions in this study is that the impact box can be considered rigid. To assess this, the displacement of the four markers on the impact box has been measured. The markers are seen in Figure 6.14. Furthermore, the relative displacement of the first three markers to the fourth marker has been computed. The relative displacement of a given maker  $i$  as a function of time is given by  $u_i(t) - u_4(t)$  and is shown in Figure 6.15.

Considering the fact that the distance between Marker 1 and Marker 4 is 208 mm, a relative displacement of less than 0.5 mm is found to be small enough to support the assumption of a rigid impact box. Note that the forces acting on the impact

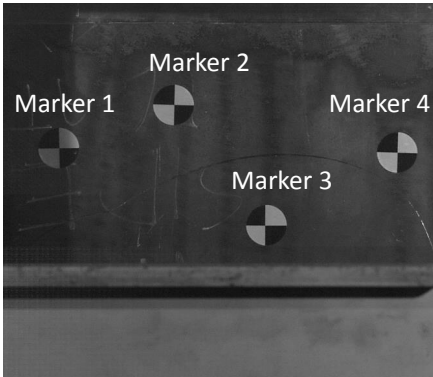


**Figure 6.14:** Markers at impact box.

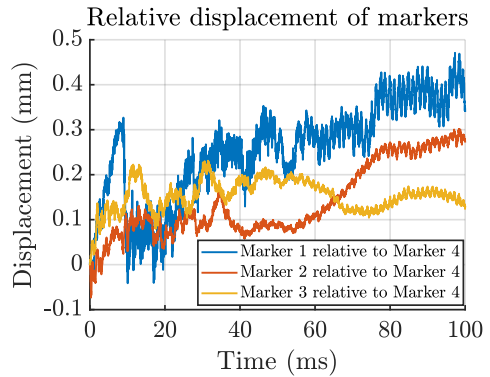


**Figure 6.15:** Relative displacements.

box when testing crash boxes are, in general, lower than for rims. This check of rigidity has therefore been carried out after all experiments.

## Reaction Wall

Previously presented, the reaction wall is mounted on a rubber foundation allowing horizontal translation of the entire setup. To assess whether or not this translation is significant, it was recorded using a high-speed camera. The recordings are shown in Figure 6.16. For practical reasons, the translation of markers located on the top support, seen above the rim in Figure 6.13, are tracked.

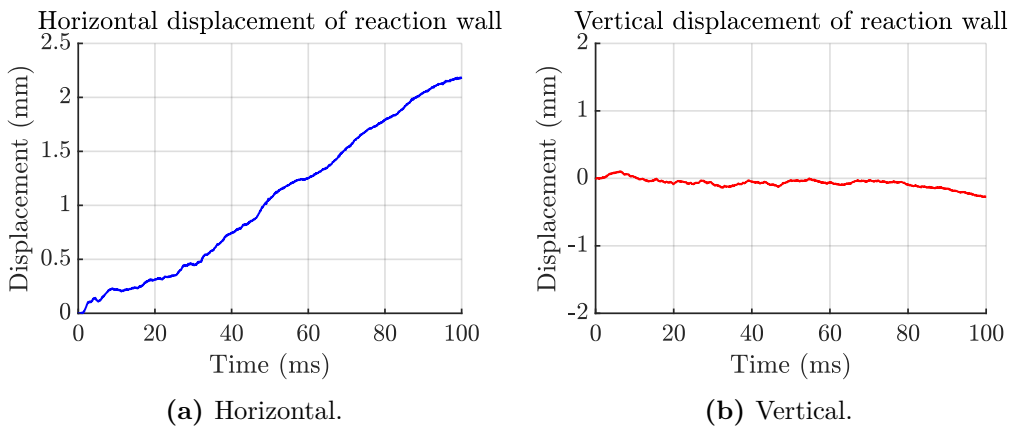


**Figure 6.16:** Displacements of the reaction wall.

The translation of the reaction wall is assumed to be the same as the top support. This is considered reasonable because the top support is very stiff in the axial direction. Seen from the Figure 6.16a the reaction wall translates horizontally more than 2 mm after 100 ms. The displacement of interest when rims are tested is the displacement of the rim relative to the reaction wall. In rim experiments, a displacement of magnitude 100 mm is expected. In this context, 2 mm is significant. Measured translations of the impact box and the trolley are therefore adjusted for horizontal rigid body translation of the rigid wall. This is done for all the experiments carried out in this study.

From Figure 6.16b the vertical translation of the reaction wall is plotted. For practical purposes, this is considered small. Thus, it is ensured that the top and bottom supports are sufficiently stiff.

### 6.5.2 Velocity Computed from Measured DIC Translation

Velocities of the trolley and the impact box are obtained by differentiating the filtered DIC translations once. To validate this method, the velocity of the trolley before impact computed from DIC has been compared to the velocity from the optical sensors. These sensors record the time it takes the trolley to move between two points at a distance of 250 mm. Thus, the mean velocity over this period of time can be calculated. Differentiating the translation prior to impact, the velocity of the trolley was 4.1546 m/s compared to 4.1540 m/s based on the optical sensors. These values are considered the same. The method of differentiating filtered translations is therefore found to be a valid method for computing velocities.

A weakness of this validation is that only trolley velocity *before* impact is compared to a second method of computing the same metric. During this period of time, the displacement curve is linear, and thus, a constant velocity. This is easier to capture with DIC compared to when the velocity changes rapidly. A method to validate the entire velocity history, for instance using a laser, would be preferable to ensure a trustworthy velocity history. However, for practical reasons, this has not been done.

### 6.5.3 Acceleration Computed from Measured DIC Translation

When estimating the rim crushing force, accelerations of the impact box and load cell are used. These are obtained by differentiating the filtered translations twice. Due to limitations in the test setup, computed accelerations cannot be validated.

However, because translations and velocities are concluded to be trustworthy, the accelerations are assumed trustworthy.

#### 6.5.4 Voltage Measured in Strain Gauges

The load cell logged at a frequency of 250 kHz in all experiments. However, the cameras following the trolley and the impact box only recorded at 30 kHz. The software in the kicking machine takes care of extracting data from the load cell at the instances in time when an image is taken. This is useful when post-processing the data from an experiment because accelerations and force in the load cell are needed at the very same instance in time. A possible bug in the kicking machine software was discovered which subtracted a constant value when writing the load cell output at the instance when an image is taken. To adjust for this, the load cell output was shifted so that the average value for the last 10 ms recorded was zero. In this period of time, the trolley is sliding back after the impact and the force should be zero. The logged voltage and the shifted values are shown in Figure 6.17.

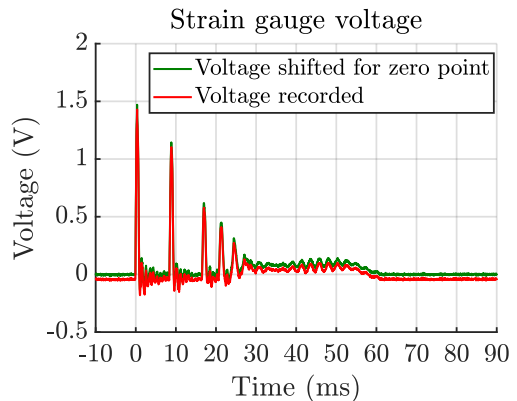


**Figure 6.17:** Mean voltage in strain gauges.

The pattern of the shifted curve in Figure 6.17 is reasonable. Before the initial impact, the force and thus the voltage in the strain gauges is zero. The peaks correspond to repeated impacts between the trolley and the impact box. The more constant value between 30 and 60 ms corresponds to the trolley and the impact box moving together and constantly crushing the test specimen. At 60 ms the crushing has reached its maximum. After this, the trolley starts moving in the opposite direction due to the elastic release of the system. No force is acting on the nose and thus no voltage is picked up.

#### 6.5.5 Integrated Force in Load Cell

Described in Section 6.4.1, the load cell force is obtained by multiplying the voltage with a calibration factor. It was further discovered in Section 6.4.1 that one of the calibration factors found this year is 27 % higher than the one found in 2014.

Consequently, the choice of calibration factor strongly affects the recorded force in the load cell. Thus, this significantly changes the estimated crushing force in the experimental tests. A correct calibration factor is essential in this study.

Because the calibration factor could not be determined with certainty, an alternative method to find the factor has been proposed. The idea is to extract the acceleration of the trolley based on the signal from the load cell. The acceleration is the load cell force divided by the mass behind the strain gauges. From acceleration and initial conditions the translation can be computed by integrating twice, following Equation (4.5). Comparing this to the translation found from DIC, the load cell signal can be linearly scaled to minimize the error between the two curves. This scaling corresponds to scaling the calibration factor. In Figure 6.18, the translation from DIC is plotted together with the translation from the integrated force using different calibration factors.

By inspection of Figure 6.18, it is clear that the calibration factor should be chosen with great care. The red curve is obtained by using a calibration that minimizes the error between the integrated load cell force and the translation from DIC (black curve). In other words, the calibration factor equal to 1108.0 does not come from a physical calibration but from an error minimization.

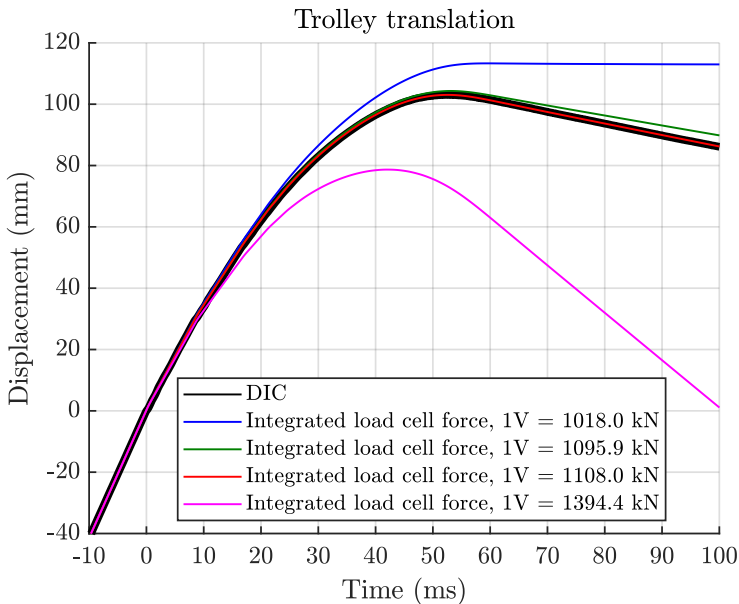


**Figure 6.18:** Comparison of translation of trolley measured by DIC and obtained by the integrated force using various calibration factors.

The deviation between the DIC and the integrated translation is for practical purposes negligible. From this, it was decided that instead of physically calibrating the load cell, it should be done as part of post-processing for all experiments. In all further presented experimental results where the signal from the load cell is involved, this method of calibration has been used.

## 6.6 Low-Velocity Gap Tests

To better understand the behavior of the test rig, seven low-velocity tests have been carried out. The purpose of the tests were to observe the free impact between the trolley and the impact box. The trolley was accelerated by pushing it by hand. Using up to four people resulted in a maximum initial impact velocity of 1.3 m/s. The impact box was initially at rest and allowed to move freely in the direction of impact. To capture the energy in the system, a single chamber crash box was placed with an approximate gap of 150 mm. This crash box obviously does not affect the free sliding of the impact box before long after the impact and is not relevant for the results presented in this section.

### 6.6.1 Theoretical Pure Elastic Impact

A reference to the tests is the theoretical pure elastic impact between two rigid bodies in one dimensional. Figure 6.19a and 6.19b show the trolley and the impact box, respectively before and after impact, with the notation used. Conservation of kinetic energy and conservation of linear momentum gives the equations for velocities after impact. They read:

$$v_{f,elastic}^{Box} = \frac{2}{1 + \frac{m_{Box}}{M_{Trolley}}} \cdot v_0^{Trolley} \quad (6.2)$$

$$v_{f,elastic}^{Trolley} = v_0^{Trolley} - \frac{m_{Box}}{M_{Trolley}} \cdot v_{f,elastic}^{Box} \quad (6.3)$$

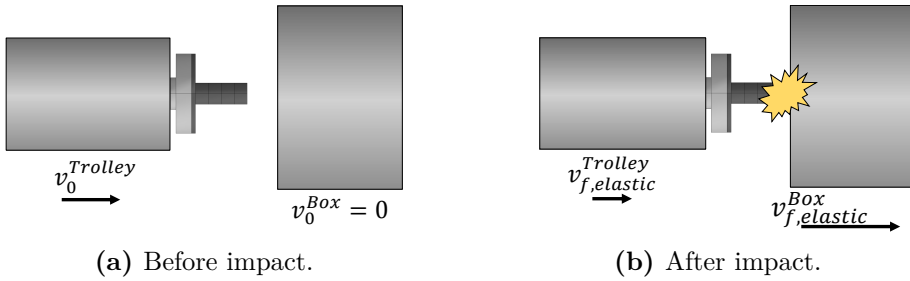


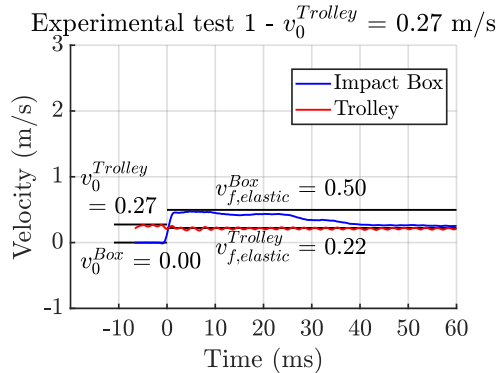
Figure 6.19: Illustration of pure elastic impact.

### 6.6.2 Test Results

In Figure 6.20, the velocities for both the trolley and the impact box are plotted for all seven tests. Time equal to zero is the time of impact. The velocities are obtained by differentiating the filtered translations from DIC. In addition, the theoretical pure elastic reference velocities are plotted according to Equation (6.2) and (6.3).

### 6.6.3 Rotation of Rig

By inspection of Figure 6.20, it is evident that the impact cannot be considered purely one dimensional. The qualitative pattern of the impact box velocity curve suggests there is some rotation. Looking at test 7 between 5 and 30 ms it seems like the impact box slows down before the velocity suddenly is increased. In this period of time, there is no contact between the trolley and the box. This increase in velocity is believed to be because of the angular rotation of the box. It was not intended in the original test design. After thoroughly measuring the test rig



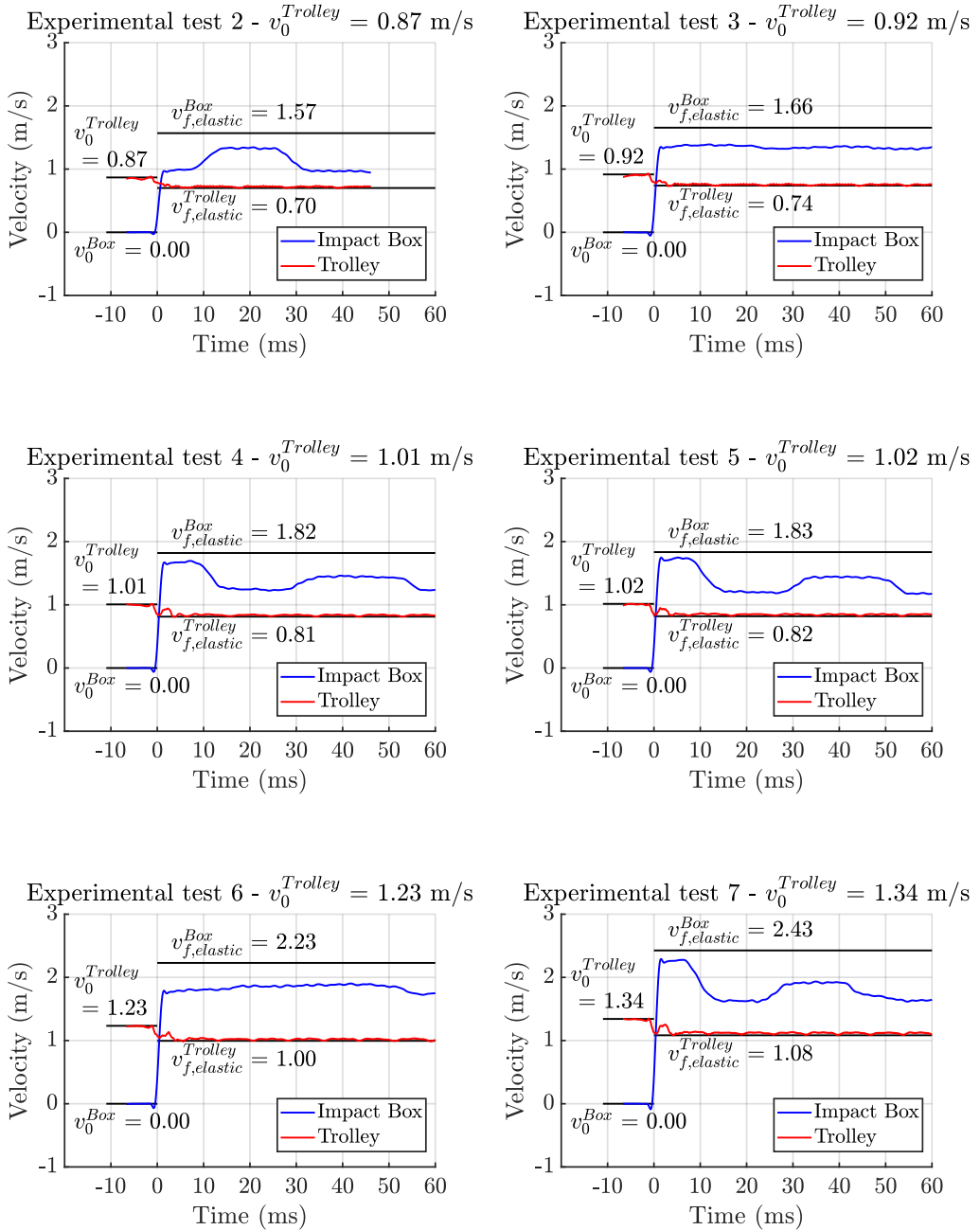
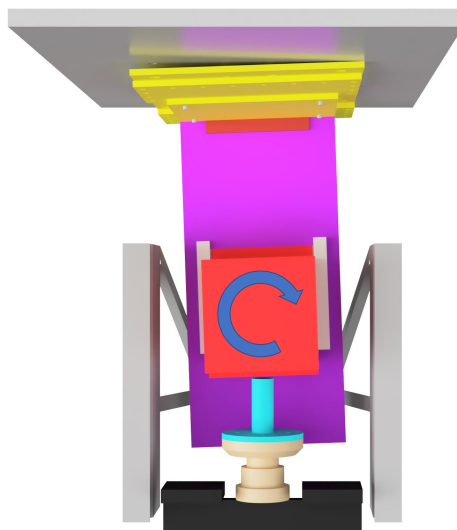


Figure 6.20: Low velocity impact tests with gap.



**Figure 6.21:** Off-centered impact.



**Figure 6.22:** Exaggerated rotated test rig.

installed, a small offset was found consequently leading to an off-centered impact. In Figure 6.21 the off-centered impact is shown and in Figure 6.22 the discovered offset in the rig assembly is shown.

In addition to the test rig being slightly rotated, there is a gap of 0.75 mm between the impact box and the supports on both sides. Therefore, because of the off-centered impact and the gaps, the impact box is allowed to rotate in one direction before hitting the supports, bouncing off and start rotating in the other direction.

To further investigate this imperfection in the experimental setup, a numerical model including the rotated test rig and the gaps was established. In the model, no rim or crash box was placed in front of the impact box; thus only simulating the impact between the trolley and the impact box. The initial trolley velocity was 0.275 m/s. In Figure 6.24 the velocities for the left and the right side of the box are plotted. The velocities are in the direction *parallel* with the initial direction of translation of the trolley. The velocities presented in Figure 6.24 are for the center element on each side. However, the velocity is the same for all elements on a given side.

From the numerical analysis, it is clear that the measured velocity on one side on the box, in reality, can be broken down to the sum of a rigid body translation and rotation. This is a problematic conclusion because the translation of the impact box is experimentally measured using 2D-DIC on only *one* side of the box.

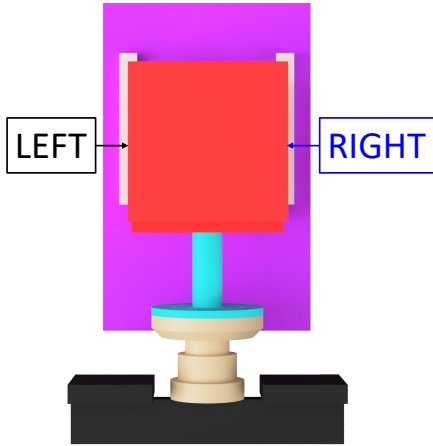


**Figure 6.23:** Marker location.

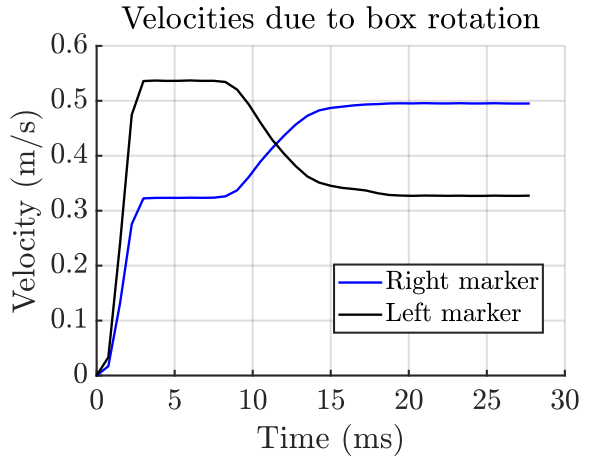


**Figure 6.24:** Velocities indicate box rotation.

However, when a test specimen is present, the impact box is more constrained against rotation. Lateral friction on the impact surface keeps the box from rotating. Further, when the initial trolley velocity is higher, the rotational effect will be less dominant. Thus, for rim tests, rotation of the impact box is considered not to disrupt the test results.

## 6.7 High-Velocity Crash Box Test With Gap

Another observation by inspection of the low-velocity test results, presented in Figure 6.20, is that the impact box velocity never reaches the theoretical pure elastic velocity after impact. To further investigate this, a test was carried out using a crash box placed with a gap of 30 mm to the impact box, shown in Figure 6.25. This gap is large enough for the free impact to take place, let the impact box slide freely before hitting the crash box. Consequently, allowing the initial impact to be investigated. The initial velocity of the trolley was 4.14 m/s. The recorded velocity-history for both the trolley and the impact box can be found in Figure 6.26. As always, velocities are obtained by differentiating the filtered translations found from DIC. Note that the sudden drop in velocity of the impact box right before time zero and the overshoot just after time zero are filter effects. These effects should be ignored when studying the figure.

One method to assess the experimental result is to compute the Coefficient of Restitution (CoR) and consider the deviation between the experimental result

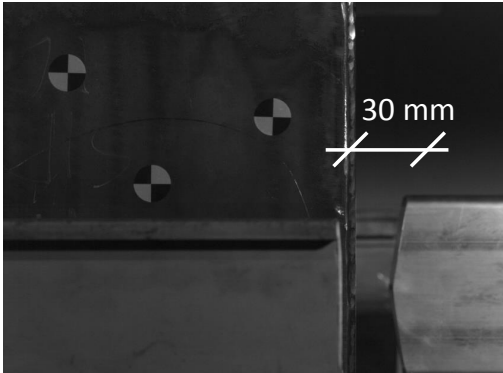


**Figure 6.25:** Profile with gap.

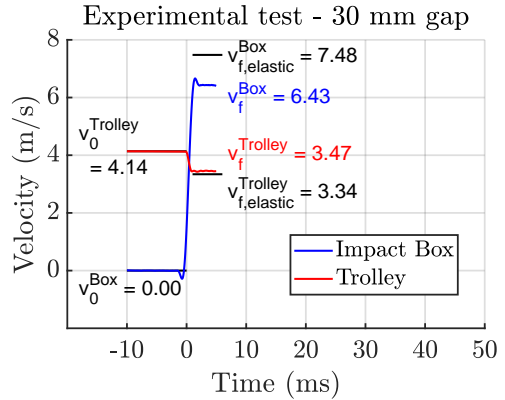


**Figure 6.26:** Velocities gap test.

and the theoretical benchmark. This reads  $CoR = -(v_f^{Trolley} - v_f^{Box})/v_0^{Trolley}$  [34]. For this particular experiment the CoR is 0.72, notably lower than the theoretical pure elastic impact where CoR equals to 1.00. A second method is to compute the loss in kinetic energy. The masses of the trolley and the impact box are 1407.2 kg and 150 kg respectively. Thus, 4.0 % kinetic energy is lost in the impact.

In both methods, the impact box is assumed to move in a linear direction with no rotation and corresponding rotational kinetic energy. This is a simplification and in conflict with the low-velocity tests in Section 6.6. However, for a high-velocity test, the rotational effects are considered less important.

Regardless of which method one considered, there is an apparent deviation between the experimental result and the theoretical pure elastic case. This suggests that there is some energy dissipation in the impact. To better understand this, a numerical simulation was carried out. The trolley was given the same initial velocity as in the experiment and the impact box was allowed to slide freely. At first the rig was modeled without the rig rotation shown in Figure 6.22. This yielded a CoR of 0.93 and 1.5 % loss in kinetic energy. A fundamental kinematic difference between the experiment and the numerical model was thus discovered.

For reference, an equivalent numerical analysis was carried out including the rotation of the crash rig and the off-centered impact. Some rotational effects were seen for the impact box in this analysis but not as significant as for the low-velocity case. This simulation also gave a CoR of 0.93 and a 1.5 % loss in kinetic energy.

Friction and plasticity are usual suspects when energy is dissipated. Both have been investigated in the experimental setup. The frictional forces have been found

negligible compared to the impact force. Also, the velocity of the impact box after impact in Figure 6.26 is constant, implying that virtually no friction from any surfaces slows the impact box down. Plasticity in the impact box is not seen numerically. No plastic deformation is seen in the physical impact box. The difference between the experiment and the simulation is believed to be linked to contact damping during the impact.

## 6.8 Kinematics of the System

When comparing the experimental crash box result with the numerical result a fundamental difference in the impact behaviour was found. As stated in Section 6.7, the numerical model predicts results closer to pure elastic impact than what is observed in the experimental test. For other crash box tests, this trait is seen not only seen for the initial impact, but also for the subsequent impacts following in the test. This section aims to illustrate the difference as well as looking into the consequences and importance with regards to the response of the crash boxes.

Comparing the kinematic of the system from an experiment and a simulation has been done to better understand the behavior of the crash rig. The experimental results are taken from one of the crash box tests presented in Section 6.9. The numerical results are taken from a numerical model based on this experiment.

Figure 6.27 shows the velocity and Figure 6.28 shows the displacement of both

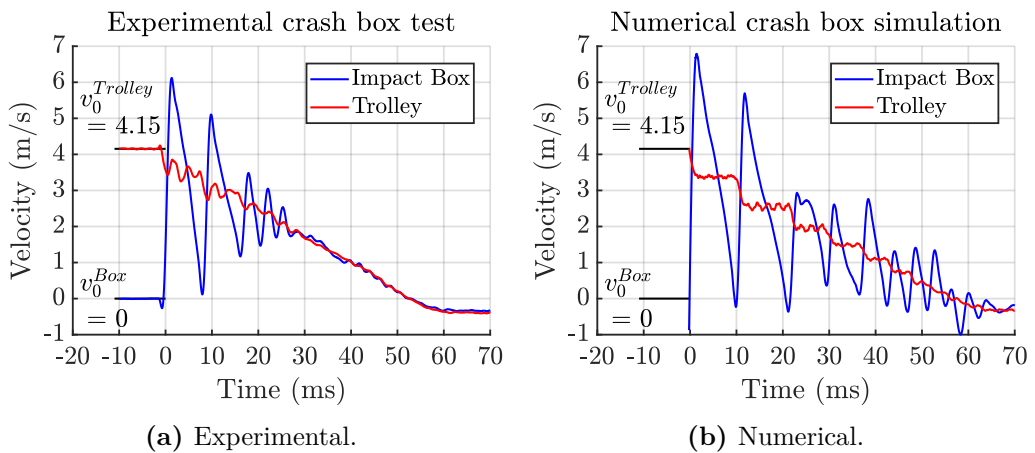


**Figure 6.27:** Velocities of impact box and trolley.

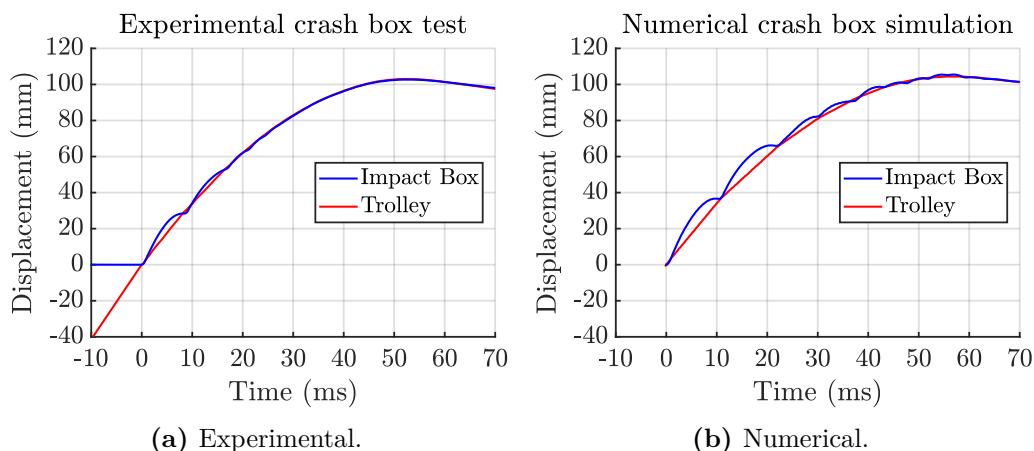


**Figure 6.28:** Displacements of impact box and trolley.

the box and trolley as a function of time for both the experimental test and the numerical simulation. The initial velocity of the trolley is the same.

It is evident that the experimental impacts are more damped than the numerical, consequently leading to the trolley and impact box moving together after about 30 ms. This tendency is not seen in the numerical simulations. The exact energy dissipating mechanism has not been identified, but it is believed to be because of contact damping in the impacts.

Several suggestions and attempts were explored in the numerical simulations to include the damping effects. In Section 6.8.1 a brief description is given and results are presented from these attempts.

### 6.8.1 Introducing Damping in the Numerical Simulation

#### Yield Stress of the Impact Box

Though it was thought to be unlikely, yielding in the impact box could explain energy being absorbed in the system. However, due to plastic hardening, this would mean the subsequent impacts should not dissipate energy due to an already strain-hardened material. Simulations were carried out to get a rough idea of what the yield stress of the impact box needed to be to get a corresponding velocity and coefficient of restitution after the first impact as in the experiment.

Figure 6.29 shows how the velocity of the box after the initial impact varies due to yielding of the box. To achieve the same velocity and coefficient of restitution

the yield stress must be reduced to just above 100 MPa, which is far below the actual yield stress of 420 MPa.

### Bulk Viscosity

The linear bulk viscosity term included in ABAQUS/Explicit helps to damp out high frequency oscillations and introduces damping associated with volumetric straining. No effects were seen when this parameter was changed.

### Contact Damping

By allowing soft kinematic contact, that is allowing penetrations of surfaces; a contact damping force can be introduced in Abaqus/Explicit. The damping force is a function of the damping coefficient and is proportional to the relative velocity of the surfaces during overclosure. The damping force is given as:

$$f_{vd} = \mu_0 A v_{rel} \quad (6.4)$$

where  $\mu_0$  is the damping coefficient,  $A$  the contact area and  $v_{rel}$  is the relative velocity between the penetrating surfaces. Using a linear pressure-overclosure law with slope 1 and damping coefficient 5, a similar initial velocity was achieved. However, due to the slope, a large overclosure of 5 mm followed, which is deemed too great. The penetration of surfaces can be seen in Figure 6.30, where some elements of the impact plate are removed for illustration purposes.

Introducing contact damping was found to work, however, to get results close to the experimental ones without

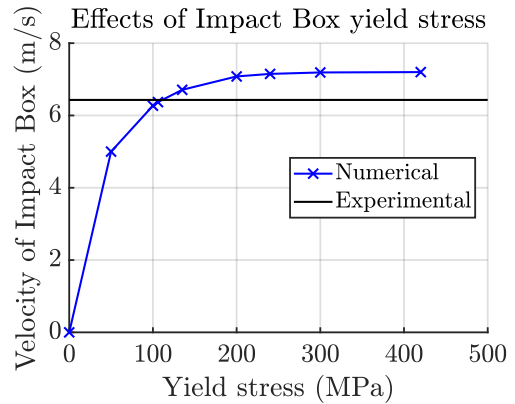


**Figure 6.29:** Non-physical yield stress of the impact box is needed to reduce box velocity.

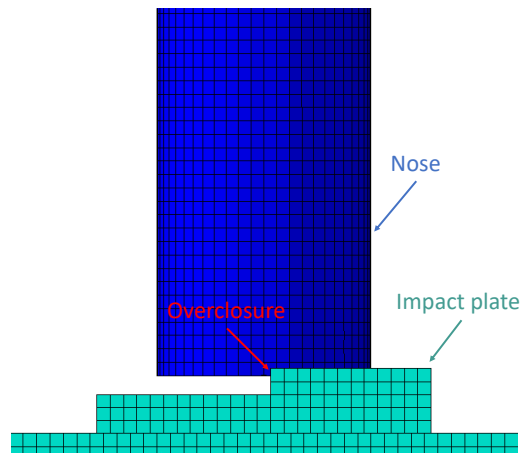


**Figure 6.30:** Penetration of nose and impact plate in simulation.

large overclosures, a high damping coefficient is needed which ruins the critical time step and makes the simulations too expensive to run.

### Rayleigh Damping

Rayleigh damping introduces both mass and stiffness proportional damping to the system. The mass proportional damping,  $\alpha_R$ , generally damps out lower frequencies and the stiffness proportional damping,  $\beta_R$ , damps the higher frequencies. From the following expression the critical damping fraction for the  $i^{th}$  mode can be seen:

$$\xi_i = \frac{\alpha_R}{2\omega_i} + \frac{\beta_R\omega_i}{2} \quad (6.5)$$

where  $\omega_i$  is the  $i^{th}$  mode natural frequency.

As the  $\alpha_R$ -factor introduces damping forces for absolute velocities, the velocity of the impact box is damped even after the impact which is not desirable. Instead, using a higher stiffness proportional damping could help damp out during impact, but this will also ruin the stable time step and cause the simulation to be too computationally expensive.

### Artificial Energy Absorbing Buffer

By having a deformable buffer in front of the impact plate, energy could be dissipated through different loading/unloading response of the buffer, subsequently introducing damping during all impacts.

#### *Viscoelastic Behavior*

Initially, an elastic response was tested as permanent deformations of the buffer was undesirable. As such, assigning viscoelastic material behavior to the plate was tested. To dissipate enough energy, the characteristics of the loading and

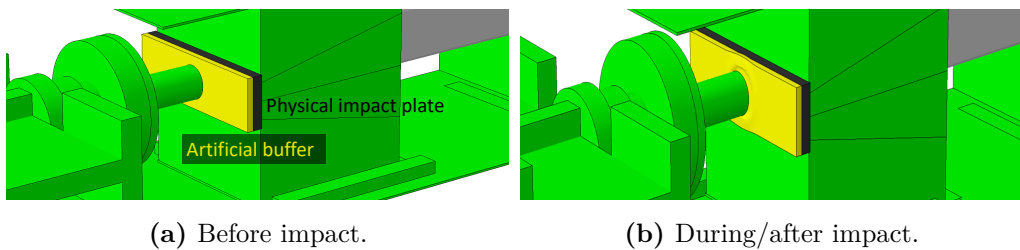


**Figure 6.31:** Introducing an artificial buffer.

unloading response should be quite different. No parameters were found to give the desired response properties.

### *Superelastic Behaviour*

The superelastic model (also referred to as pseudoelastic) in Abaqus is based on phase transformations of the material. That is the loading and unloading occur for different phases of the material. The idea was to take advantage of this and find parameters that would allow for enough energy absorption. No such parameters were found.

### *Elastic-Perfectplastic Behaviour*

Impact stresses for an elastic impact are given by Equation (6.1). For a material with no strain hardening, that is an elastic-perfectplastic material, impact stresses higher than the yield stress should result in plastic deformations of the buffer. This will damp the impacts as long as the velocity of the trolley is sufficient for the given Young's modulus and density. A Young's modulus of 210 MPa with density  $2 \text{ kg/m}^3$  gave a correct velocity after initial impact. However, as the velocity drops for each impact, the later impacts will not cause further plastic deformation of the plate.

Comparing Figure 6.28b and 6.32b, the damping effects of an energy absorbing buffer is clearly seen and is more similar to the experimental results, show in Figure 6.28a. A buffer with yield stress equal to 60 MPa and 70 MPa for respectively crash box and rim simulations were found to match the experimental kinematics.

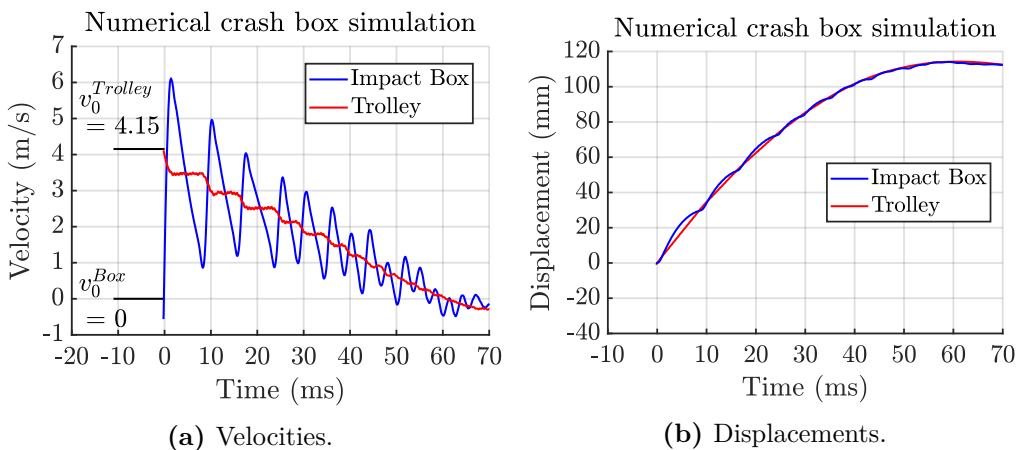


**Figure 6.32:** Numerical crash box simulation with buffer.

## 6.9 Validation Using Known Crash Boxes

The response and behavior of impact tested crash boxes are well known and documented for several cross sections and load scenarios. Crash boxes were therefore used for benchmarking and controlled testing of the rig. Numerical simulations are compared to the experimental results to assess the robustness of the validation method used to estimate the crushing force. In addition, the estimated forces from experiments are compared to results obtained from experiments previously done.

Costas et.al [35] did extensive work on double-chamber AA6005-T6 profiles under quasi-static and dynamic impact loading conditions. A damage regularization model was proposed and validated for shell elements subjected to large bending and membrane deformations in order to reduce mesh dependency of the Cockcroft-Latham failure criterion. The same double-chamber profile was tested in the crash rig and simulated with a material card provided by Costas, found in Appendix D. Geometry is found in Figure 6.33. Costas' experimental results and his numerical model are assumed true and are taken as the benchmark for the tests carried out for this thesis.

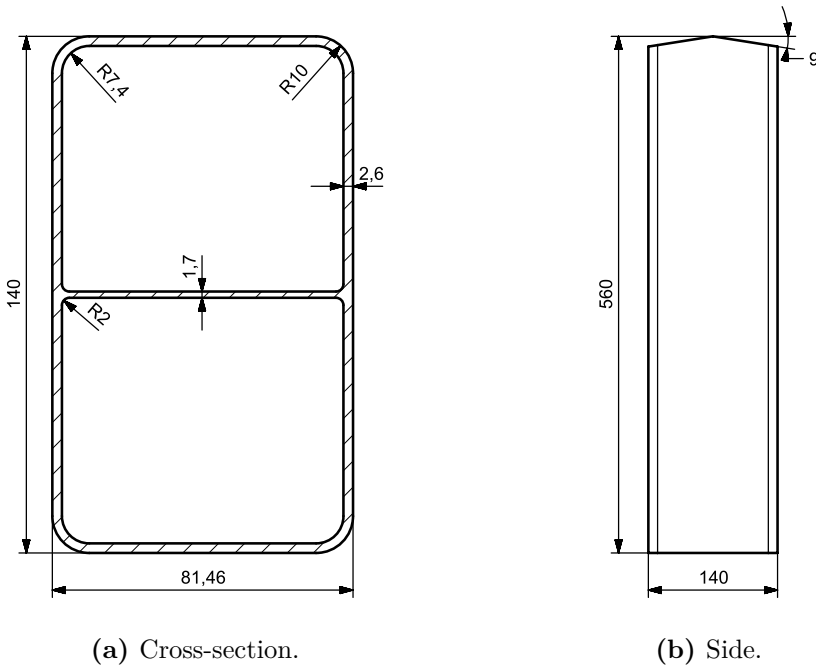


**Figure 6.33:** Dimensions of double chamber profile.

The double-chamber profile exhibits two main collapse modes, one asymmetric and one symmetric where the latter has lower energy absorption per unit length. Both modes are seen in the experimental tests, whereas the symmetric deformation mode is predominately seen in the numerical simulations. The symmetric collapse mode is caused by failure of the middle wall.

### 6.9.1 Experimental Validation of the Force Estimation Scheme

Through simulation of the rim impact in Section 5.2, it was found that the force estimation scheme presented in Chapter 4 is valid. To experimentally check the validity of the concept, and ensure its applicability for use in physical tests of rims, dynamic crash box tests have been conducted. These crash boxes are tested in the rim crash rig and compared to the experiments carried out by Costas.

Costas' experiments did not include the impact box, but the nose of the trolley impacted the specimen directly. This is a simpler method of testing because the trolley crushes the specimen continuously rather than repeated impacts on the impact box. The force impulses caused by repeated impacts are eliminating, and thus, fewer uncertainties in the recorded crushing force. This reduces the need for filtering and the crushing force can be taken from the load cell signal directly, instead of estimating it. The load cell signal is therefore reasonably assumed to be the true crushing force acting on the specimen.

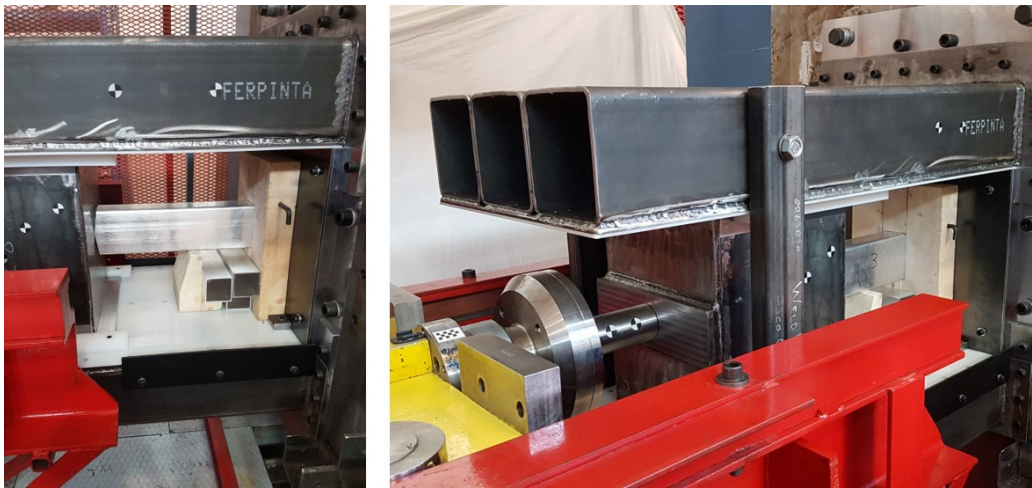


**Figure 6.34:** Images showing crash box test setup.

The experimental test setup used for testing crash boxes is shown in Figure 6.34. Since the rig is designed for rims, a less sophisticated support for the crash boxes was made in wood. The support constrains the crash box at the reaction wall. A total number of three crash boxes were tested, all with an initial trolley velocity of approximately 4 m/s. The high-speed camera setup is as described in Section 6.3.

In Figure 6.35, the force vs. displacement and mean force vs. displacement for the three tests as well as Costas' results are shown. It is emphasized that the force estimation scheme has been used to estimate the force for the three tests, with the same filter as previously presented. Clearly seen, the results from the tests conducted are in good accordance with previous tests. Initial stiffness, mean force level and general trends are the same. This experimentally proves that the crushing force can be obtained by the proposed estimation method. The conclusion that the test concept is valid and can be used to estimate the crushing force in the rim tests is drawn.

The discrepancy between test 1 compared to test 2 and 3 is due to the different deformation modes. Test 2 and 3 deformed with a combination of the asymmetric high energy mode and lower energy symmetric mode, while test 1 only had the symmetric mode. Thus, test 1 resulted in larger displacement and lower mean force. Both modes were also seen in the tests done by Costas.

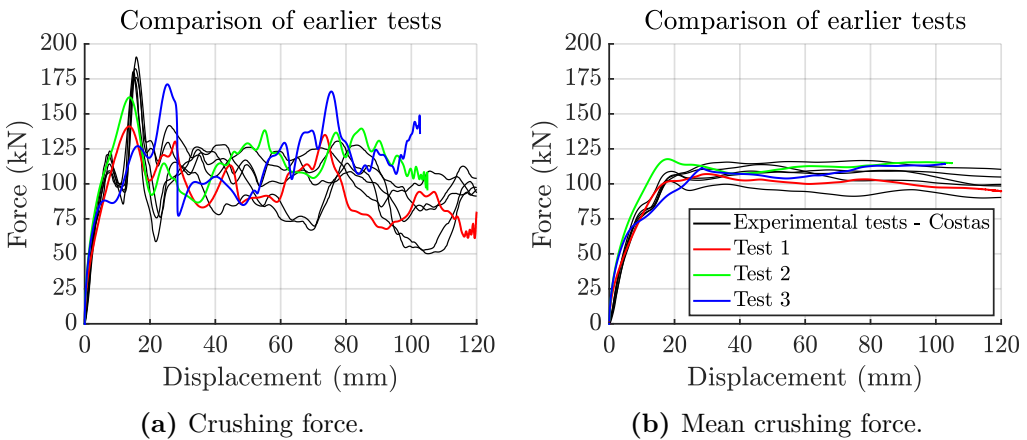


**Figure 6.35:** Experimental crash box tests compared to tests by Costas.

### 6.9.2 Numerical and Experimental Comparison

The estimated force is assumed to be a valid estimation of the contact force between the impact box and test specimen. This holds for both numerical simulations and the experimental tests. Based on this, the accuracy of the numerical model has been checked by comparing the physical tests to simulations of the crash box using a full numerical crash rig model and applying the material card provided by Costas. The through-thickness damage regularization model was used to model the crash box.

Further, the importance of the numerical damping described in Section 6.8.1, used to match experimental system kinematics, has been assessed. Damping is introduced by adding the artificial elastic-perfectplastic buffer to the system, shown in Figure 6.31.

The deformation mode found in the numerical simulations corresponds best to test 1. Thus, this test is the basis of comparison for the numerical model against experimental tests.

From Figure 6.36, it is seen that the numerical model can reproduce the experimental results to a reasonably good degree. The quality of the numerical result improves when damping effects are implemented. The mean force is close to being the same at the final displacement while the actual force varies to some degree. The force spikes seen in the simulations without the artificial buffer included are a consequence of the filtering and are not due to the numerical model itself. As the filters are set to specific window sizes, the filter and estimated force will be

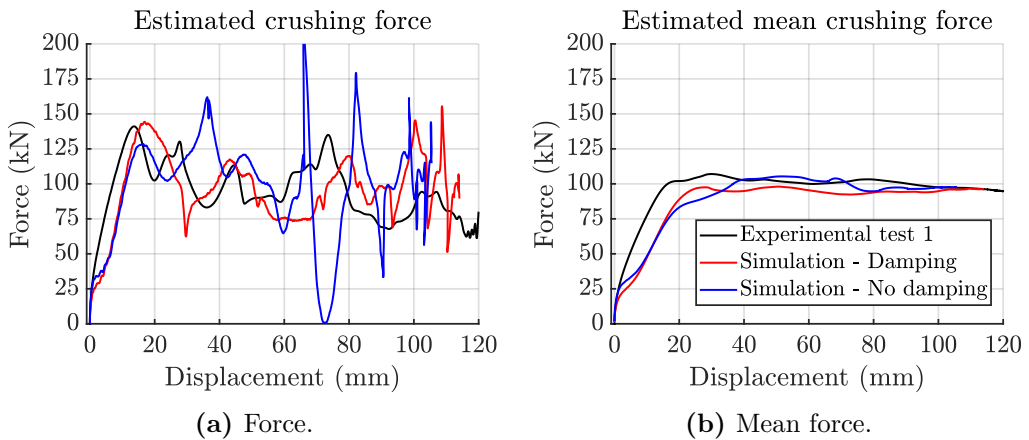
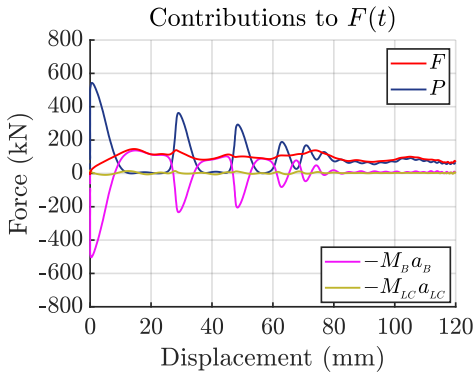
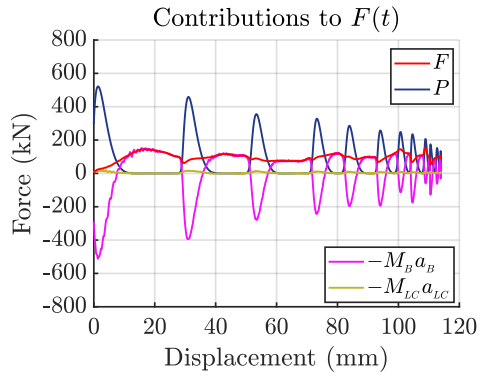


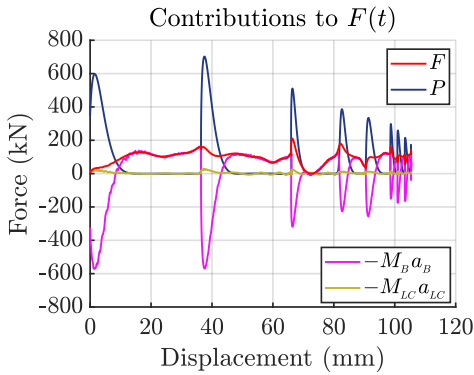
**Figure 6.36:** Comparison of numerical model with and without damping.



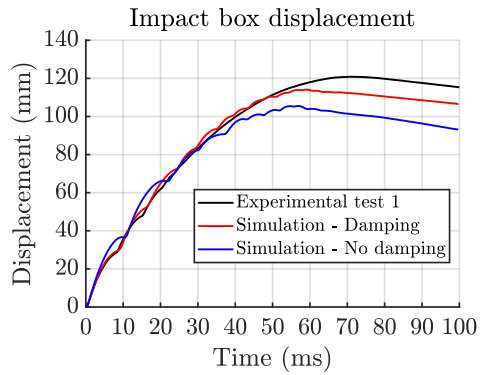
(a) Experimental test 1.



(b) Simulation including damping.



(c) Simulation excluding damping.



(d) Impact box displacement.



(e) Front view.



(f) Overview.

**Figure 6.37:** (a), (b), (c): Force Components, filtered values. (d): Displacement comparison. (e), (f): Comparison of crash box test 1 and numerical model with buffer.

sensitive to changes in impact frequency. For simulations that do not include a buffer, the impact frequency increases throughout the simulation.

The estimated contact force,  $F$ , is broken down to its force components and shown in Figure 6.37a, 6.37b and 6.37c. Although the estimated force is quite good for the simulation without damping, the incident at which the impacts occur and the value of the force peaks correspond much better for the simulation that includes the artificial buffer. Though it does not damp enough to get the trolley and impact box to move together as it does experimentally, including the buffer is enough to significantly improve the accuracy of the simulation. The improvement is even more clear when looking at the displacement vs. time curve in Figure 6.37d. The displacement history for the impact box matches when the buffer is included. The final deformation after crushing is shown in Figure 6.37e and 6.37f, where experimental test 1 is compared to the numerical simulation including the buffer.

The response of the crash box was previously assumed to be independent of the boundary conditions imposed from the impact box, i.e., how the box moves. A secondary approach to modeling the initial impact was introduced in the simulation. Instead of introducing damping, a simulation has been carried out with a reduced trolley velocity such that the initial velocity peak of the impact box matched the experimental velocity peak.

In Figure 6.38 the crushing force response is shown. Both force and mean force are considered the same for the two numerical approaches. Maximum displacement is lower when the trolley velocity is reduced because there is less initial kinetic energy is brought to the system. From this, it is concluded that the response

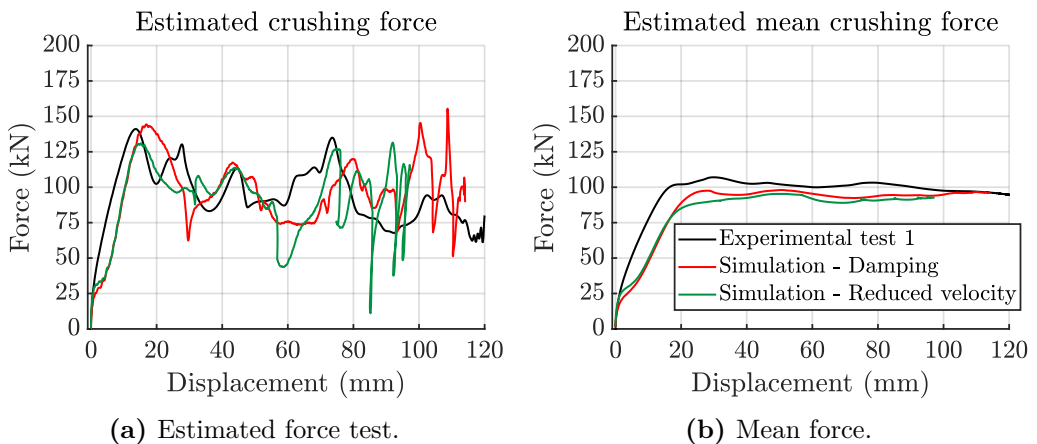


**Figure 6.38:** Damping vs. reduced velocity.

of the crash box is independent of the boundary condition that the impact box represents.

The crash box tests are, together with the numerical simulation described in Chapter 5, used to find the best filter which will be used for the rim tests. The results presented in this section takes the same zero-phase filter as used in Section 5.2. This filter is found to give the best results out of the filters tested. The response of the crash box using the remaining filters are presented in Appendix E.

### 6.9.3 Concluding Remarks from the Crash Box Study

Based on the experiments carried out using crash boxes and corresponding numerical simulations, valuable insight about the crash rig and test concept is gained. From an experimental point of view, the tests carried out yield results in accordance with the well-known response of the crash boxes based on the work done by Costas. Thus, it is concluded that the test rig design by Martinsen in fact behaves as intended. Despite some inaccuracies in the production and assembling of the rig, the estimated crushing force is concluded to be a good approximation of the actual force.

From the iterative work between physical testing and simulations, the kinematics of the crash rig is investigated and better understood. To be able to numerically model the contact damping in the impact between the nose of the trolley and the impact box, an artificial buffer is introduced. This buffer is found to improve the kinematic response while at the same time ensuring correct estimation of the crushing force.

Section 5.2 together with Section 6.9.1 has shown that the force estimation scheme presented in Chapter 4 indeed is a valid method for estimating the crushing force of a specimen tested in the test rig. Thus, the results presented in Section 6.10 from the rim tests are assumed valid as they are based on thoroughly checked assumptions and methods.

## 6.10 Rim Tests

In this study, experimental impact testing of rims have, in addition to equivalent numerical modeling, been the main area of focus. Previously described experimental work has been carried out to ensure trustworthy testing of rims. The test setup is one of a kind and not based on any standards.

A total number of four rims have been tested in the kicking machine. The trolley was accelerated to approximately 5 m/s. Exact velocity for each test can be found in Table 6.3.

The rim tested is the previously presented Audi Q7 ALY58988 10-spoke rim. The purpose of experimental testing was to estimate the force vs. displacement curve in dynamic crushing of rims. This is by itself interesting because it provides data regarding the rim. Furthermore, the experimental tests have been the foundation for the validation of the numerical model.

### 6.10.1 Rim Orientation

Two different rim orientations have been tested. The spoke section is fairly symmetric, however, the geometrical difference between short and long spokes has been investigated. The first three rims were tested with a short spoke facing the impact box, shown in Figure 6.39. The fourth rim was tested with a long spoke facing the impact box, shown in Figure 6.40.

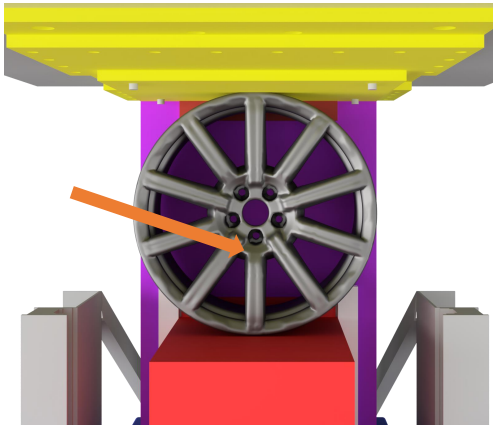


**Figure 6.39:** Short spoke facing impact box – "Short spoke configuration".

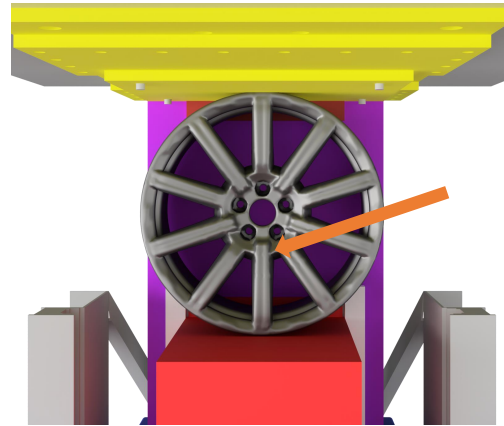


**Figure 6.40:** Long spoke facing impact box – "Long spoke configuration".

### 6.10.2 Estimated Crushing Force

The rim crushing force has been estimated using the previously described method, presented in Chapter 4, with the post-processing technique presented in Figure 4.3, which is the same as used for the crash boxes. This include using the filter presented as filter 5 in Appendix B. In Figure 6.41a, the force vs. displacement

curve for all tested rims are shown. Similarly, in Figure 6.41b the mean force vs. displacement is shown. The forces are plotted up to maximum displacement for the respective rim.

By inspection of Figure 6.41a and 6.41b several interesting observations are made. Extensive inspection of both the figures as well as the recorded visual deformation history has been carried out to arrive to these observations. In Section 6.10.3 deformation history for the rims are shown. The observations are listed below:

1. The overall trend of the force vs. displacement curve is the same for all rim tests. The first main peak between 20 and 25 mm corresponds to where the short spoke starts to buckle. Prior to this point, it is able to carry the axial load. The sudden drop in force after this point is explained by buckling. Sudden release of axial stresses to bending stresses weakens the spoke. A weakened spoke weakens the rim.
2. After buckling the short spoke is further compressed until fracture. For all rim tests, the short spoke fractured first at a displacement between 35 and 45 mm. After fracture, the rim bed must carry the load before the outer spokes begin to carry substantial loads.
3. The second main peak between 60 and 70 mm corresponds to the long spoke carrying its buckling load. When the rim is further compressed the long spoke fails due to shear fracture between the spoke and the rim bed.
4. The shear fracture of the long spoke occurs at around 70 mm for all rims. At this point, most of the initial kinetic energy in the trolley is dissipated. Although rim 2 and 3 experience a maximum displacement of more than 10 mm ( $\sim 15\%$ ) more than rim 1 and 4, this extra displacement is essentially "free of charge". After fracture, the long spoke is either torn apart from the rim or stuck between the bed and center part of the rim. If torn apart, the weak rim bed is easily deformed the extra 10 mm. If stuck, kinetic energy left in the system is absorbed by a small deformation of the long spoke.
5. All fracture may be classified as brittle fracture rather than ductile. This is expected due to the nature of a cast alloy.
6. In the experiments, fracture is also seen in the spokes not perpendicular to the impact surface. This is believed to be explained by significant tension in these spokes.
7. The mean force for rim 1 and 4 is almost 20% higher than for rim 2 and 3 in the later deformation. This suggests that two different deformation modes are experienced.

8. Rim 1, 2 and 3 were all tested with the short spoke facing the impact box. Rim 4 was tested with the long spoke facing the impact box. This difference in setup does not seem to affect the pattern or the magnitude of crushing force. By visual inspection of the deformation history for these tests, it is clear that the short spoke fails first then the long spoke fails.

### 6.10.3 Deformation History

The deformation history for rim 1, 3 and 4 is shown in Figure 6.42, 6.43 and 6.44. The camera recording deformation of rim 2 was not triggered and thus, these images are missing.

### 6.10.4 Images of Crushed Rims

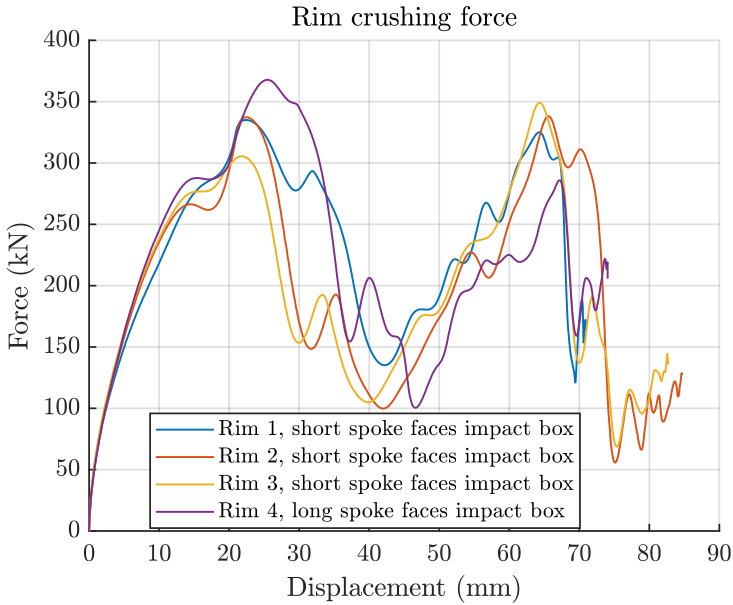
Images of the deformed rims are shown in Figure 6.45. All images are taken so that the impact box was impacting the rims from the bottom side in the images. The top part of the rims in the images was facing the reaction wall.

### 6.10.5 Energy Conservation

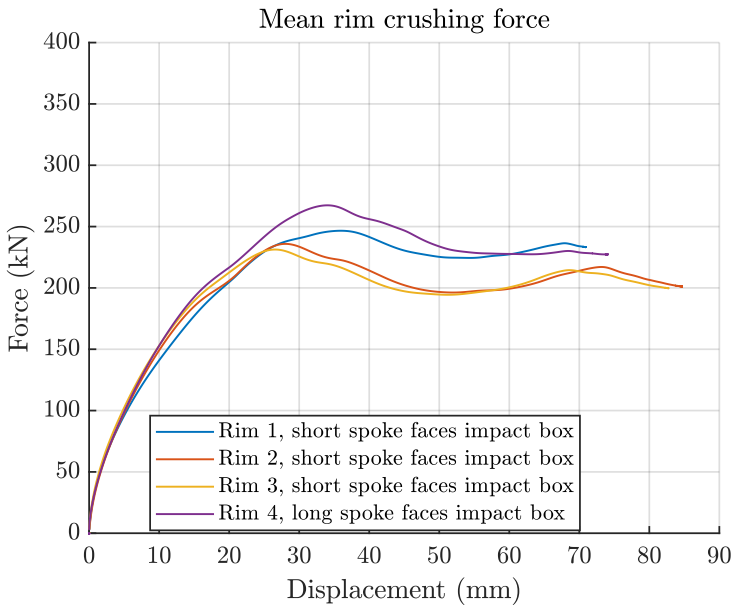
An easy way to validate the mean force, the upper limit can be computed and compared to the measured one at maximum displacement. The upper limit is defined by  $F_{mean}^{upper} = E_0/v_0$  where  $E_0 = 1/2 * m^{Trolley} * v_0^2$ . For consistency  $m^{Trolley} = 1407.2$  kg. This upper limit is equivalent to all kinetic energy being dissipated by deformation of the rim. For an actual physical test, the real mean force must be lower because some energy is dissipated through friction, heat, damping, etc. However, the underlying assumption in this study is that these effects can be neglected. In Table 6.3 the upper limit, as well as the measured mean force at maximum displacement and deviation between the two, are listed in the three rightmost columns. All measured means are lower than the upper limit. Also, all deviations are lower than 5 %, which is considered to be an indication that the measured mean force is the true mean force.

Rim	$v_0$ (m/s)	$E_0$ (kJ)	Maximum displacement (mm)	$F_{mean}^{upper}$ (kN)	$F_{mean}^{measured}$ (kN)	Deviation (-)
1	4.98	17.5	70.4	248.0	237.4	4.3 %
2	5.00	17.6	84.7	208.0	202.3	2.7 %
3	4.94	17.2	82.7	207.9	200.8	3.4 %
4	4.97	17.4	74.1	234.9	231.0	1.7 %

**Table 6.3:** Key metrics from rim tests.

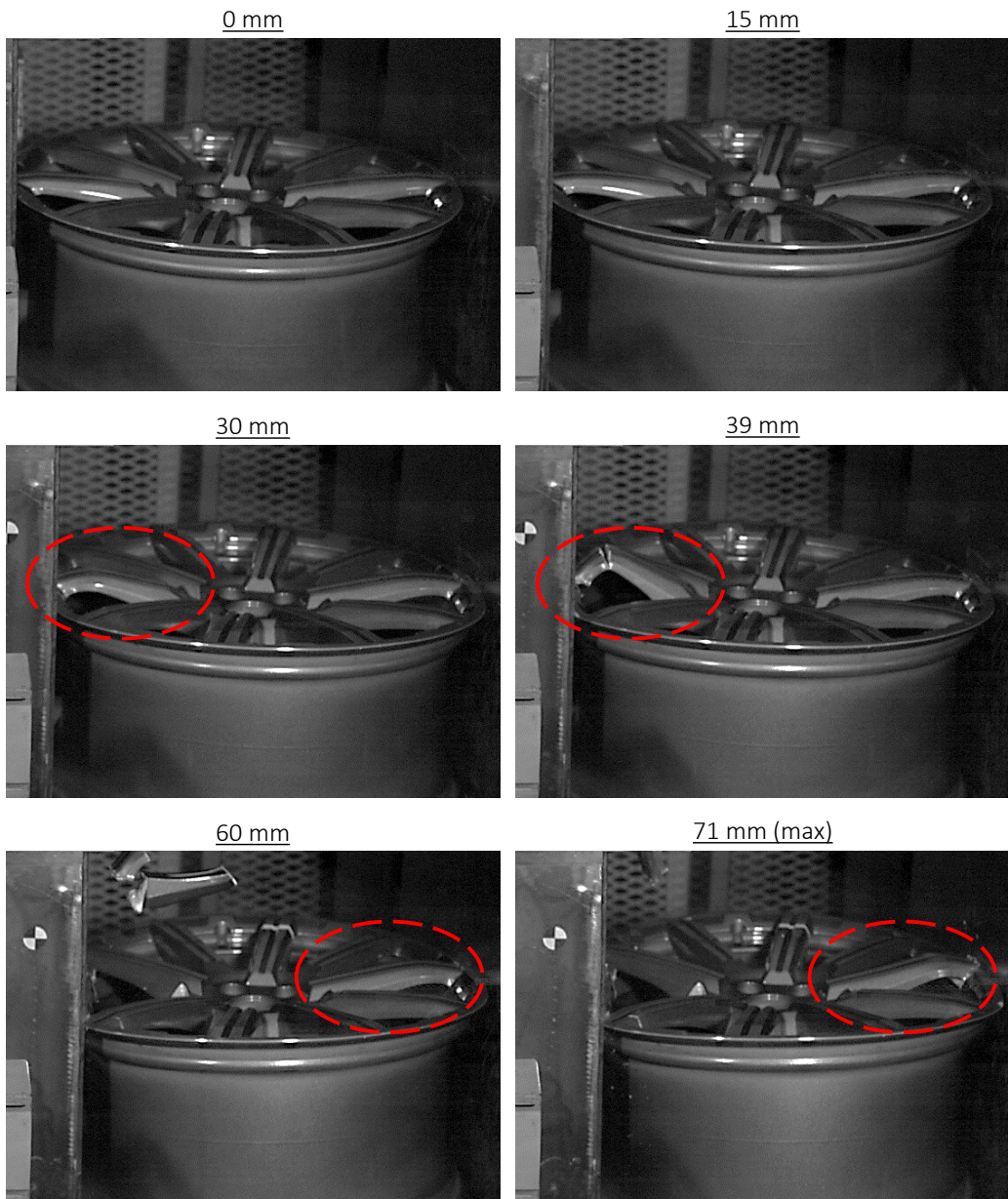


(a) Crushing force.



(b) Mean force.

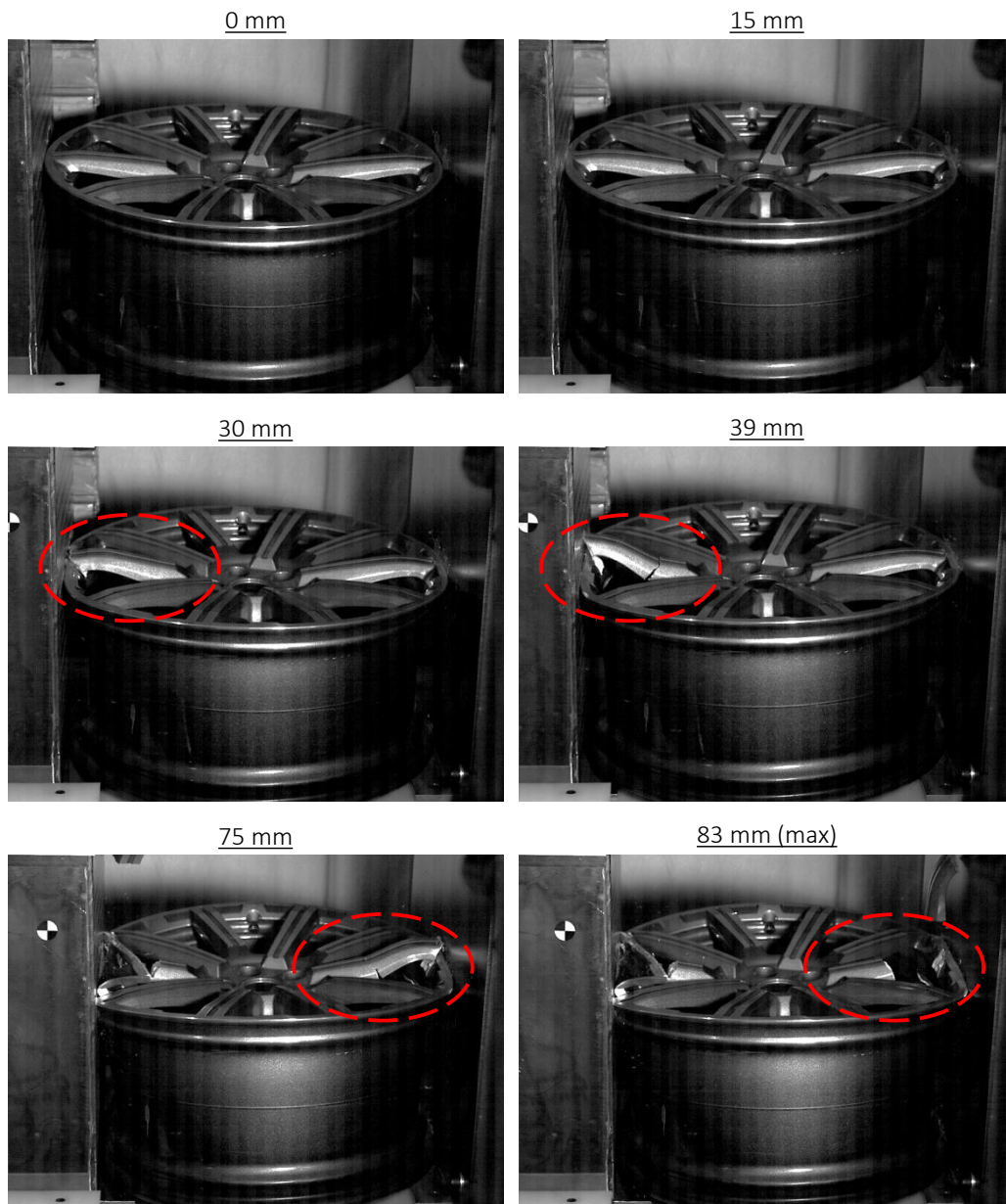
**Figure 6.41:** All experimental tests.

Rim 1 – Short spoke configuration

**Figure 6.42:** Rim 1. Visual deformation at given displacement.

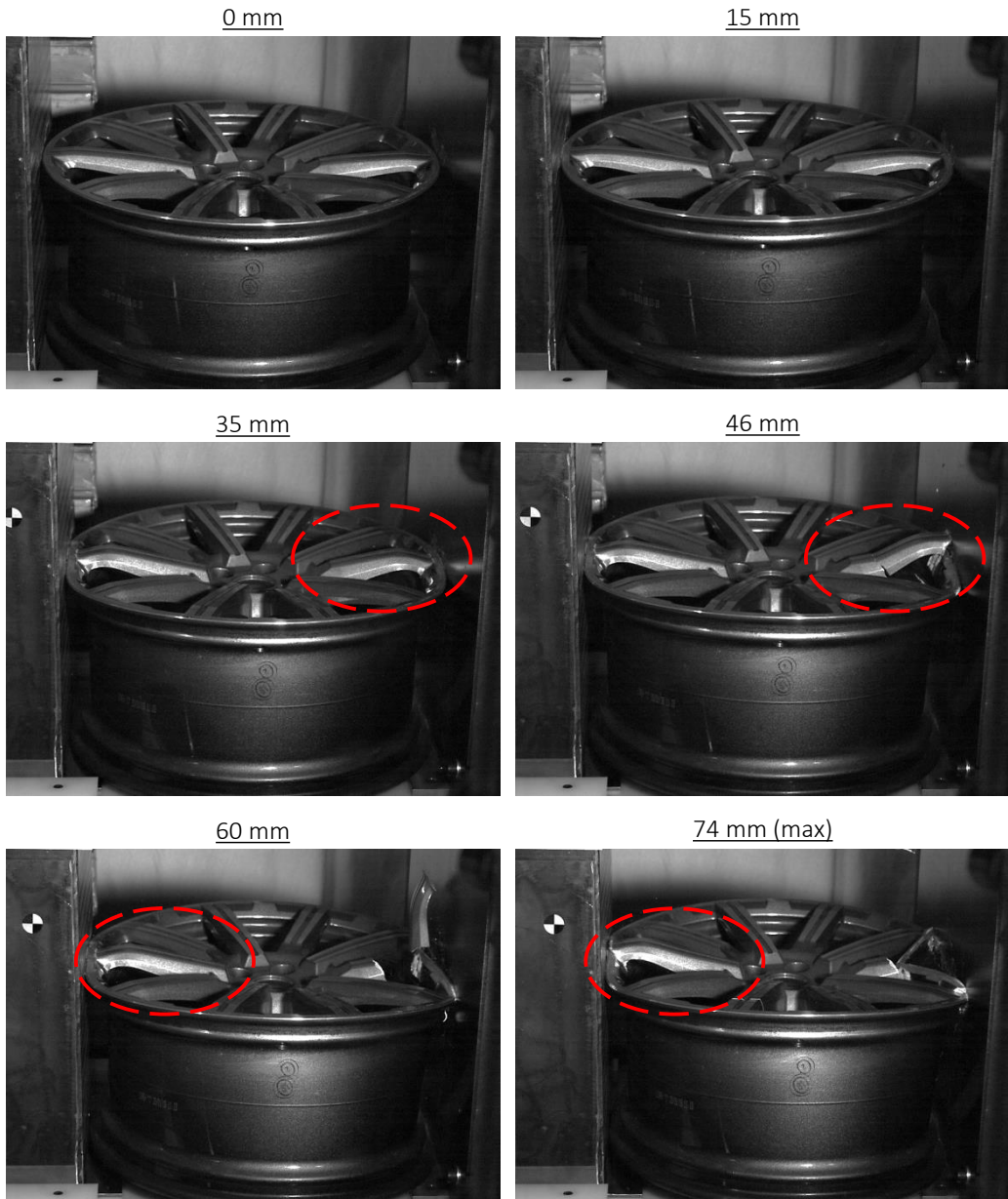
**Deformation sequence:** buckling of short spoke, brittle *bending* dominated fracture of short spoke (39 mm), buckling of long spoke, *shear* dominated fracture of long spoke (71 mm).

Rim 3 – Short spoke configuration



**Figure 6.43:** Rim 3. Visual deformation at given displacement.

**Deformation sequence:** buckling of short spoke, brittle *shear* dominated fracture of short spoke (39 mm), buckling of long spoke *shear* dominated fracture of long spoke (75 mm).

Rim 4 – Long spoke configuration

**Figure 6.44:** Rim 4. Visual deformation at given displacement.

**Deformation sequence:** buckling of short spoke, brittle *shear* dominated fracture of short spoke (46 mm), buckling of long spoke, *shear* dominated fracture of long spoke (74 mm).

Rim 1



Rim 2



Rim 3



Rim 4



**Figure 6.45:** Images of all rims after testing. Impact from the bottom side of the images.



## Chapter 7

# Validation of the Numerical Model

### 7.1 Comparison of the Estimated Crushing Force

An essential part of this study is to validate the numerical model by comparing simulations to experimental tests. The force estimation scheme, presented in Chapter 4, is utilized to obtain the force vs. displacement relations. The numerical base model, presented in Chapter 5, includes the experimental discoveries, presented in Chapter 6, to be able to make a reasonable comparison. Note that the numerical model used in Section 5.2 to validate the force estimation scheme is exactly the same as presented in this chapter.

The two main extensions of what is already described in the numerical base model, presented in Section 5.1, is the rotation of the test rig, shown in Figure 6.22, and the introduction of the artificial buffer, shown in Figure 6.31a. Further, the geometry and masses in the numerical model have been updated to best represent the experimental setup. This was done after experimental testing.

In Figure 7.1 the four experimental tests are plotted together with the numerical simulation. Both force vs. displacement, Figure 7.1a, and mean force vs. displacement, Figure 7.1b, are shown. All curves are plotted up to maximum displacement. The numerical force is estimated using the same method as in the experiments, not the available contact force in Abaqus. The same post-processing technique is applied for all tests and the simulation. The filter used is the same as in previously presented results in the thesis, that is filter 5 in Appendix B. Comparisons using all other filters are shown in Appendix F.

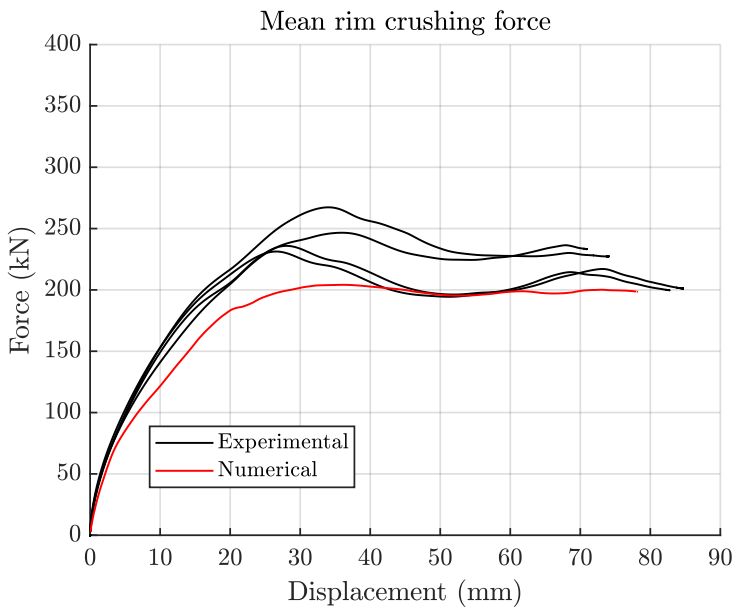
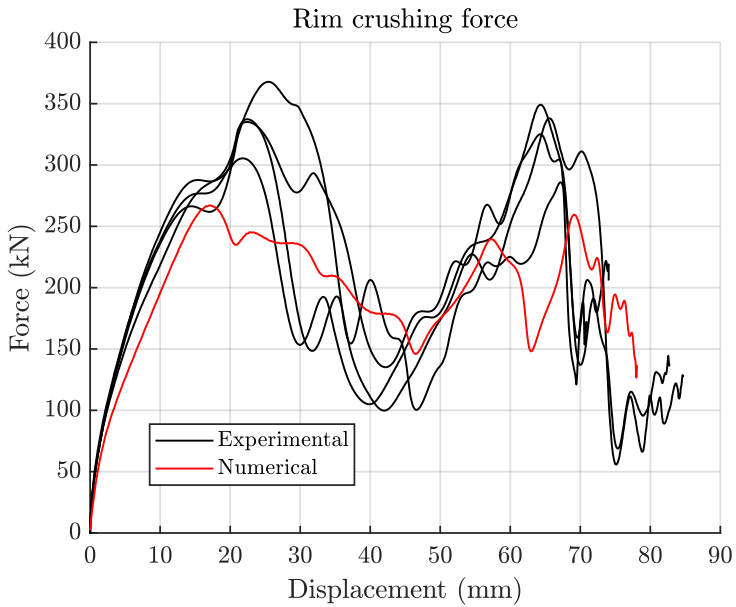


**Figure 7.1:** Numerical base model compared to experimental tests.

By inspecting Figure 7.1a and 7.1b, and comparing the simulation to the experiments, it is clear that the numerical model is able to capture the physical system to some extent. However, both the numerical force and mean force are deviating from experiments. The two most significant peak forces in the physical tests, corresponding to the instance just before buckling of respectively the short and long spoke, is not captured correctly numerically. The first peak force is, on average, approximately 70 kN (20%) too low. This is considered to be a non-negligible deviation, especially if the simulation were to be used for design. Comparing the mean force also yields the conclusion that the numerical force is too low. Although filter boundary effects are important for the first phase (displacement less than 10 mm) the force curves are *comparable* because the same filter is used. For displacements less than 15 mm the slope of experiments and the simulation is similar. Thus, the initial stiffness is captured. Furthermore, the mean force is equal or lower for all displacements. The numerical model may therefore be described as too soft. This is untypical in FEA. Later discussion on deformation mode, Section 7.2, aims to explain this.

When comparing mean force at maximum displacement, one observes that this metric is captured correctly in simulation compared to two of the experiments. However, this is an alarming result since the maximum displacement is lower numerically. Thus, a substantial amount of energy is dissipated in the simulation that is not seen experimentally. In the simulation, the rim dissipates 15.51 kJ. For the experiment with the largest maximum displacement, the rim dissipates 17.00 kJ. A difference of about 1.50 kJ. From Section 5.3 it was found that a significant amount of artificial strain energy (ASE) is introduced in the simulation to suppress hourglassing. In this simulation at maximum displacement, the ASE is 1.65 kJ. Thus, it is reasonable to state that ASE contributes to some of the differences between experiments and simulation. ASE is a problem of concern in this study.

## 7.2 Comparison of Deformation Pattern

To further investigate why the numerical rim behaves softer than the physical rim, the deformation history is compared. In Figure 7.2 and 7.3 the deformations are shown at the instance of fracture at respectively short and long spoke. A full deformation sequence is shown in Appendix G. Despite the image resolution being poor, and details are difficult to capture, the visual comparison is found to be of great use. Recall that the images from the test of rim 2 were lost.

The most interesting observations from the comparison are what happens concerning buckling and fracture. During the first phase of deformation, the crushing force builds up, before reaching the first peak. Up to 15 mm of deformation the numerical model reproduces the experimental results to a satisfying extent. The slope of the force curve is the same.

In addition to the first peak load not being captured in the numerical model, another deviation is seen when deformations are compared. Both in the experiments and the simulation the short spoke starts to buckle at this first peak load. The difference is how rapid the spoke buckles and how it fractures. Seen in experiments the short spoke buckles more rapidly than in the simulation. Thus, the slope of the force curve is steeper. Further, in experiments the short spoke undergoes a sudden brittle fracture. This occurs after buckling and corresponds to the minimum force between the two main peaks. In the numerical model, the less rapid buckling also intervenes with the fracture. From the first peak load, the buckling and fracture coincide at a slower rate. Element erosion is used to model fracture. For reduced integrated elements, only one integration point is used and failure must occur here for elements to erode. When the short spoke buckles, it undergoes bending which accumulates damage in the integration point too slowly.

After reaching the minimum force between the two main peaks, the force once again builds up. This is seen both in experiments and simulation. The same phenomena as for the short spoke is seen but for the opposite long spoke. In experiments the force builds up before the long spoke undergoes sudden buckling before fracture. Numerically, buckling and fracture occur simultaneously.

Another buckling and fracture-related observation is the order of occurrences. In the experiments it is found that the short spoke buckles and fractures before buckling of the long spoke is initiated. This is independent of whether the short or long spoke faces the impact box. In the simulation, this pattern is captured.

By comparing the deformation sequence, differences in fracture mode is observed. Experimentally two fracture modes are seen for the short spoke. For rim 1 the short spoke fractures in a bending dominated mode. For rim 3 and 4 a shear dominated mode is seen. This is an experimental difference which is believed to be explained by the stochastic behavior of the cast alloy. Fracture of the long spoke is shear dominated in all experiments. In the simulation fracture of both short and long spoke is found to be bending dominated. The shear mode is not seen. This is a significant deviation in the numerical model and suggests that the formulation of fracture could potentially be better.

Fracture of short spoke

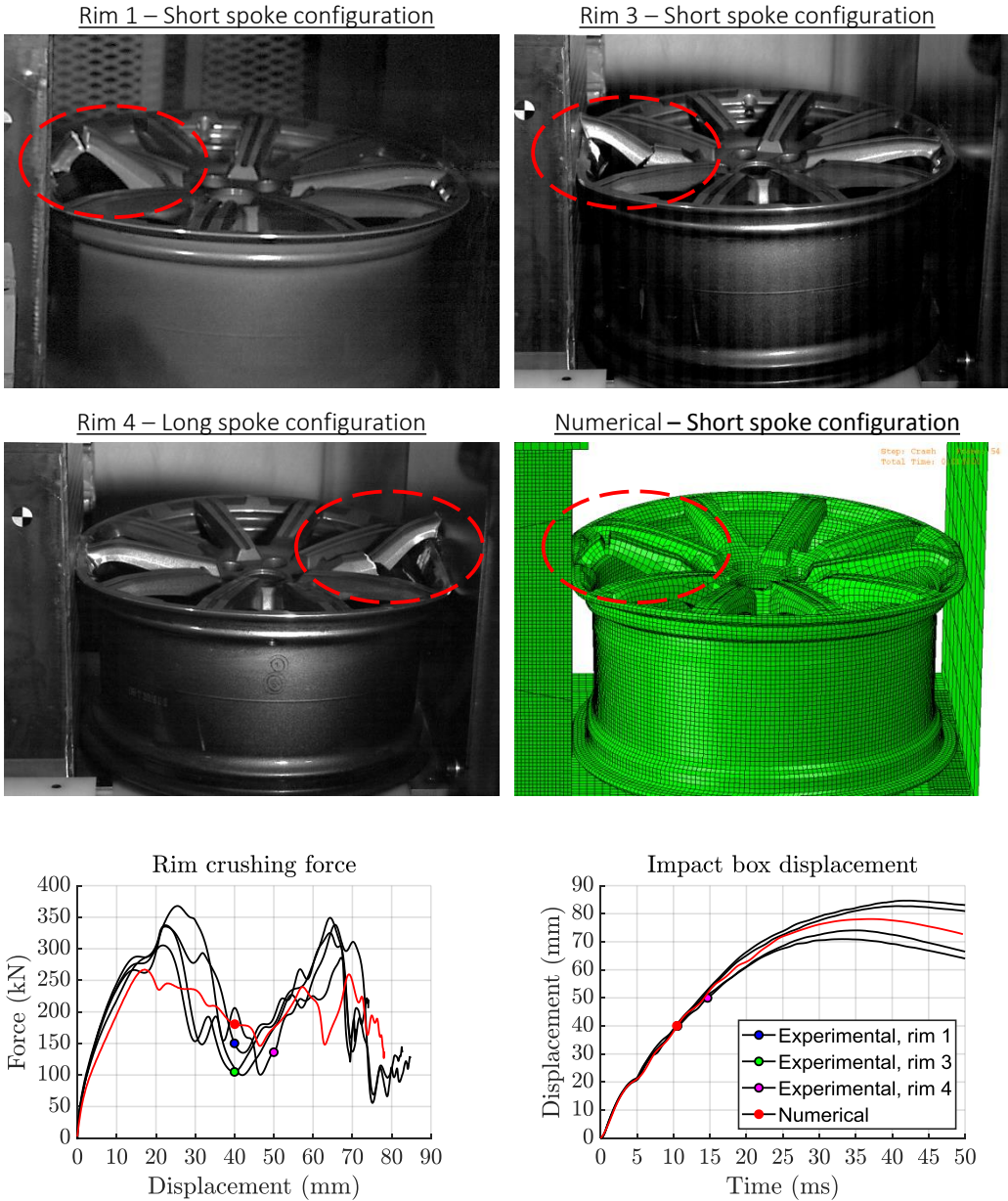
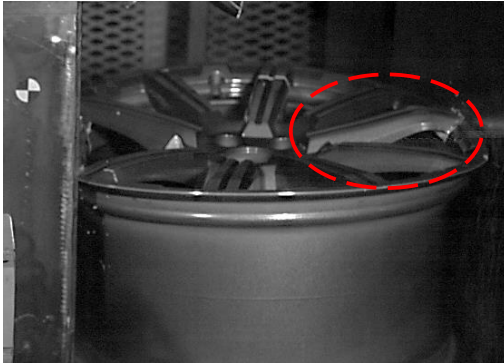


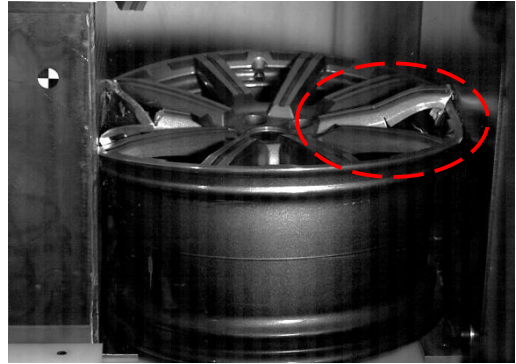
**Figure 7.2:** Comparison of experiments and simulation at the the point of short spoke fracture. Note the fracture mode within the dashed ellipses.

Fracture of long spoke

Rim 1 – Short spoke configuration



Rim 3 – Short spoke configuration



Rim 4 – Long spoke configuration



Numerical – Short spoke configuration

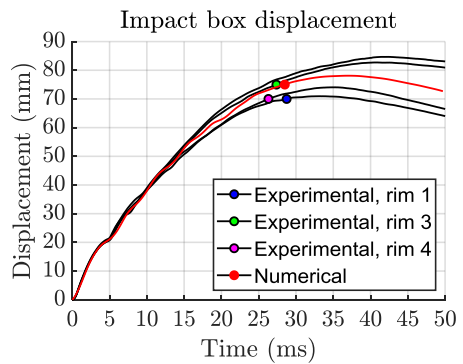
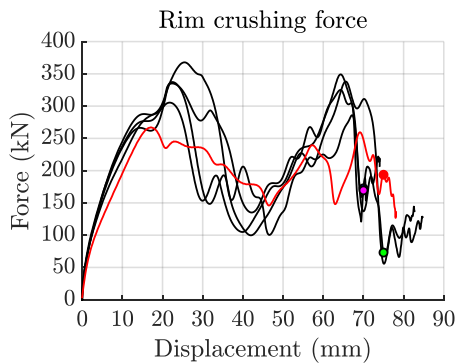
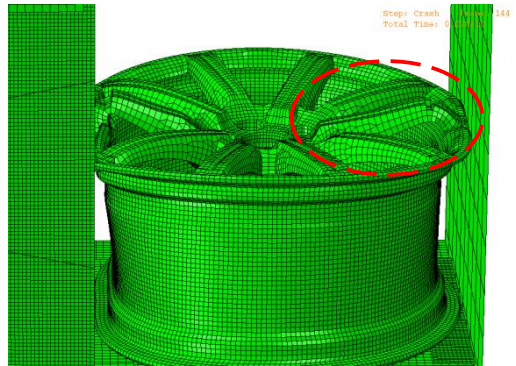


**Figure 7.3:** Comparison of experiments and simulation at the the point of long spoke fracture. Note the fracture mode within the dashed ellipses.

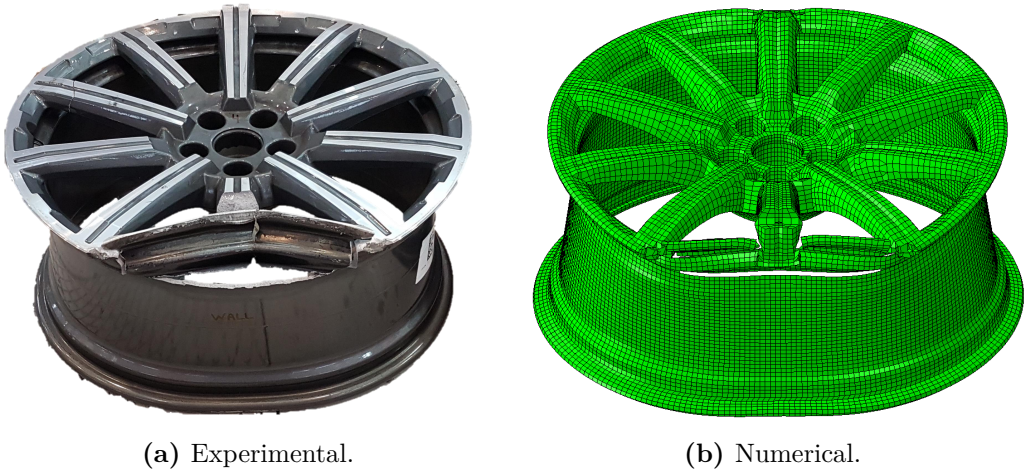


**Figure 7.4:** Plastic deformation and fracture of spokes and rim bed.

Figure 7.4 is shown to emphasize fracture of the rim bed. As can be seen, the model is able to represent important behavior such as plastic deformation and failure of the spokes and rim bed. However, the short spoke does not completely fail, as is the case in the experimental tests. As such, the rim bed fracture is not as large as seen experimentally. When the short spoke fails the brim of the spoke section completely collapses inwards resulting in large fracture of the rim bed.

From the study of the deformation sequence, it is found that general trends are well captured in the numerical model. The order of buckling is found to match experiments. Fracture is, to some extent, also captured in a reasonable manner. However, details in comparison have revealed important differences between experiments and simulation. This explains the deviations in the force vs. displacement curves.

### 7.3 Comparison of Kinematics

A comparison of numerical and experimental crushing force showed the presence of deviations in the numerical model compared to experiments. The comparison of deformation mode indicated an error in the modeling of the rim. To further assess what might be done to correct the model, it has been found useful to study the overall kinematics of the system.

In Figure 7.5 the measured displacements and computed velocities of the impact box and the trolley are shown. Numerical results are compared to the experimental results. Velocities are obtained by differentiating the filtered displacements. Without studying the details, it is clear that the kinematic trends are captured well in the numerical model. The deviation in maximum displacement is considered to be within the stochastic range. Further, the time at which maximum displacement occurs is for practical purposes the same. It is also seen that the trolley hits the impact box a repeated number of times before they start to move together. The numerical model captures the instances in time at which impacts occur. However, in the experiments, there are fewer repeated impacts. Despite this, the differences in kinematic behavior are not considered to be of relevance when comparing the estimated rim crushing force.

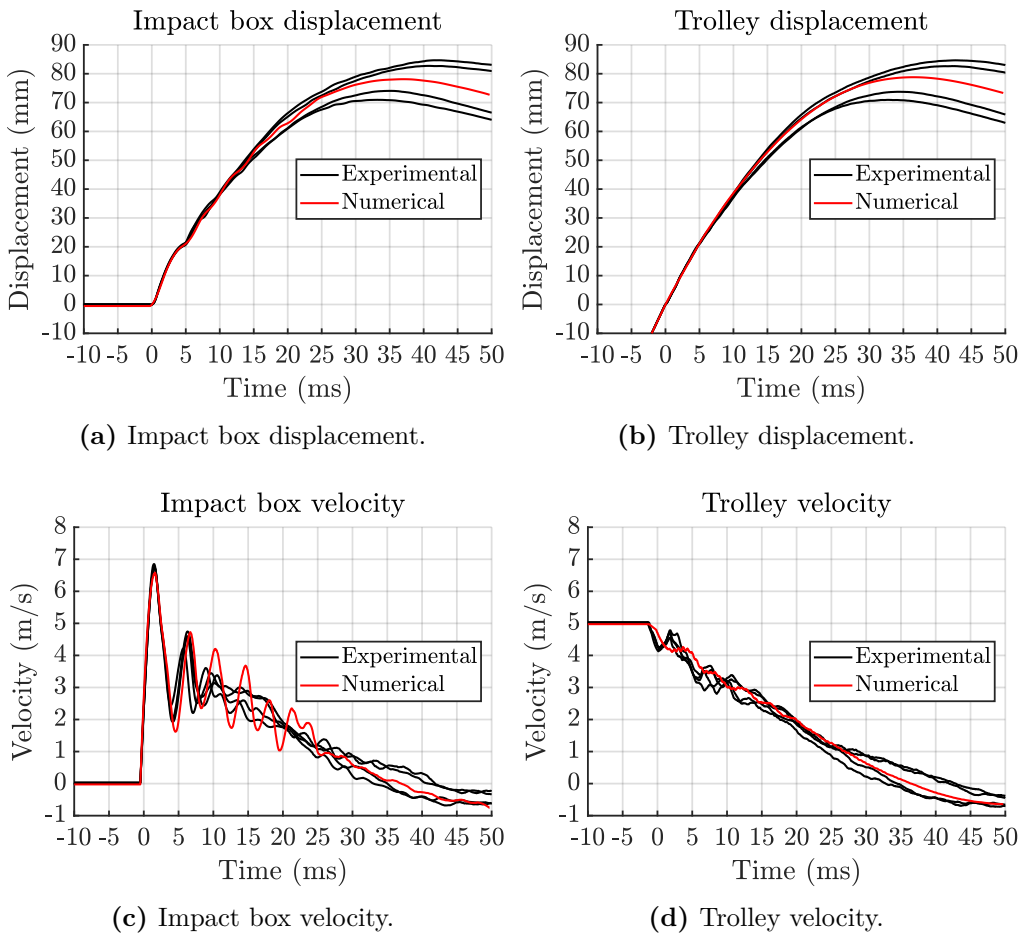


**Figure 7.5:** System kinematics, numerical simulation compared to experimental tests.

A close study of Figure 7.5a shows the displacements in the simulation, as well as the experiment tests, start to deviate at about 15 ms equivalent to 50 mm displacement. By inspecting the crushing force shown in Figure 7.1a, and the visual deformation shown in Appendix G, it is believed to be because of deformation mode. At this instance in time, about half of the initial kinetic energy is dissipated, and system velocities are lower. With lower velocities, a difference in crushing force yields more response in kinematics.

A lingering question is: How can kinematics be correctly captured but not the crushing force? The explanation is found by studying Equation (4.6). The force between the rim and the box,  $F(t)$ , is just a part of the expression describing the displacement of the impact box. Thus, different combinations of the forces acting on the box that sum up to the same must produce the same displacement of the impact box.

From this, the system's kinematics are overall well captured in the numerical model. To improve the accuracy of the rim response it is clear that investigation of the rim should be the area of focus. Thus, in Chapter 8, a parametric study is carried out.



## Chapter 8

# Numerical Parametric Study

### 8.1 Purpose of Parametric Study

From the validation of the numerical model in Chapter 7 it has been established that a parametric study should be carried out to better understand the numerical response of the rim. In addition, a parametric study is desired to better match the force vs. displacement curve estimated in experiments. The influence of relevant parameters have been investigated and are presented in this chapter. The reader should be aware of the challenge concerning the running time of simulations. The numerical model is complex and computationally expensive and is found to be a limitation when carrying out the parametric study.

### 8.2 Statistical Analysis

To investigate the probabilistic capability of the numerical model a statistical analysis has been conducted. All simulations take the base model presented in Section 5.1 including experimental discoveries. Thus, the same model as used for numerical validation in Chapter 7. A total number of 50 simulations have been carried out. All simulations with different initial damage distribution for the spoke elements, where all damage values come from the same underlying probability distribution.

In Figure 8.1 the average value for the estimated crushing force is plotted as well as  $\pm 1$  and  $\pm 2$  standard deviations (std). The statistical properties are unique for all given displacements. Numerical results are plotted up to the lowest maximum displacements among these 50 simulations and compared to experiments.

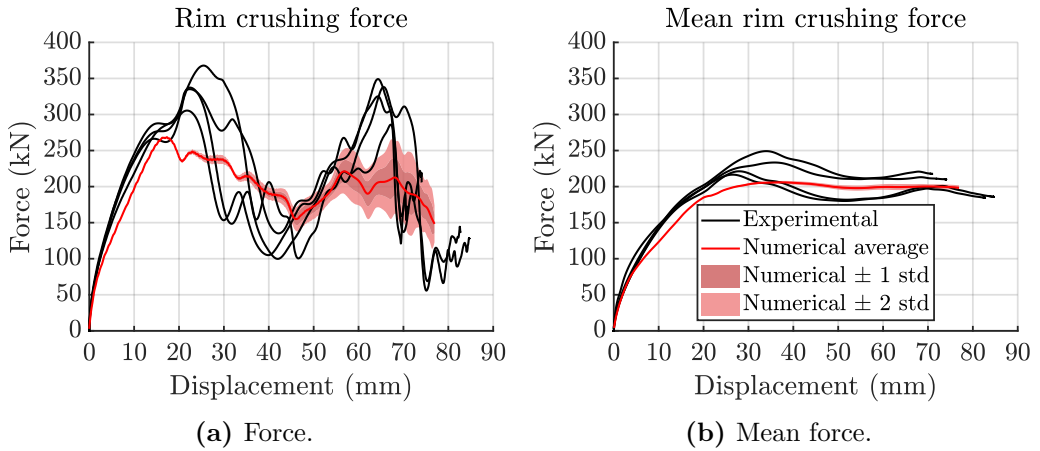


**Figure 8.1:** Statistical results of 50 simulations with different initial damage distribution.

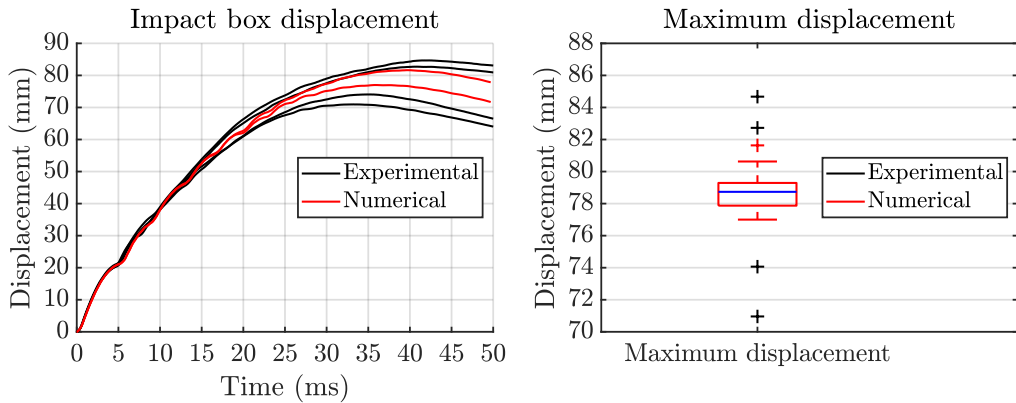


**Figure 8.2:** The simulations with highest and lowest maximum displacement from the 50 simulations with different initial damage distribution.

Compared to the four experimental results.

**Figure 8.3:** Box plot of the maximum displacement from the 50 simulations with different initial damage distribution.

Compared to the four experimental results.

Seen from Figure 8.1a, the initial phase of the force curve is independent of initial damage. The explanation is, despite elements having different initial damage, none or almost none elements are yet eroded. Work hardening occurs equally in all simulations independent of accumulated damage. When substantial fracture first occurs the simulations start to deviate. This because the consequence of different initial damage distribution is due to which, and in which order, the elements are eroded. This implies either a higher or lower crushing force compared to the

average. Seen from Figure 8.1a  $\pm 1$  standard deviation is about 25 kN for the late displacements. This is considered a substantial difference compared to the average force. It is therefore believed that probabilistic failure modeling is of interest when modeling the impact of a rim. However, when studying the mean force in Figure 8.1b practically no difference is seen. This indicates that the initial damage changes *at which* displacement peak loads occur but since peaks only occur for a very short time all simulations are on average the same.

Among the 50 simulations, two simulations yield the largest and lowest response in terms of maximum displacement respectively. In Figure 8.2 the time history for the impact box is shown in these cases. Note that the displacements are well within the range of what is seen experimentally. A difference between simulations and experiments is when displacement curves start to deviate, 25 ms compared to 15 ms. This indicates that even though the numerical model captures some of the late stochastic behavior in rim deformation, the physical differences in the early phase of deformation is not captured.

The difference in maximum displacement between the 50 simulations are shown in Figure 8.3. A box plot generated from the numerical results is compared to experiments.

A question of interest is what causes the difference between the 50 simulations? The visual deformations have been investigated. The rim deforms close to identically in all cases: the only difference being which elements get eroded and the order of erosion. Figure 8.4 shows which elements are eroded from the simulations which have the largest and smallest maximum displacement. Though the displacement between the two cases differs by 4.6 mm, it is hard to see any noticeable difference in the deformation sequence. Both follow the same deformation pattern and identifying the mechanism leading to a difference in stiffness and displacement is difficult to see.

It is believed that the numerical approach to model fracture is essential for the result. Another fracture criterion e.g., extended Cockcroft-Latham, could give another result. However, seen from physical experiments, material fracture occurs differently for different rims due to the probabilistic material properties.

Although the probabilistic approach is able to capture variance in the rim response, it does not contribute to changing the buckling mode. From Chapter 7, the significant difference between simulations and experiments concerning crushing force was found to be buckling dominated. Thus, the statistical analysis presented in this section would be of more quantitative interest if buckling was captured correctly.

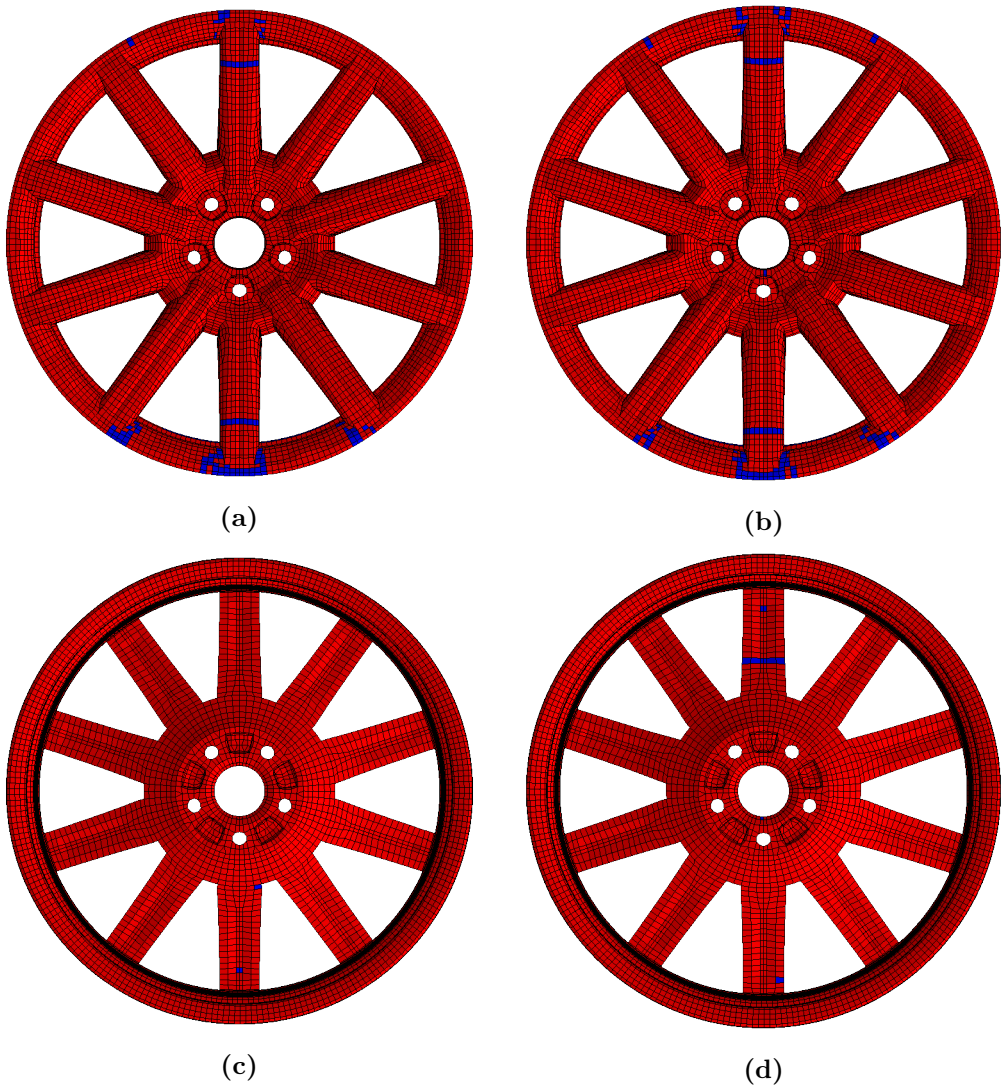


**Figure 8.4:** Blue elements indicate failure and are eroded.  
Direction of impact from bottom on the short spoke.  
(a), (c) represents the simulations with the lowest maximum displacement.  
(b), (d) represents the simulations with the largest maximum displacement.

### 8.3 Initial Damage

From Section 8.2 it was found that different initial damage distributions only affect the late deformation response. Further, for practical purposes, it does not affect the mean crushing force. To assess the added value of including initial damage, two additional simulations were carried out and compared to the base model. The first with an average initial damage,  $W_0 = 3.73$ , for all elements. The second with no initial damage,  $W_0 = 0$ , for all elements. The results are presented in Figure 8.5. Both mean force, maximum displacement and the general trend is the same for all simulations. This indicates that the initial damage distribution does not add significant value to the numerical model.

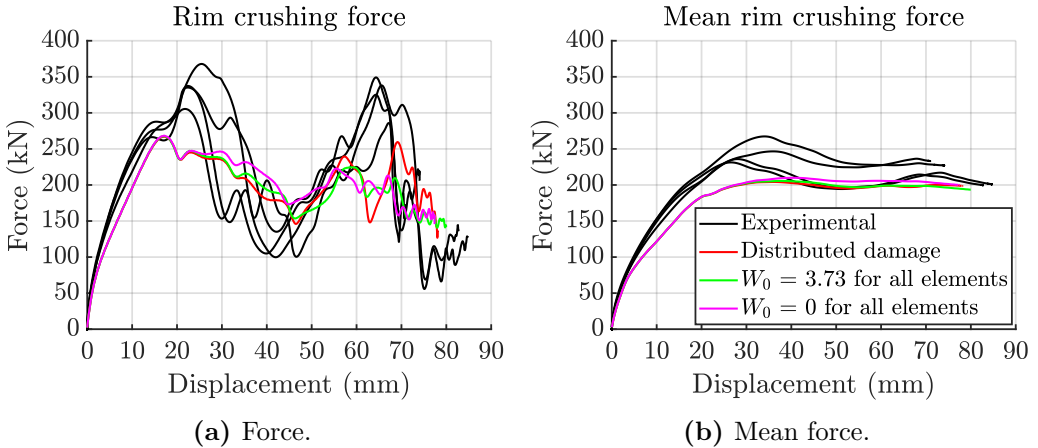
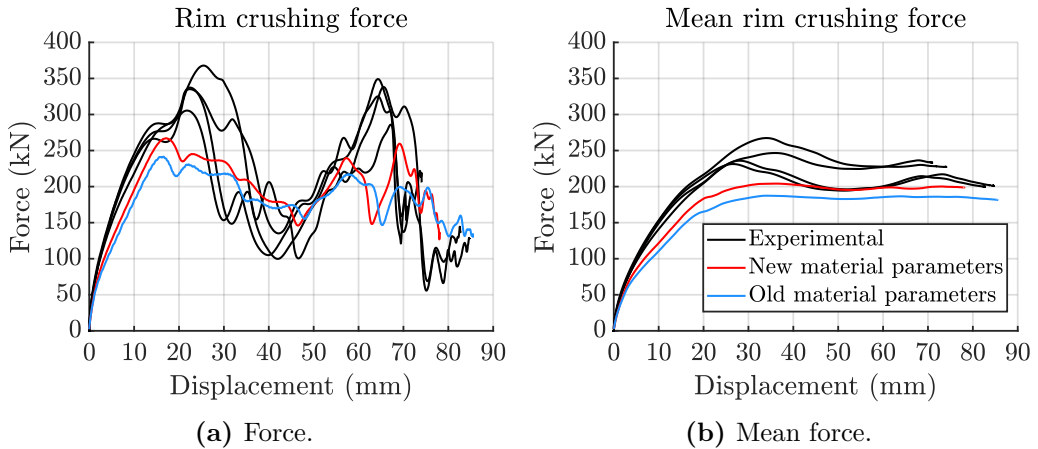


Figure 8.5: Effect of initial damage formulation.

### 8.4 Material Parameters

In Chapter 3.3 the new material tests carried out is described. In brief, the material parameters for the rim bed were found to be in accordance with what Kittilsen and Swanberg found. For the spokes, the new tests suggest slightly different parameters. The strain rate sensitivity was also quantified. To assess the influence of the different material parameters, simulations have been performed.

In Table 3.1 the the old material parameters are listed. In Table 3.5 the new parameters are listed. The differences being that yielding is increased from 181.3 MPa to 200 MPa for the spokes and the strain rate dependency constant is



**Figure 8.6:** Effect of new vs. old material parameters.

included and set to  $C = 0.00718$ . Hardening parameters are kept the same. The rim bed parameters are not changed.

Simulations taking the new and the old material parameters are shown in Figure 8.6. From the figure, the effect of adjusting the material parameters is clearly seen. The stiffness and the mean force are increased. This is a closer estimation of the physical behavior. However, compared to experimental results, the differences between the old and the new parameters are not that significant. Both the first and second peaks are underestimated. The minimum value between the two peaks is overestimated.

Based on these simulations, it is clear that material parameters are important. Adjusting it so that it corresponds to this year's material tests yields a better comparison to experimental results. It is therefore considered an essential piece in the puzzle of developing a more representative numerical model.

## 8.5 Remeshing

All previously presented simulations in the thesis, as well as all rim studies presented by Kittilsen and Swanberg, and Martinsen, have taken the orphan mesh of the rim provided by Audi. This mesh is found to be quite coarse. Especially the spokes which are meshed with three elements in the thickness direction at the outer part are considered too coarse. Bending occurs in the spokes and FE rule of thumb says at least five elements should be used in such cases. Thus, a mesh

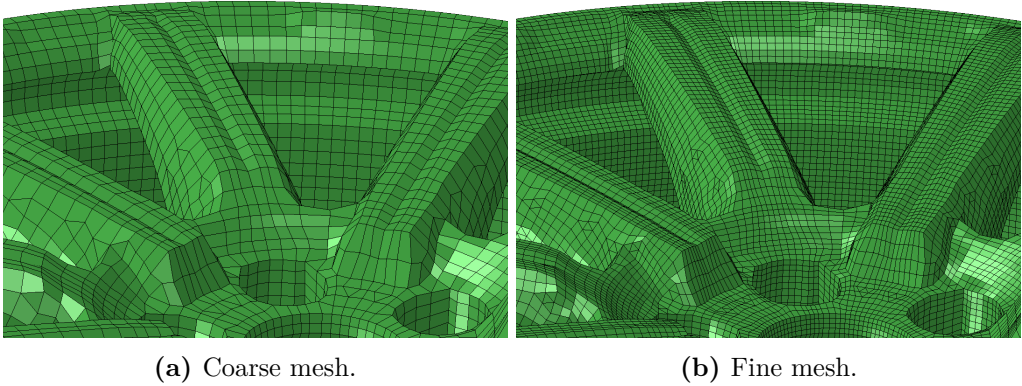


**Figure 8.7:** Close-up of coarse and fine mesh.

refinement of the rim has been done. Generally, all brick elements have been split in eight and all shell elements in four. A close-up of the old coarse mesh and the new fine mesh is shown in Figure 8.7.

Refining the mesh was hoped to increase the accuracy of the buckling response. However, as is the general case, a fine mesh resulted in a softer behavior. Thus, a lower force level was experienced as can be seen in Figure 8.8. It should be mentioned that the fracture parameter  $W_c$  is mesh sensitive, and by using the same value as for the coarse mesh the fracture behavior might not be correct. However, the initial part of the force vs. displacement curve is not dependent on fracture and the initial response can justify the conclusion of softer behavior. The initial peak load is reduced by about 35 kN.

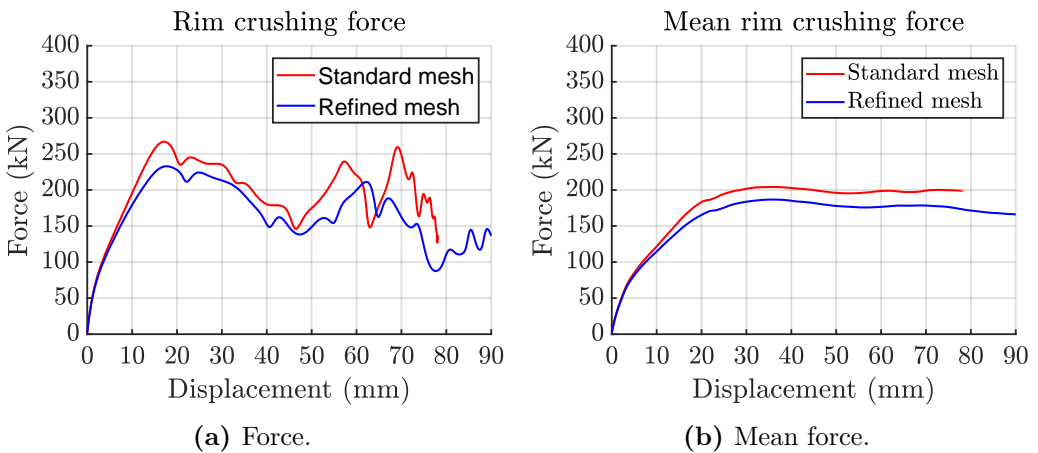
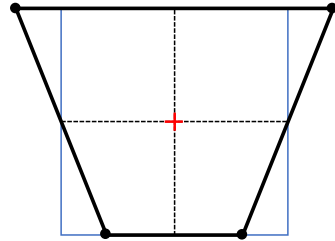


**Figure 8.8:** Comparison of response between refined and standard mesh model.

## 8.6 Fully Integrated Elements

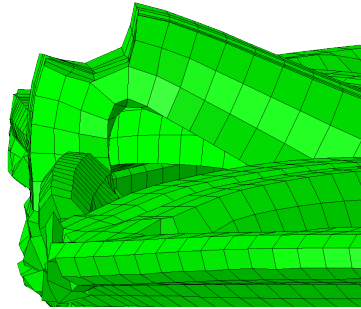
Reduced integrated elements with one integration points, such as the S4R and C3D8R elements used in the rim, are susceptible to hourglassing or zero-energy modes.

Figure 8.9 shows how a quadrilateral element subjected to bending will experience zero strain and stress at the integration point. Introducing stiffness to the element using artificial strain energy is the normal remedy. However, as was seen in Section 5.3 the artificial strain energy in the simulation amounted to 10% of the internal energy which is above the recommended limits.



**Figure 8.9:** Hourglass mode.

To alleviate the artificial strain energy, fully integrated elements can be used. As the spoke elements are eroded, the last remaining element row is subjected mainly to bending, which is seen in Figure 8.10. As a consequence, the elements do not experience much strain in the integration point, and the damage is not accumulated. Using fully integrated elements was therefore thought to help with complete fracture of the spokes, which was seen experimentally.



**Figure 8.10:** Elements subjected to bending.

Unfortunately, using fully integrated elements with element erosion was not possible with the sub-routines used. Whereas the standard behavior in Abaqus is to erode elements when all integration points have accumulated damage equal to one, the sub-routines used eroded elements as soon as one integration point reached the limit. This resulted in a rim behavior which is far too brittle.

The effects of using fully integrated elements can, however, be seen in simulations without failure included. Figures 8.11 and 8.12 show how the artificial strain energy is reduced from about 6% of the internal energy to 2% going from reduced integration to full integration.

It is also seen that the mean force increases slightly and that the maximum displacement decreases when using fully integrated elements.

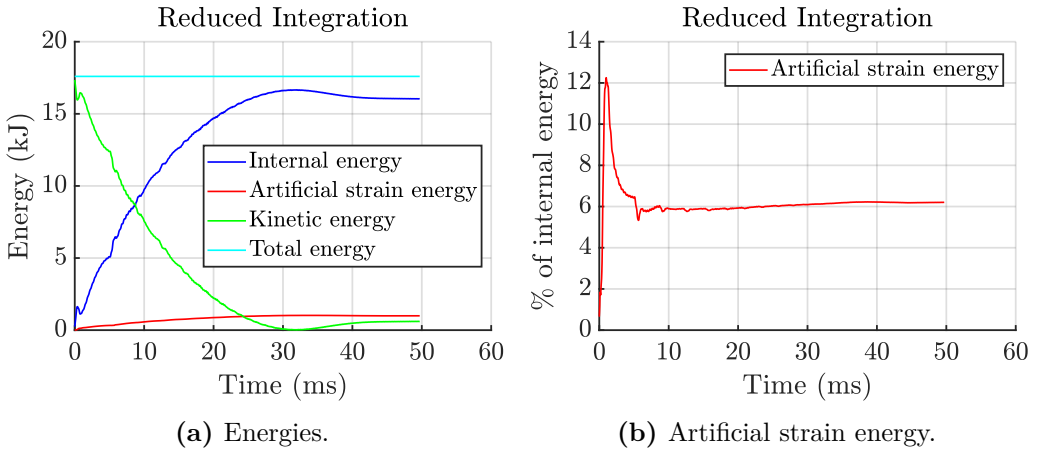


**Figure 8.11:** Energies in the simulation using reduced integration.

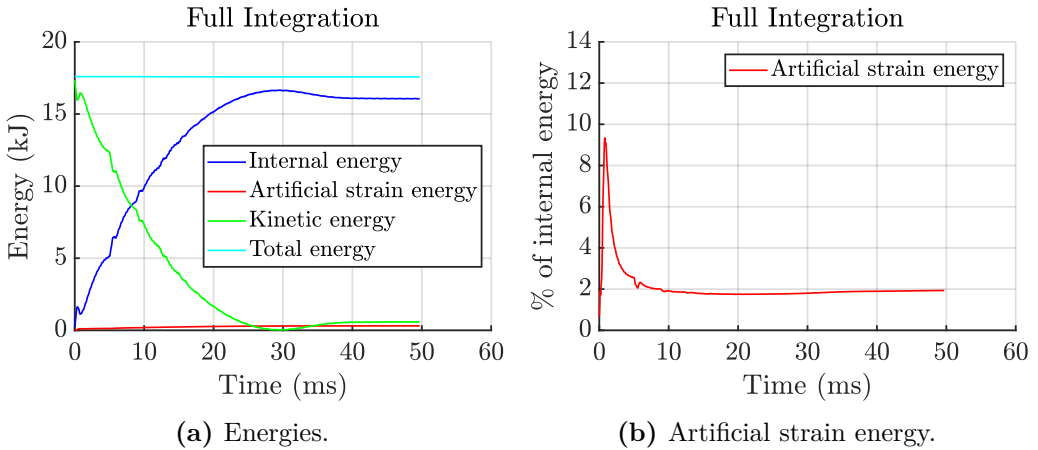


**Figure 8.12:** Energies in the simulation using full integration.

## 8.7 Excluding Fracture

As fracture occurs in the simulations, resistance from the rim is reduced and the force level drops. By excluding fracture in the model, an upper limit of the crushing force can be found.

Figure 8.13 shows the response of the rim when fracture is neglected in the numerical simulations. What is worth noting is that the peak force is similar to the simulations which were run with fracture included, meaning the peak force is independent of fracture. Though the presence of damage and fracture has an impact on the deformation pattern, it is not an essential factor for determining peak loads. As the peak loads remain the same for this upper bound case, it suggests that there is something else and fundamentally different between the real world case and the way the rim is modeled. Some stiffness and resistance in the rim are lost before elements are eroded.

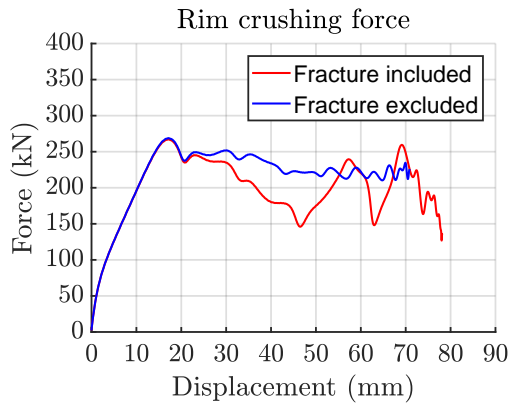


**Figure 8.13:** Comparison between model with and without fracture included.

## Chapter 9

# Discussion

### 9.1 Material Characterization

Quasi-static material tests from one of the provided rims have been carried out for this thesis and compared to the tests carried out by Kittilsen and Swanberg. The new tests strongly indicate the challenge of characterizing the cast aluminum. Stochastic behavior is introduced due to the manufacturing process, and a deterministic characterization fails to capture the range of behavior. Previous tests were used to describe the variation in fracture strain, and incorporated in the numerical model by initial damage. Representative parameters characterized yield stress and hardening. Hardening is considered to be well described using previously found parameters. However, the yield stress is found to have stochastic tendencies and variations in yield are found to affect the numerical response of the rim. A similar distribution of initial yield stress, as the initial damage, could improve the numerical capability of stochastic investigation.

A new contribution to previous studies is the material tests carried out to determine strain rate dependency for the cast aluminum. The specimens tested were all taken from the spoke section of the rim. These tests indicated a relatively strong strain rate dependency of the cast aluminum. An elastic-viscoplastic material model is therefore found suitable for numerical modeling. Simulations suggest that material parameters accounting for viscous effects should be included to match experimental behavior.

## 9.2 Quality of the Experimental Test Concept

Martinsen completed his work with the design of the test rig used for experiments carried out for this thesis. Through testing of aluminum crash boxes and the provided rims, the crash rig is found to be a valid method for experimental testing. The technique developed to estimate the crushing force is also proven to work. However, some discoveries are made which degrade the quality of the test concept. Translations are obtained by the use of high-speed cameras recording from one side of the test only. The underlying assumption is that the impact box translates in-plane only without rotation. Close investigation on the installed test rig showed deviations from a perfectly symmetric setup. Tests indicated that for low-velocity free impacts, the impact box is found to get a small rotation. Although this rotation is considered negligible in component tests, it is problematic to quantify this effect. A test setup using one camera on each side could be useful to study the three-dimensional kinematic behavior of the impact box.

The test setup requires four high-speed cameras. This was found to be cumbersome due to a limited view of the test setup. The cameras were prioritized so that the camera recording the translation of the impact box had a clear view. This was done because the acceleration of the box is essential to arrive at a reasonable estimation for the crushing force. The consequence of this was a less ideal position for the camera recording the trolley. The results showed a noisy signal for the translation of the trolley. In the end, this was found to be less of a problem because the inertia of the nose and load cell contributes significantly less than the inertia of the impact box when estimating the crushing force. However, to trace the velocity, obtained by differentiating the translation, and study the kinematics of the trolley throughout the test, a less noisy signal would be desirable.

To improve the quality of measurements from experiments alternative measurement methods should be considered. Translations could be captured using lasers. For instance, a laser mounted on the reaction wall would give the relative distance between the impact box and the reaction wall directly. This would exclude the high-speed camera recording translation of the top support, used to correct translations of the trolley and impact box in the current setup. A laser would also make it easier to do preliminary work related to setup and post-processing of test results. At the same time, the signal would be less noisy.

Another limitation of the test rig is the stiffeners between the top and bottom support blocking the view of the nose impacting the impact box. It is found that more energy is dissipated in experiments than in simulations through contact damping. A possible camera recording in this area could lead to a deeper understating of the repeated impacts.

Accelerations are computed from the second derivative of translations. From an experimental point of view, this was expected to be challenging because noise and error tend to amplify when differentiated. To better capture accelerations, it should be considered to use accelerometers instead of cameras. Accelerometers are well-known equipment and available in a variety of models. Thus, to ensure a higher quality of test results better and more suitable measuring equipment should be used.

### 9.3 Failure Criterion

From the investigation of the experimental and numerical deformation sequence, a distinct difference in fracture behavior has been discovered. Fracture of the spokes appears to be shear dominated for the physical rims. This is a problematic observation regarding the choice of failure criterion for numerical analyses. Cockcroft-Latham is used for the numerical study. This is a tension based ductile failure criterion. Thus, the stress state culminating in the shear fracture in the physical experiments does not accumulate the correct damage in the numerical model. Elements are therefore not eroded correctly to numerically replicate what is seen experimentally.

The choice of failure criterion is believed to be important to match experimental and numerical results better. A proposed criterion is the extended Cockcroft-Latham, to better capture shear fracture. Though, due to difficulties in implementation, this was not assessed in the numerical study for this thesis.

A challenge with using a more complex failure criterion is the need for additional material tests. First of all, this would be time-consuming. Specimens would have to be cut and machined from the rim before tested. Second of all, the cast aluminum is by nature stochastic. Thus, by introducing additional material parameters scatter in all of these would have to be considered. To find a set of failure parameters, described by probability distributions, would require many tests. Also, how to implement these material variations would have to be figured out. However, to better model the fracture seen in experiments, it might be inevitable to use a different failure criterion.

## 9.4 Numerical Formulation

The provided mesh from Audi consists of shell elements for the rim bed while the spoke section consists of solid brick elements. A drawback of this modeling approach is the coupling between the shell and solid elements. The shell elements share nodes with some of the solid elements such that displacements are transferred and shared between the two. However, the rotational degrees of freedom from the shells are not transferred to the solid elements, and as a consequence, the rotational stiffness is lost. This could help explain why the numerical model experiences more rotation in the spokes during the initial contact than what is seen experimentally. Subsequently, the loss of stiffness might explain the underestimation of peak load in the numerical simulations.

This is an interesting observation, and work has been initiated looking into this by modeling the rim bed using solid elements. The ongoing work has shown promising results with an increase in peak loads and overall stiffer behavior.

The shell to solid coupling might explain some loss in stiffness, but other numerical formulations might also have an effect on the estimated crushing force. While a smaller element size yields a softer response with greater displacement, the fracture behavior seems to be more accurately captured. Artificial strain energy in the model amounted to about 10% of the internal energy which is considered to be significant. When modeling the rim using fully integrated elements this was significantly reduced and the forces were seen to increase slightly as an added effect. In addition, though it was not tested, it is believed that using a fully integrated model, including failure, would increase the accuracy of the fracture behavior with a more rapid fracture propagation. For elements experiencing hourglassing under bending the strain would be sampled at several integration points which could lead to more damage accumulation than for the reduced integrated elements.

It is clear from the numerical simulations and parametric study that the numerical formulation is important for the rim behavior in the simulations. Some parameters may lead to higher crushing force and reduced deformation, while others have the opposite effect. It is therefore clear that to increase the accuracy of the numerical model, it is important to find the correct combination of numerical parameters. It is believed that the correct numerical formulation would lead to a better replication of the force vs. displacement curve, with higher peak forces and a more rapid drop towards the minimum force as a result of more accurate fracture behavior.

## 9.5 Filters

Due to the nature of the test setup, several filtering processes were needed to obtain reasonable results and estimation of the crushing force. The filters presented in this thesis were found through trial and error. Based on the numerical and experimental validation of the test setup, it is fair to say the filters that are used work quite well. However, there is no guarantee that the optimal filter is applied.

More work could have gone into the design of filters used, which could be tailored to this experiment. When using frequency domain filters a good way to find a suitable filter is to extract the frequency content from the sensor data using Fourier transforms. This would allow for greater insight into the frequencies that would need to be filtered out. Though better filters could be made, it is not given that any real value would be added as the current filters have yielded acceptable results.



## Chapter 10

# Conclusion and Further Work

### 10.1 Conclusion

Based on the experimental tests carried out for this thesis, it is concluded that the test rig developed is applicable for impact testing of cast aluminum rims. The setup allows essential measurements to be made without producing too much noise. Translations measured using high-speed cameras and DIC gave satisfying results. Accelerations computed from the differentiation of translations are found to be suitable to estimate the crushing force. The method for estimating the crushing force in experiments is also proven to work. Results from both experimental and numerical work support this conclusion.

From the numerical study, simulations are found to reproduce the experiments to some extent. It is concluded that the numerical model is able to capture trends satisfyingly. Trends for both spoke and rim bed fracture are in accordance with experiments. The mean force at maximum displacement is captured as well as overall kinematics. However, the numerical model is not able to reproduce peak loads and details in the force vs. displacement relation. Thus, the numerical model *cannot* be concluded to reproduce the experiments to a full extent.

The investigation from running simulations with different initial damage is found to be a valid method to investigate some of the stochastic behavior of the rim numerically. Modeling scattered behavior by assigning elements with different initial damage is concluded to affect the response of the rim after fracture of the short spoke.

## 10.2 Further Work

### Quasi-Static Reference

As the test setup is quite elaborate and the force estimation is complex, experiments should be conducted to get a quasi-static reference for the response of the rim in order to eliminate uncertainties due to dynamical testing. For the quasi-static reference, inertial effects can be ignored, and the crushing force can be more accurately captured using a conventional test technique. This would provide additional data to verify the crushing forces which were estimated experimentally.

### Fracture Modeling

More work should be done in order to introduce a more suitable failure criterion for the current load case. The Cockcroft-Latham criterion, which is used in this thesis, is a ductile failure criterion based on tensile loading. From the experimental tests, it seems more reasonable to use a failure criterion which better suits shear fracture like the Extended Cockcroft-Latham criterion or a failure criterion which exhibits brittle behavior.

### Numerical Formulation

Numerical formulations are found to affect the response of the rim in simulations. A parametric study should be carried out to find a better numerical representation of the rim. This includes modeling of the rim bed using solid elements to circumvent the loss of rotational stiffness due to the shell-to-solid coupling of the rim bed and spokes. Sub-routines in order to use full integration in combination with failure should be fixed. Work can be done with a refined mesh model and the appropriate failure parameter,  $W_C$ , to better capture the correct fracture behavior.

# Bibliography

- [1] IIHS.org: About the Institutes. URL: <https://www.iihs.org/iihs/about-us>. Accessed: 24.01.2019
- [2] IIHS.org: Frontal Crash tests. URL: <https://www.iihs.org/iihs/ratings/ratings-info/frontal-crash-tests>. Accessed: 24.01.2019
- [3] IIHS.org: Ratings - 2017 Audi Q7. URL: <https://www.iihs.org/iihs/ratings/vehicle/v/audi/q7-4-door-suv/2017>. Accessed: 24.01.2019
- [4] IIHS.org: Small Overlap Crash Test Protocol. URL: [https://www.iihs.org/media/ec54a7ea-1a1d-4fb2-8fc3-b2e018db2082/Ztykhw/Ratings/Protocols/current/small\\_overlap\\_test\\_protocol.pdf](https://www.iihs.org/media/ec54a7ea-1a1d-4fb2-8fc3-b2e018db2082/Ztykhw/Ratings/Protocols/current/small_overlap_test_protocol.pdf). Accessed: 24.01.2019
- [5] Kittilsen, E. T. and Swanberg, E.: *Behaviour and modelling of cast aluminium rims subjected to impact loading*. Master thesis, NTNU (2017)
- [6] Martinsen, C.: *Modelling and testing of thick aluminium castings under impact loadings*. Master thesis, NTNU (2018)
- [7] Groover, M. P.: *Fundamentals of Modern Manufacturing: Materials, Processes, and Systems*. John Wiley & Sons, Inc., 4th. edition edn. (2010)
- [8] Knoll, O.: *A Probabilistic Approach in Failure Modelling of Aluminium High Pressure Die-Castings*. Ph.D. thesis, NTNU and Karlsruhe Institute of Technology (2015)
- [9] Zhang, B., Cockcroft, S. L., Maijer, D. M., Zhu, J. D., and Phillion, A. B.: Casting Defects in Low-Pressure Die-Cast Aluminum Alloy Wheels. *JOM* 57; 36-43 (2005)

- [10] Magazin, K. E.: Low-Pressure vs High-Pressure Die-Casting. URL: <https://www.ke-mag.com/issue-42/article/low-pressure-vs-high-pressure-die-casting.html>. Accessed: 14.02.2019
- [11] ModBargains: HRE Flow Form Wheels. URL: <http://www.modbargains.com/hre-ff15-flow-form-wheel-bmw-liquid-silver.htm>. Accessed: 18.02.2019
- [12] Nagarajan, H. N., Kotrappa, H., Mallanna, C., and Venkatesh, V. C.: Mechanics of Flow Forming. *CIRP Annals* 30(1); 159-162 (1981)
- [13] thefabricator: Metal spinning versus flow forming. URL: <https://www.thefabricator.com/article/stamping/metal-spinning-versus-flow-forming>. Accessed: 19.02.2019
- [14] Callister, W. D. and Rethwisch, D. G.: *Materials science and engineering: an introduction*. John Wiley & Sons, Inc., 9th. edition edn. (2014)
- [15] Pio, L. Y.: Effect of T6 Heat Treatment on the Mechanical Properties of Gravity Die Cast A356 Aluminium Alloy. *Journal of Applied Science* 11(11); 2048-2052 (2011)
- [16] Hopperstad, O. S. and Børvik, T.: NTNU Materials Mechanics TKT4135, Lecture Notes: Materials Mechanics Part I (2017)
- [17] Hopperstad, O. S. and Børvik, T.: NTNU Impact Mechanics TKT4128, Lecture Notes - Part 1: Modelling of plasticity and failure with explicit finite element methods (2018)
- [18] Lee, C. D.: Effects of microporosity on tensile properties of A356 aluminum alloy. *Materials Science and Engineering* 462(1-2); 249-254 (2007)
- [19] Anderson, T. L.: *Fracture Mechanics: Fundamentals and Applications*. CRC Press LLC, 2nd edn. (1995)
- [20] Gatea, S., Ou, H., Lu, B., and McCartney, G.: Modelling of ductile fracture in single point incremental forming using a modified GTN model. *Engineering Fracture Mechanics* 186 (2017)
- [21] Smith, S. W.: *The Scientist and Engineer's Guide to Digital Signal Processing*. California Technical Publishing, 2nd edn. (1999)

- [22] Press, W. H., Teukolsky, S. A., Vetterling, W. T., and Flannery, B. P.: *Numerical Recipes in C: The Art of Scientific Computing*. Press Syndicate of the University of Cambridge, 2nd edn. (2002)
- [23] wikipedia.org: Savitzky–Golay filter. URL: [https://en.wikipedia.org/wiki/Savitzky-Golay\\_filter](https://en.wikipedia.org/wiki/Savitzky-Golay_filter). Accessed: 26.02.2019
- [24] Balchen, J. G., Andersen, T., and Foss, B. A.: *Reguleringsteknikk*. Institutt for teknisk kybernetikk, NTNU, 6th edn. (2016)
- [25] wikipedia.org: Digital Filter. URL: [https://en.wikipedia.org/wiki/Digital\\_filter](https://en.wikipedia.org/wiki/Digital_filter). Accessed: 1.03.2019
- [26] Hopperstad, O. S.: NTNU Impact Mechanics TKT4128, Lecture Notes: Explicit finite element methods (2018). URL: [https://ntnu.blackboard.com/webapps/blackboard/execute/content/file?cmd=view&content\\_id=\\_460080\\_1&course\\_id=\\_11289\\_1](https://ntnu.blackboard.com/webapps/blackboard/execute/content/file?cmd=view&content_id=_460080_1&course_id=_11289_1). Last visited on 2018/10/31
- [27] Akhil, K. T., Arul, S., and Sellamuthu, R.: The Effect of Section Size on Cooling Rate, Microstructure and Mechanical Properties of A356 Aluminium Alloy in Casting. *Procedia Materials Science* 5; 362-368 (2014)
- [28] Kleine, A., Rosefort, M., Matthies, C., and Koch, H.: Improved Properties of Aluminum Cast Alloys Due to a Boron Grain Refinement. URL: [https://www.trimet.eu/en/fe-veroeffentlichungen/trimet\\_improved\\_properties\\_of\\_aluminium.pdf](https://www.trimet.eu/en/fe-veroeffentlichungen/trimet_improved_properties_of_aluminium.pdf). Accessed: 20.02.2019
- [29] Chen, Y., Clausen, A. H., Hopperstad, O. S., and Langseth, M.: Stress–strain behaviour of aluminium alloys at a wide range of strain rates. *International Journal of Solids and Structures* 46(21); 3825-3835 (2009)
- [30] Langseth, M. and Hansen, A. G.: NTNU Impact Mechanics TKT4128, Lecture Notes: Crashworthiness of aluminium structures (2018)
- [31] Hanssen, A. G., Auestad, T., Tryland, T., and Langseth, M.: The kicking machine: A device for impact testing of structural components. *International Journal of Crashworthiness* 8(4); 385-392 (2003)
- [32] Langseth, M. and Hopperstad, O. S.: Static and dynamic axial crushing of square thin-walled aluminium extrusions. *International Journal of Impact Engineering* 18; 7-8, 949–968 (1996)

- [33] Grimsmo, E. L., Clausen, A. H., Langseth, M., and Aalberg, A.: An experimental study of static and dynamic behaviour of bolted end-plate joints of steel. *International Journal of Impact Engineering* 85; 132-145 (2015)
- [34] Langseth, M., Clausen, A. H., and Børvik, T.: NTNU Impact Mechanics TKT4128, Lecture Notes: Impact and Energy Absorption (2017)
- [35] Costas, M., Morin, D., Hopperstad, O. S., Børvik, T., and Langseth, M.: A through-thickness damage regularisation scheme for shell elements subjected to severe bending and membrane deformations. *Journal of the Mechanics and Physics of Solids* 123; 190-206 (2019)

# Appendices



## Appendix A

# Strain Rate Sensitivity

Test	$\sigma_{eq} (p = 1\%)$ (MPa)	$\dot{p}$ (1/s)	$\sigma_{eq} (p = 2\%)$ (MPa)	$\dot{p}$ (1/s)	$\sigma_{eq} (p = 3\%)$ (MPa)	$\dot{p}$ (1/s)
S1i1L	227.8	5e-04	241.9	5e-04	253.1	5e-04
S1i1R	225.3	5e-04	239.8	5e-04	249.8	5e-04
S1i2L	240.3	5e-04	254.0	5e-04	263.6	5e-04
S1i2R	-	-	-	-	-	-
S2i1	-	-	-	-	-	-
S2i2	252.9	219.1	264.0	257.4	276.6	268.8
S3i1L	260.7	344.8	274.6	365.3	285.9	393.9
S3i1R	258.8	785.1	272.7	844.5	284.7	894.2
S3i2L	268.9	850.6	274.1	869.9	286.5	932.0
S3i2R	259.2	724.9	273.3	815.6	283.1	897.9

Test	$\sigma_{eq} (p = 4\%)$ (MPa)	$\dot{p}$ (1/s)	$\sigma_{eq} (p = 5\%)$ (MPa)	$\dot{p}$ (1/s)	$\sigma_{eq} (p = 6\%)$ (MPa)	$\dot{p}$ (1/s)
S1i1L	261.5	5e-04	268.3	5e-04	273.8	5e-04
S1i1R	258.0	5e-04	265.3	5e-04	270.5	5e-04
S1i2L	271.3	5e-04	277.1	5e-04	281.2	5e-04
S1i2R	-	-	-	-	-	-
S2i1	-	-	-	-	-	-
S2i2	284.3	319.7	294.2	326.4	300.8	337.6
S3i1L	297.0	386.3	301.4	378.3	304.1	414.7
S3i1R	288.2	888.5	-	-	-	-
S3i2L	294.7	946.9	299.5	955.0	308.5	945.0
S3i2R	289.7	913.1	298.8	951.6	308.0	960.1

**Table A.1:** True stress for different values of true plastic strain and strain rate.

---

---

## Appendix B

# Filters

### B.1 Convolution Coefficients for Polynomial Fitting of Savitzky-Golay Filters

Polynomial Degree	quadratic or cubic 2 or 3			quartic or quintic 4 or 5	
Window size	5	7	9	7	9
-4			-21		15
-3		-2	14	5	-55
-2	-3	3	39	-30	30
-1	12	6	54	75	135
0	17	7	59	131	179
1	12	6	54	75	135
2	-3	3	39	-30	30
3		-2	14	5	-55
4			-21		15
Normalization	35	21	231	231	429

**Table B.1:** Convolution coefficients for polynomial fitting [23].

## B.2 Time Domain Filters

Filter	1	2	3	4
Type	SG	SG	SG	SG
Weights method	None	Kaizer	Gaussian	Gaussian
Convolution length	20	40	35	45
Polynomial order	3	3	3	3
Window size	111	95	101	87

**Table B.2:** Filter parameters  
*SG=Savitzky-Golay*.

## B.3 Frequency Domain Filters

Filter	5	6	7	8	9
Type	Zero phase				
Frequency Response	Low pass				
Impuls Response	FIR	FIR	IIR	FIR	FIR
Sample Rate	2	2	2	2	2
Filter Order			1		
Half Power Frequency			0.022		
Stopband Frequency	0.100	0.200		0.150	0.04
Stopband Attenuation	130	130		200	50
Passband Frequency	0.011	0.011		0.010	0.009
Passband Ripple	1.00	1.00		1.30	0.001
Design method	Equiripple	Equiripple	Butter	Equiripple	Equiripple
Convolution length	20	20	20	20	20

**Table B.3:** Filter parameters.

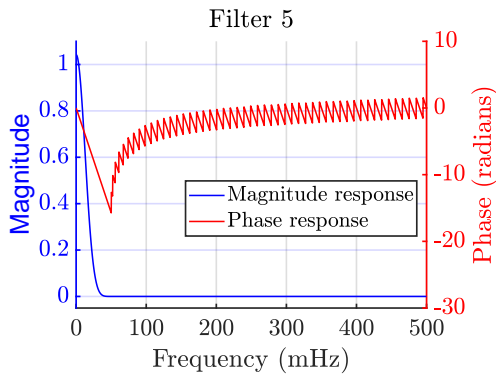


**Figure B.1:** Response of filter 5.

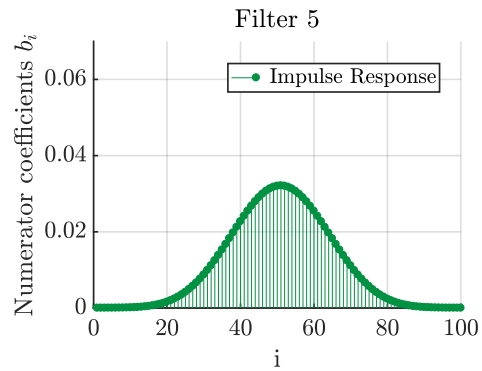


**Figure B.2:** Impulse response of filter 5.

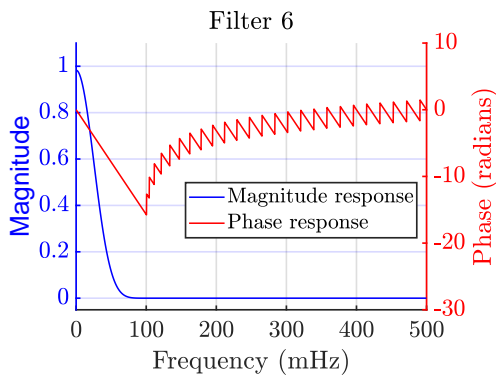


**Figure B.3:** Response of filter 6.

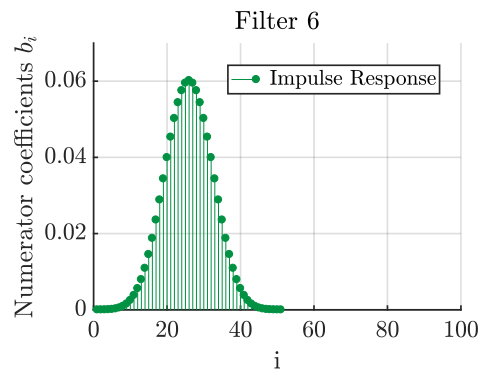


**Figure B.4:** Impulse response of filter 6.

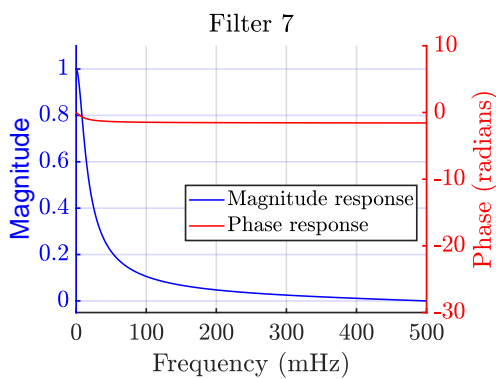


**Figure B.5:** Response of filter 7.

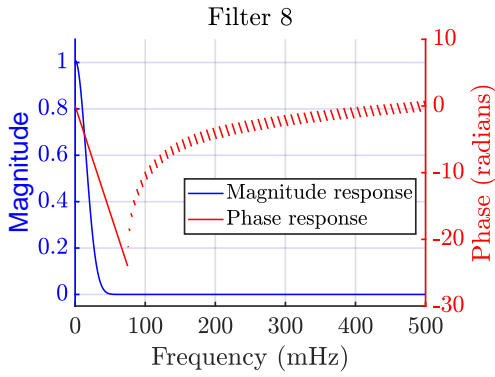


Figure B.6: Response of filter 8.

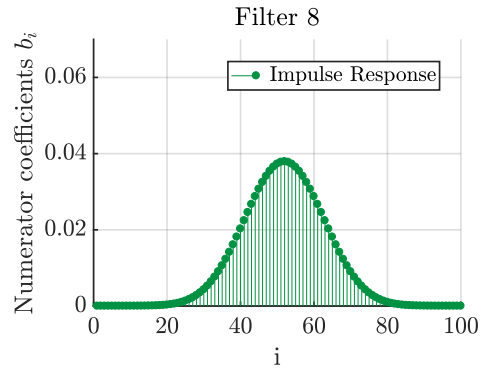


Figure B.7: Impulse response of filter 8.

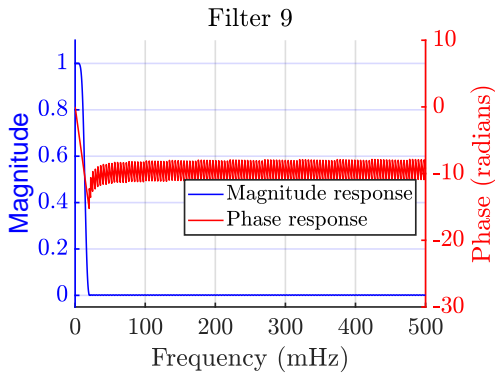


Figure B.8: Response of filter 9.

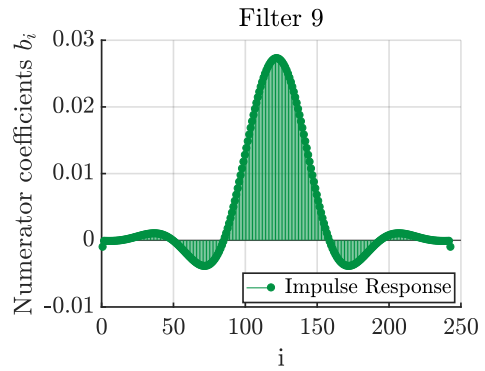
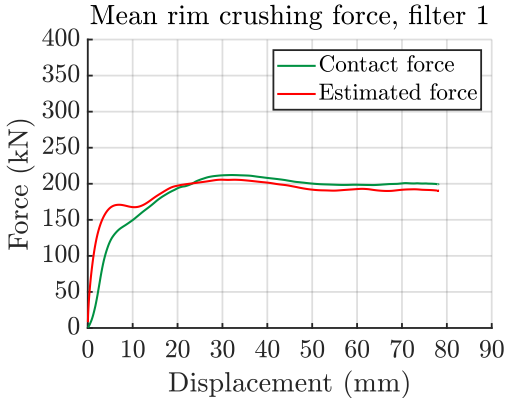
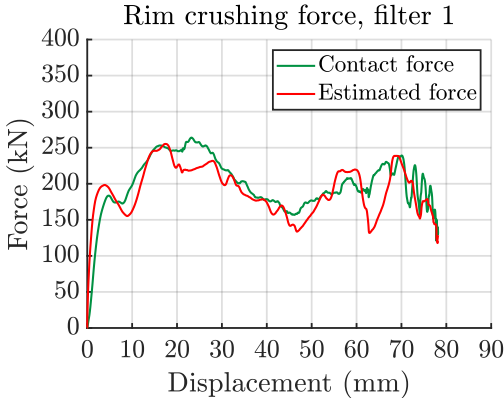
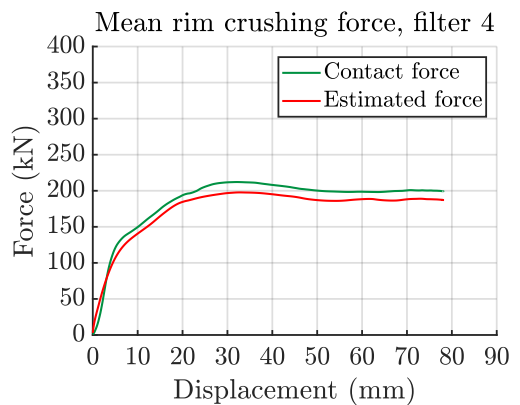
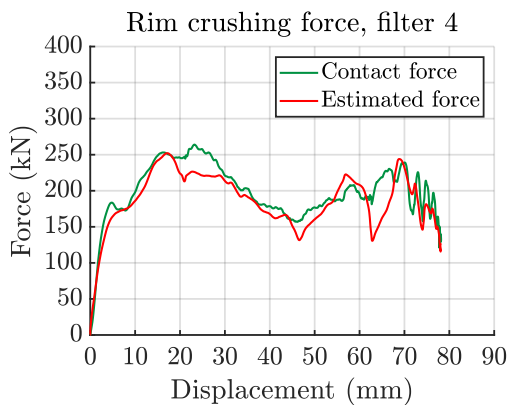
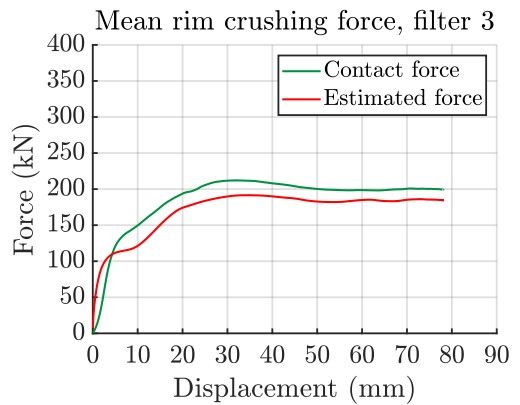
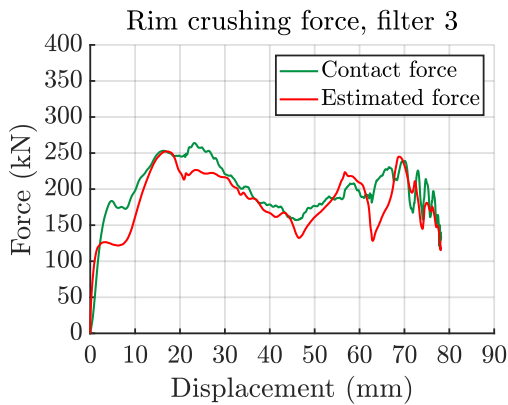
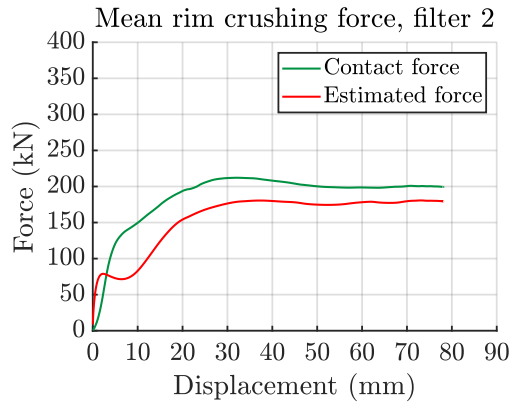
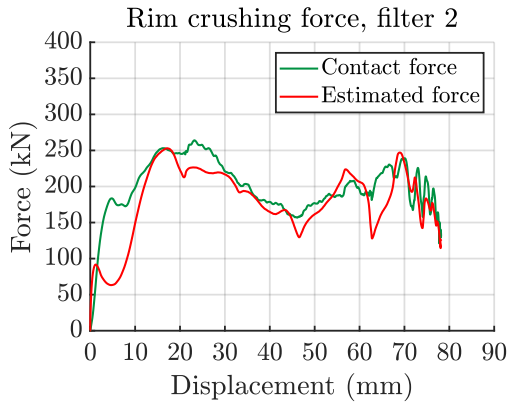


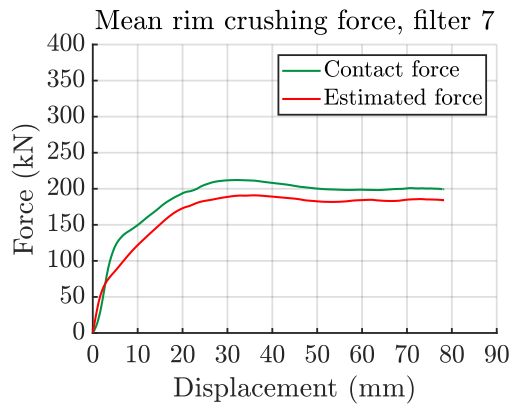
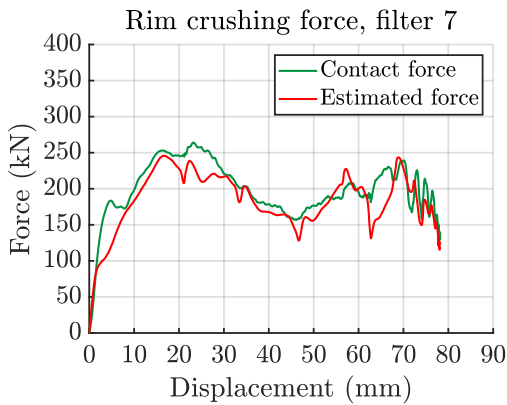
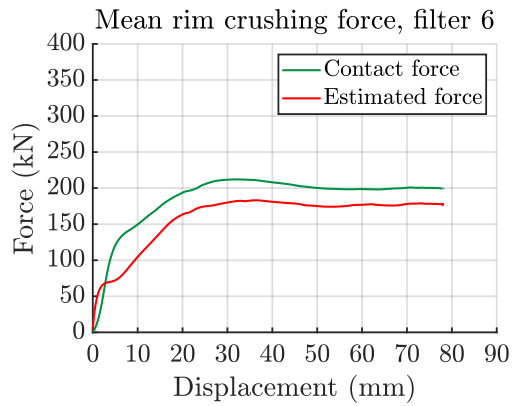
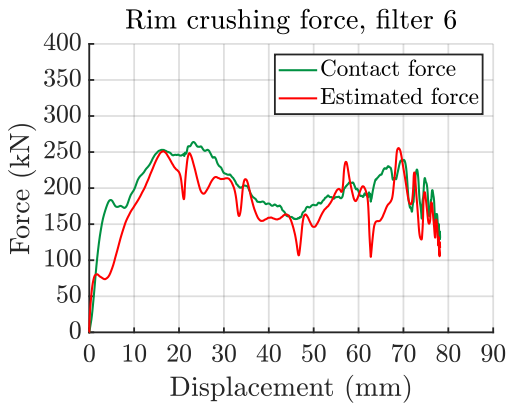
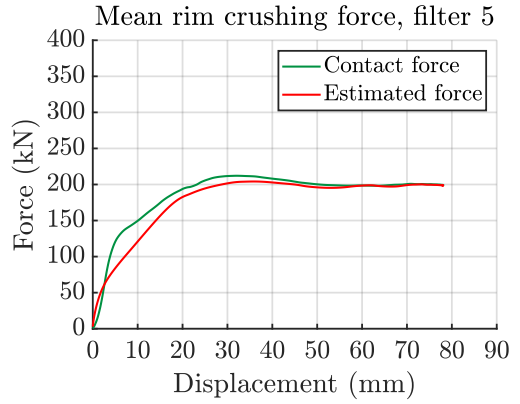
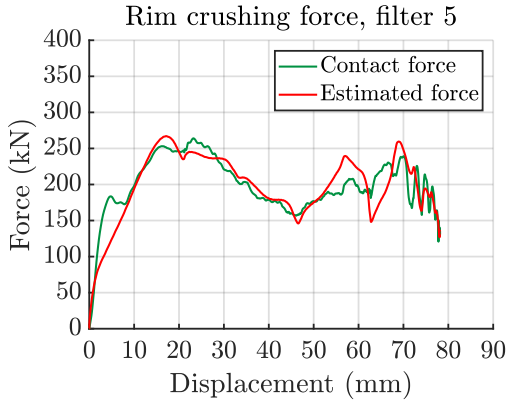
Figure B.9: Impulse response of filter 9.

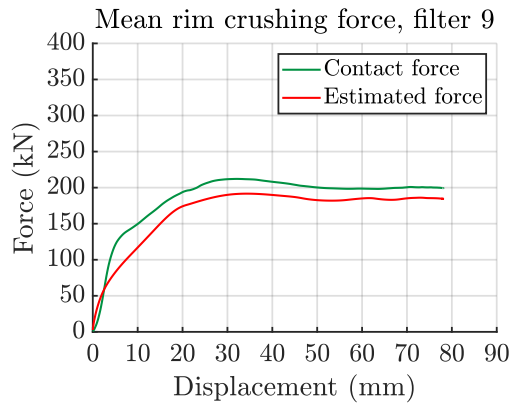
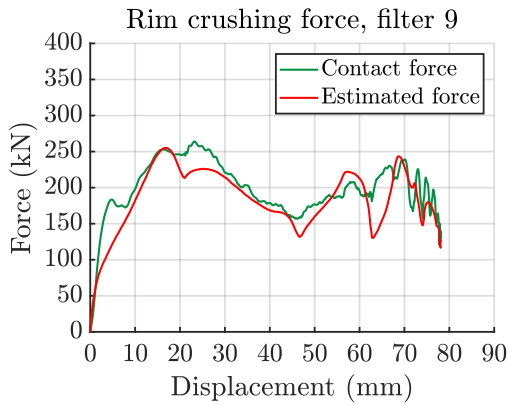
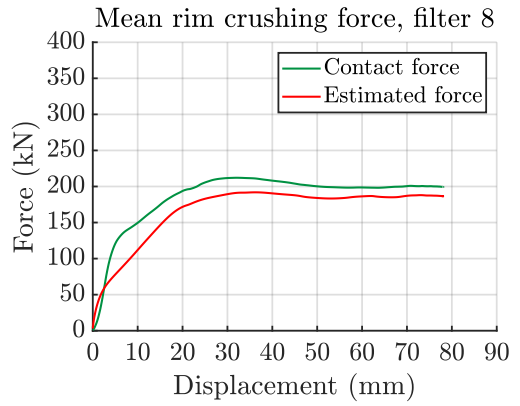
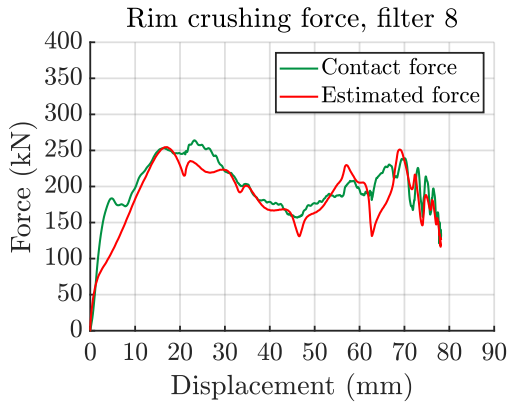
# Appendix C

## Numerical Rim Results Different Filters









## Appendix D

# Material Card of AA6005-T6

```
*Material, name=SMM_AA6005T6_inner
*Include, input = DEPVAR_SMM.inc
*Density
  2.71e-09,
*User material, Constants = 30
**      EFLAG,      YFLAG,      RMAPFLAG,      HFLAG
          1,          3,          5,          1
**      VFLAG,      TFLAG,      DFLAG,      SFFLAG
          0,          0,          4,          0
**      STFLAG,      EO,      NU,      SIGMA0
          0,      77867.71,      0.33,      272.3
          A,      KSI,      THETAOR1,      QOR1
8.00000e+00, 1.00000e-02,      5823.9,      2.2
**      THETAOR2,      QOR2,      THETAOR3,      QOR3
          596.4,      34.22,      281.7,      30.67
          THETAMIN,      DINIT,      DCRIT,      WCB
0.00000e+00, 0.00000e+00,      1.0,      168.67
**      WCS,      WCL,      c,      PHI
          121.124,      44.7038,      0.8599,      1.0
          GAMMA,      THICK,
          1.0,      1.7460
*Material, name=SMM_AA6005T6_outer
*Include, input = DEPVAR_SMM.inc
*Density
  2.71e-09,
*User material, Constants = 30
```

---

```

**      EFLAG,          YFLAG,          RMAPFLAG,          HFLAG
          1,            3,              5,                1
**      VFLAG,          TFLAG,          DFLAG,          SFFLAG
          0,            0,              4,                0
**      STFLAG,          EO,            NU,          SIGMA0
          0,          77867.71,          0.33,          272.3
          A,            KSI,          THETAOR1,          QOR1
8.00000e+00, 1.00000e-02,          5823.9,          2.2
**      THETAOR2,          QOR2,          THETAOR3,          QOR3
          596.4,          34.22,          281.7,          30.67
          THETAMIN,          DINIT,          DCRIT,          WCB
0.00000e+00, 0.00000e+00,          1.0,          168.67
**      WCS,            WCL,            c,            PHI
          121.124,          44.7038,          0.8599,          1.0
          GAMMA,          THICK,
          1.0,          2.5653

```

DEPVAR\_SMM.inc:

\*DEPVAR, DELETE=61

```

61,
1,p, "Equivalent plastic strain"
2,pdot, "Equivalent plastic strain rate"
3,T, "Temperature"
4,Tdot, "Increment in temperature"
5,d, "Damage"
6,pvm, "von Mises norm of plastic strain"
7,LEOTE, "Equivalent strain gradient"
8,OMEGA, "Non local variables"
9,PHI, "Equivalent stress with respect to overstress"
10,SEQ, "Equivalent stress with respect to stress"
11,XEQ, "Equivalent stress with respect to backstress"
12,SY, "Yield stress"
13,R, "Isotropic hardening"
14,Sv, "Viscous stress"
15,we, "Stored elastic energy"
16,wp, "Stored plastic energy"
17,De, "Dissipated elastic energy"
18,Dp, "Dissipated plastic energy"
19,R1, "Isotropic hardening R1"
20,R2, "Isotropic hardening R2"
21,R3, "Isotropic hardening R3"

```

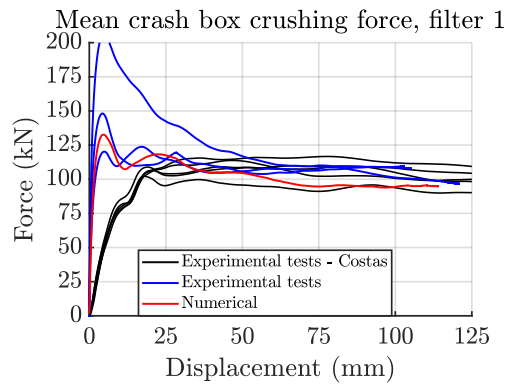
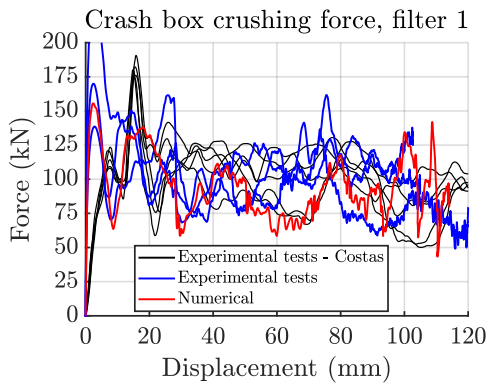
22,R4, "Isotropic hardening R4"  
23,X11, "Kinematic hardening X11"  
24,X12, "Kinematic hardening X12"  
25,X13, "Kinematic hardening X13"  
26,X14, "Kinematic hardening X14"  
27,X15, "Kinematic hardening X15"  
28,X16, "Kinematic hardening X16"  
29,X21, "Kinematic hardening X21"  
30,X22, "Kinematic hardening X22"  
31,X23, "Kinematic hardening X23"  
32,X24, "Kinematic hardening X24"  
33,X25, "Kinematic hardening X25"  
34,X26, "Kinematic hardening X26"  
35,Alpha01, "Kinematic hardening Alpha0 11"  
36,Alpha02, "Kinematic hardening Alpha0 22"  
37,Alpha03, "Kinematic hardening Alpha0 33"  
38,Alpha04, "Kinematic hardening Alpha0 12"  
39,Alpha05, "Kinematic hardening Alpha0 23"  
40,Alpha06, "Kinematic hardening Alpha0 13"  
41,Stress11,"Stress 11"  
42,Stress22,"Stress 22"  
43,Stress33,"Stress 33"  
44,Stress12,"Stress 12"  
45,Stress23,"Stress 23"  
46,Stress31,"Stress 31"  
47,INUM,"Number of iterations for the current time step"  
48,MAXINUM,"Maximum number of iterations"  
49,STRAININC,"Equivalent strain increment"  
50,SIGMA0,"Initial yield stress"  
51,SIGC,"Critical stress"  
52,DTIME,"Time to fracture"  
53,pfd,"Post-Failure Damage"  
54,pc,"Equivalent Plastic strain at failure"  
55,pu,"Equivalent Plastic strain at erosion"  
56,IPRATIO,"Failed integration points"  
57,e33pl,"plastic strain through the thickness"  
58,e33plc,"critical plastic strain through the thickness"  
59,ta,"Ageing time"  
60,PCs,"Strain ageing contribution"  
61,FAIL,"Failure status variable"

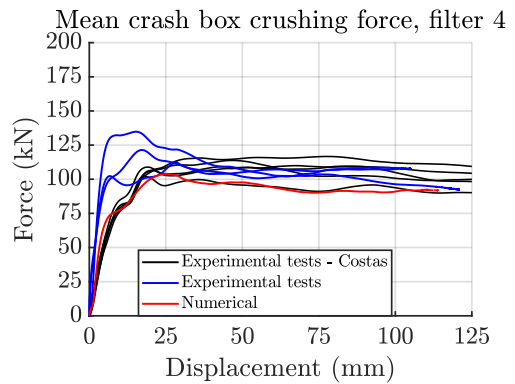
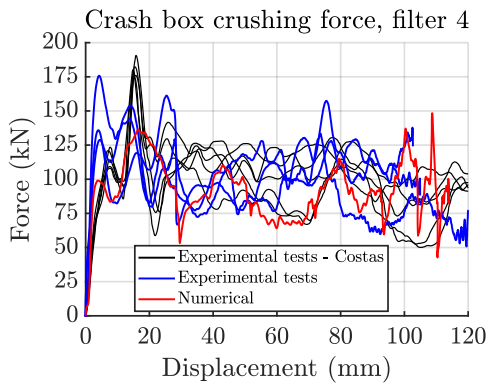
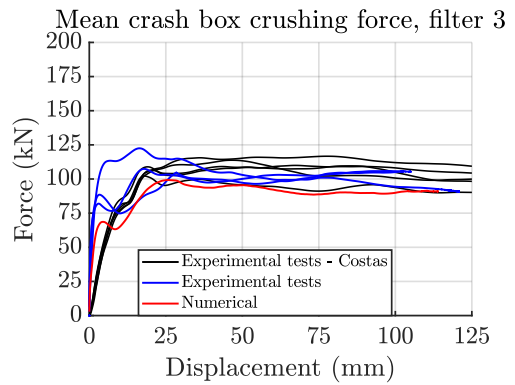
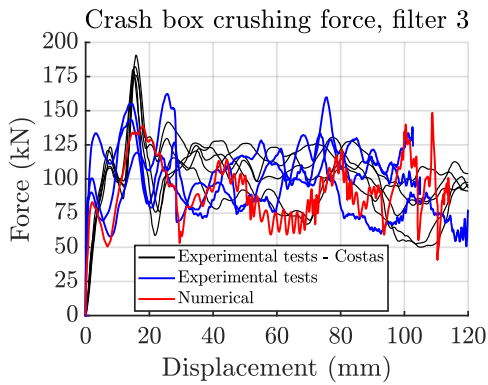
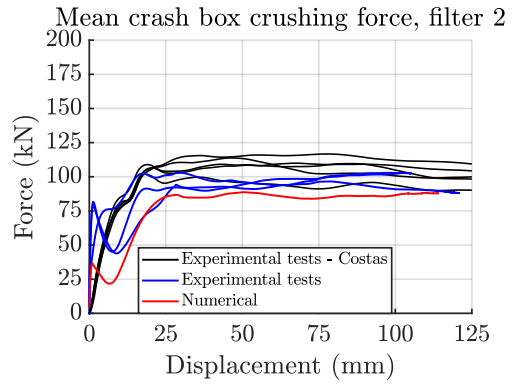
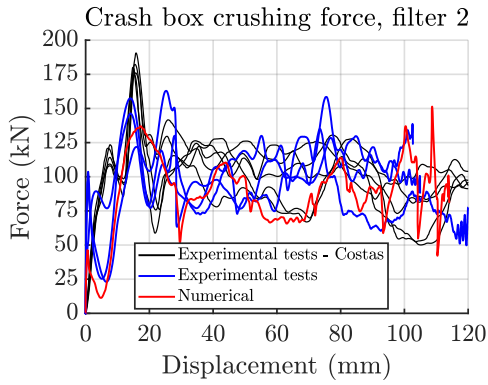
---

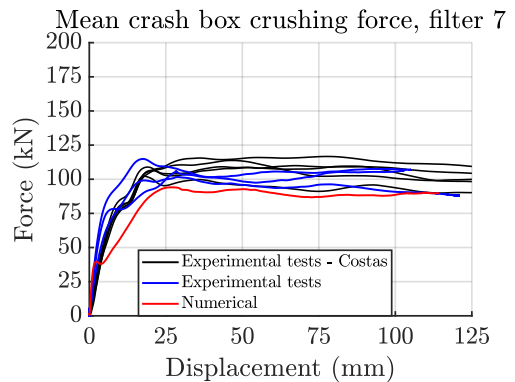
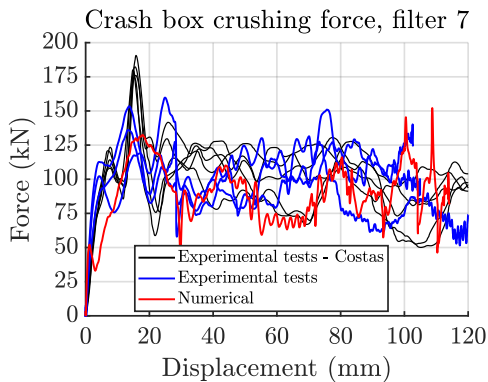
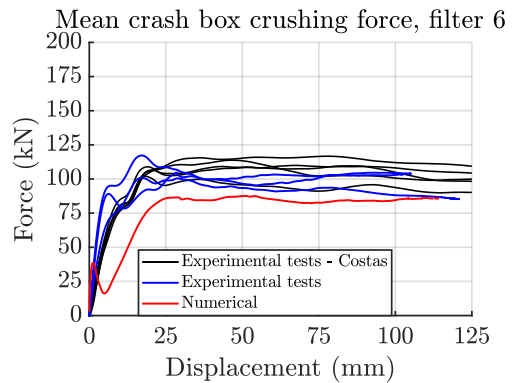
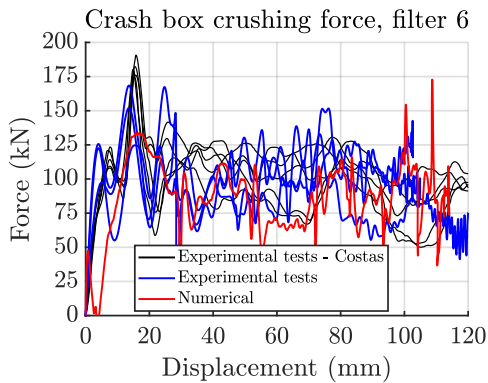
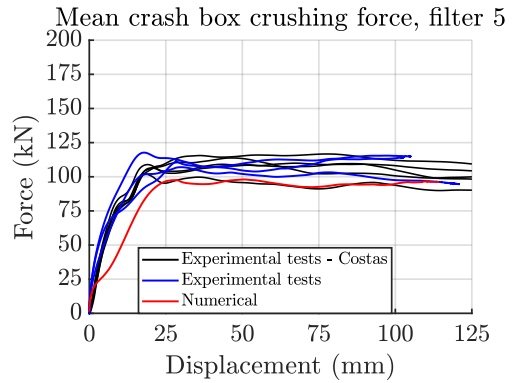
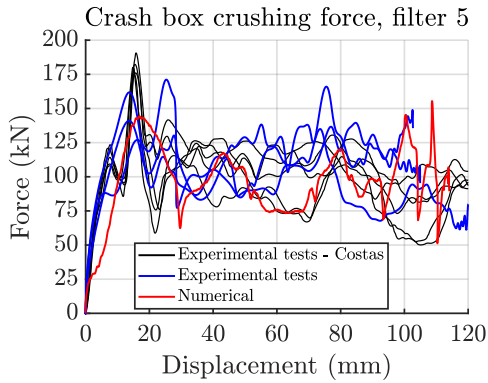
---

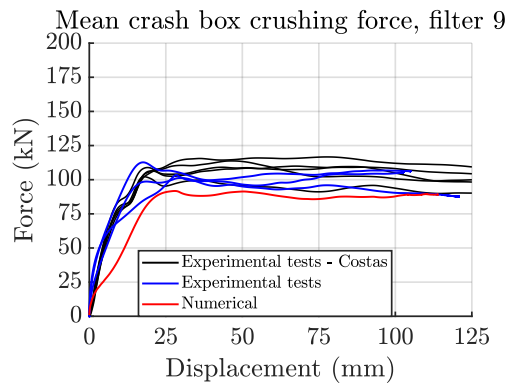
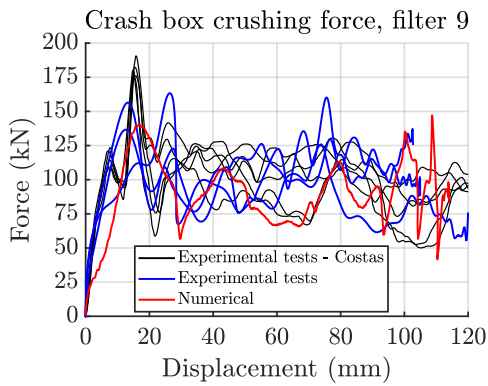
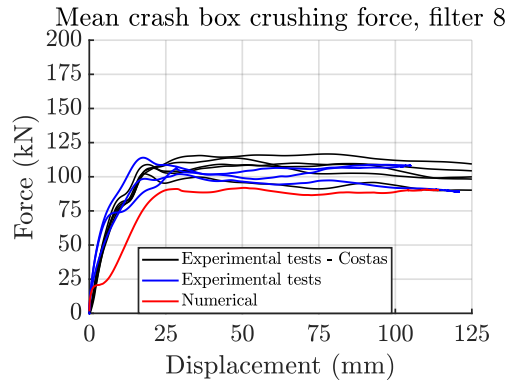
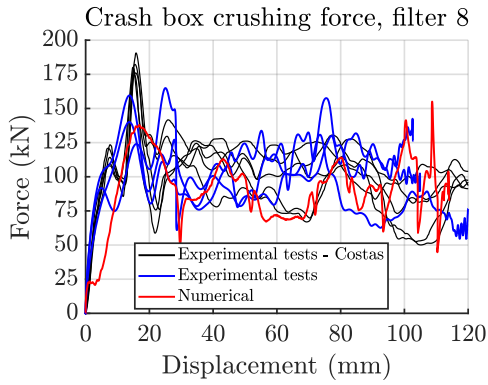
## Appendix E

# Crash Box Results Different Filters



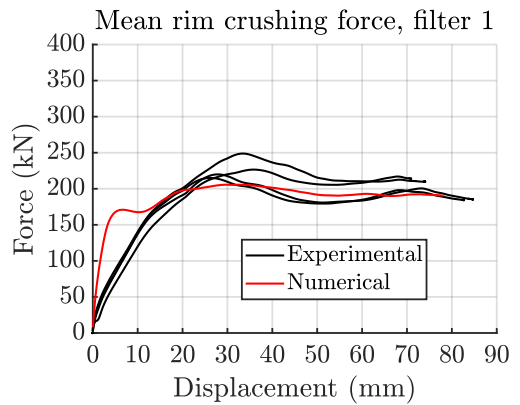
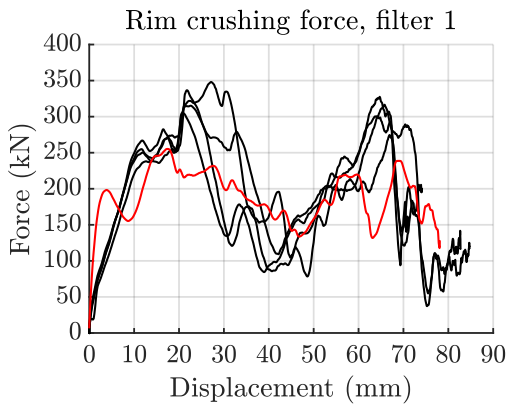


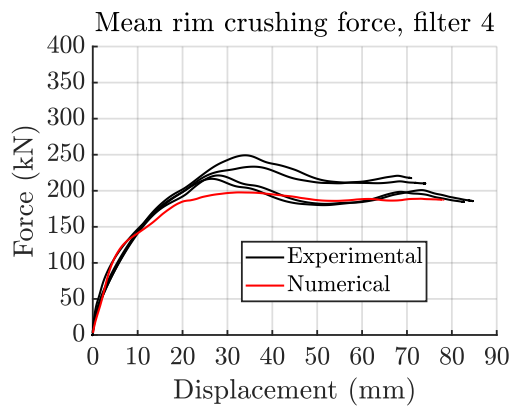
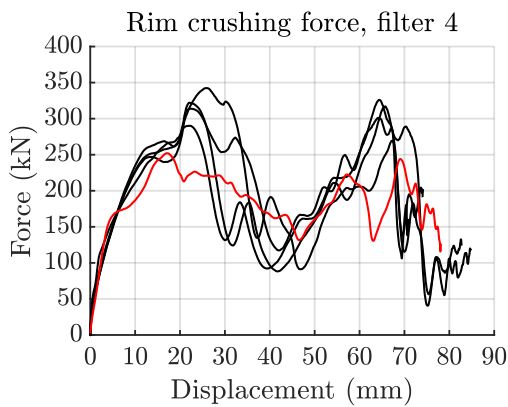
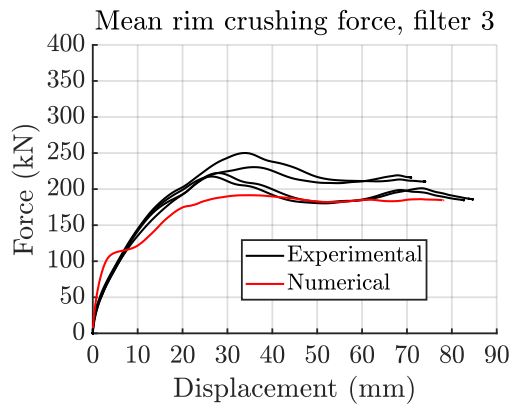
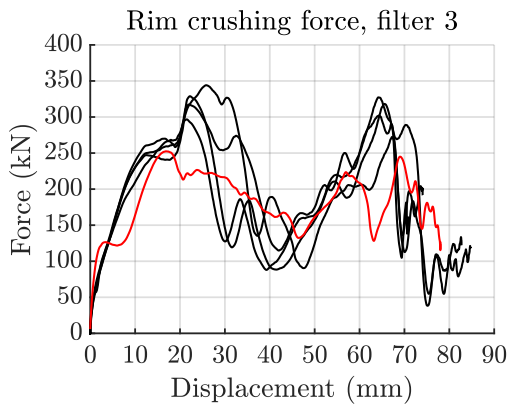
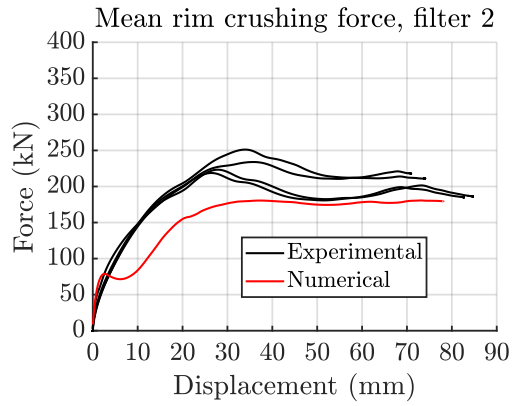
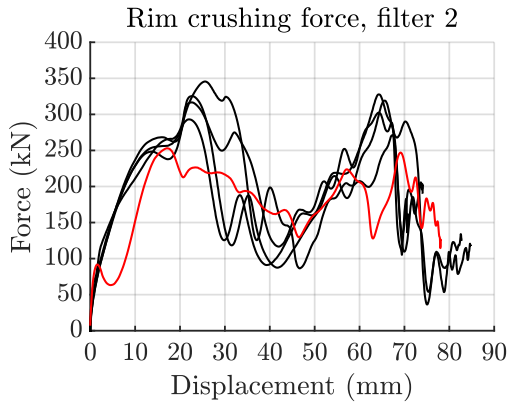


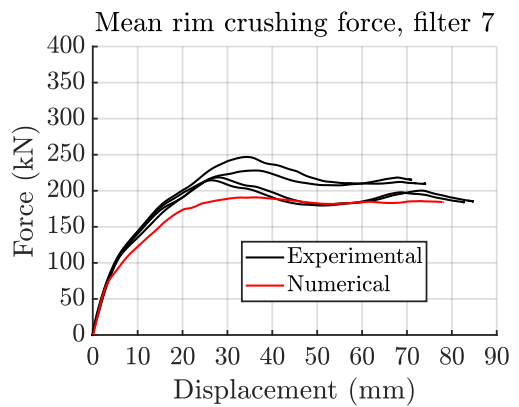
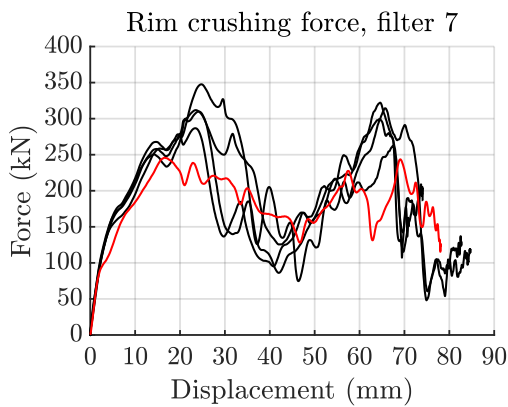
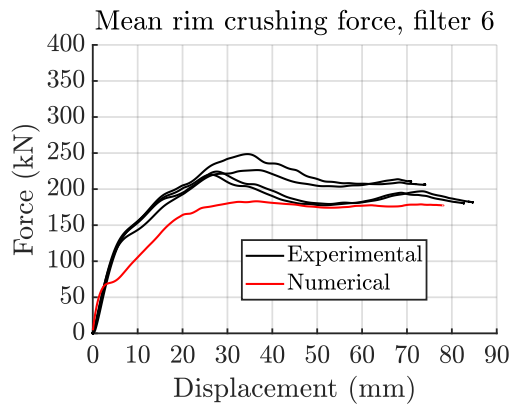
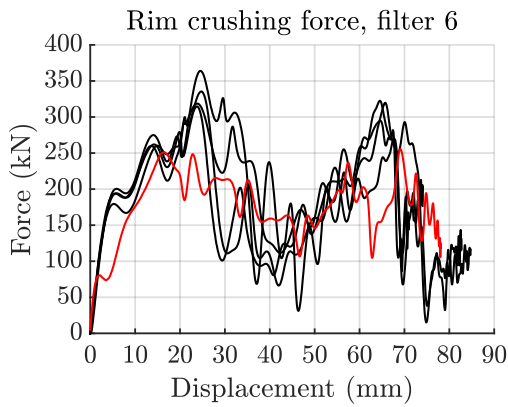
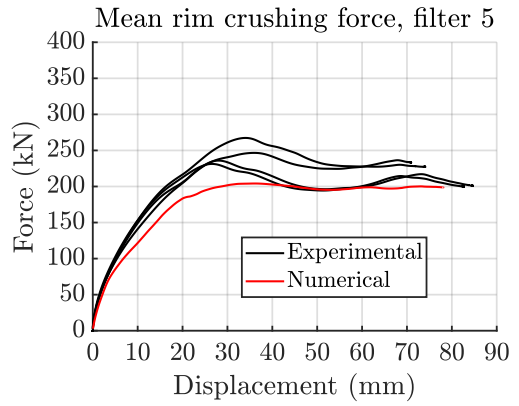
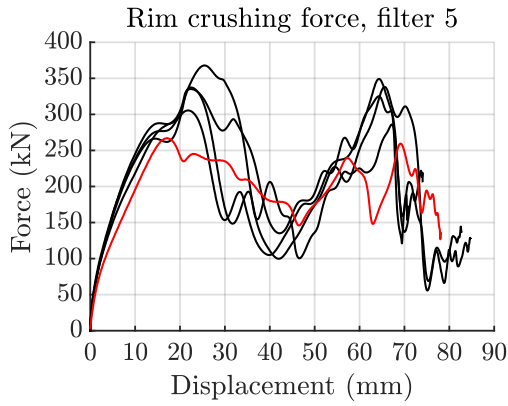


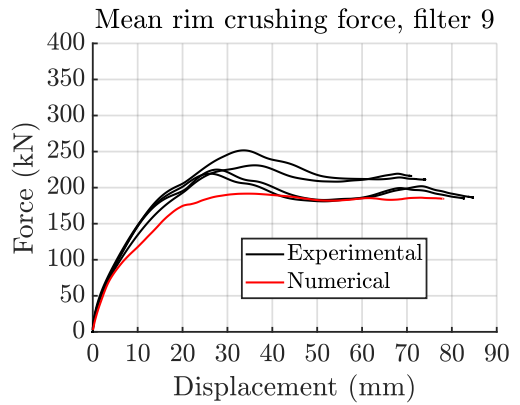
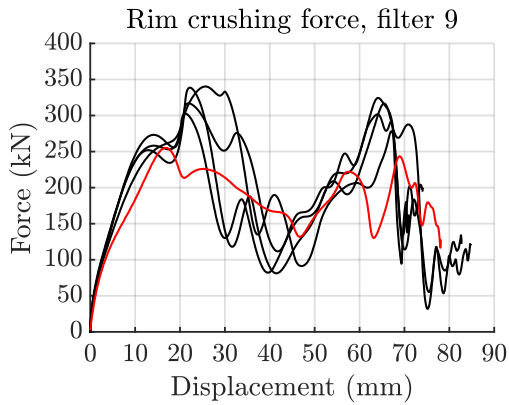
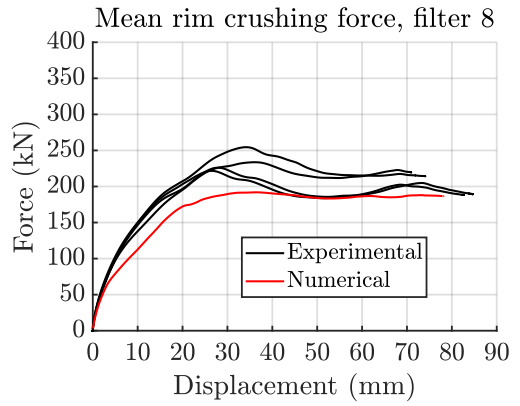
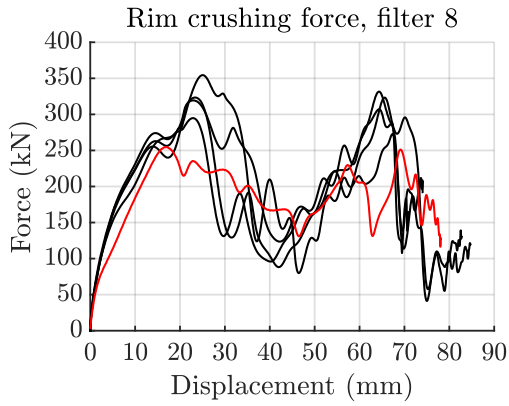
## Appendix F

# Rim Results Different Filters









## Appendix G

# Deformation Sequence

A tip to the reader:

If read as PDF on a computer set the viewer to one side page display without scrolling and read as a flip book.

---

0 mm deformation

Rim 1 – Short spoke configuration



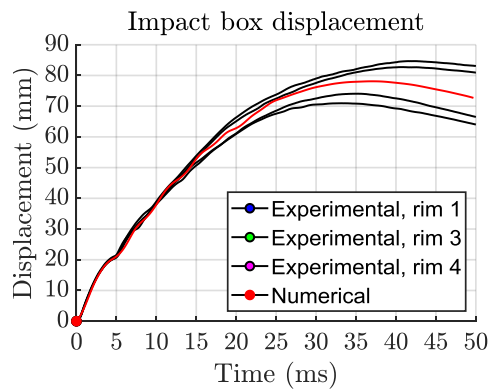
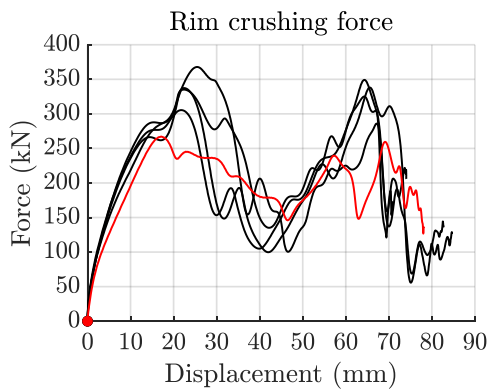
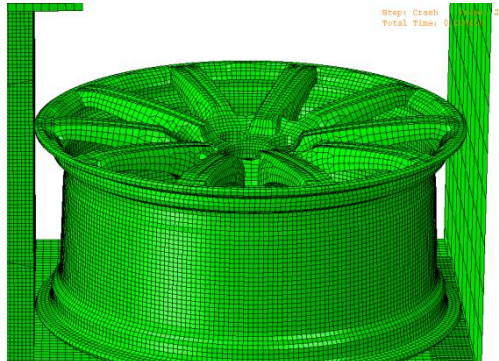
Rim 3 – Short spoke configuration



Rim 4 – Long spoke configuration



Numerical – Short spoke configuration



5 mm deformation

Rim 1 – Short spoke configuration



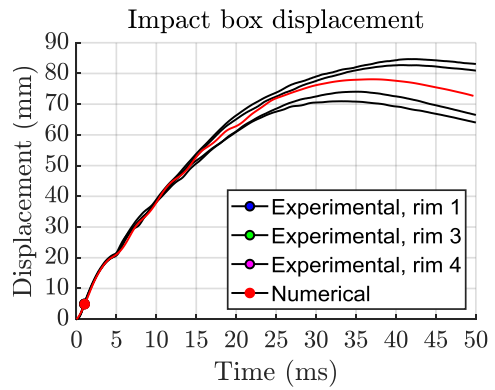
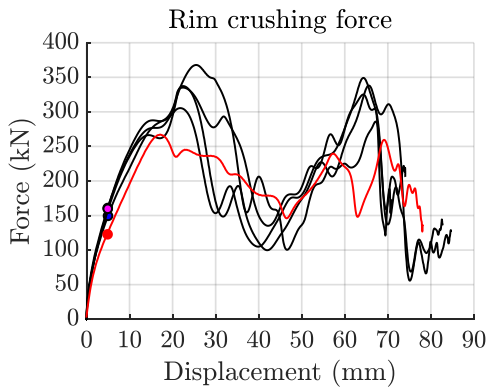
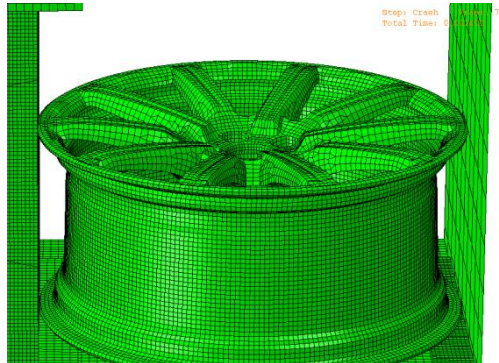
Rim 3 – Short spoke configuration



Rim 4 – Long spoke configuration



Numerical – Short spoke configuration



---

10 mm deformation

Rim 1 – Short spoke configuration



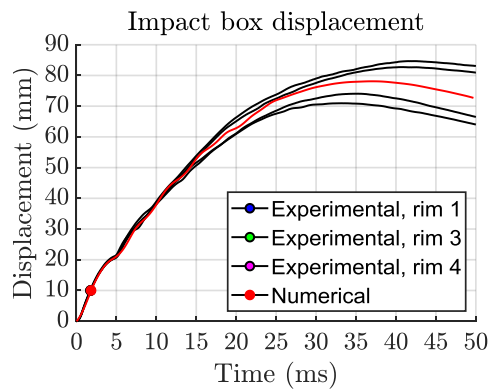
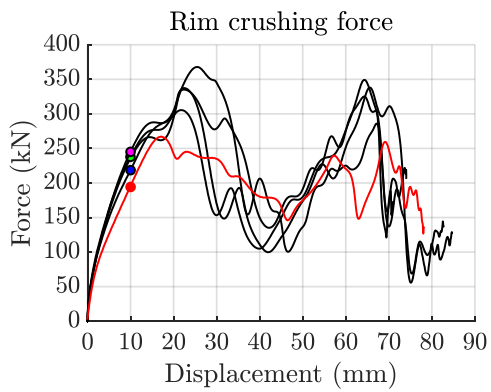
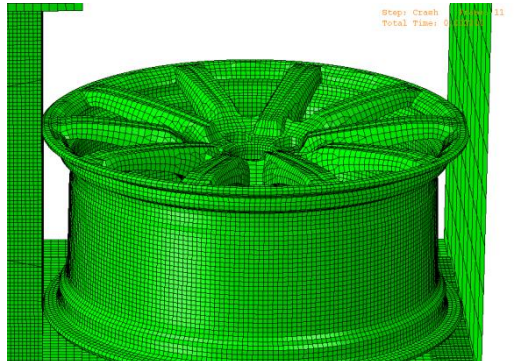
Rim 3 – Short spoke configuration



Rim 4 – Long spoke configuration



Numerical – Short spoke configuration



15 mm deformation

Rim 1 – Short spoke configuration



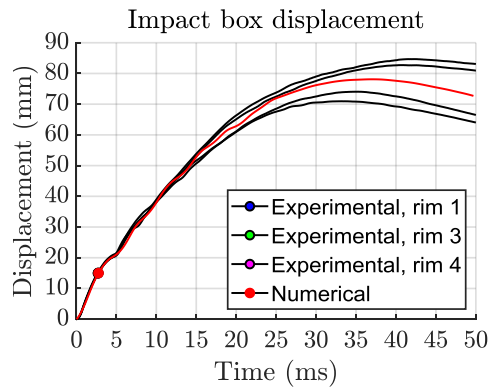
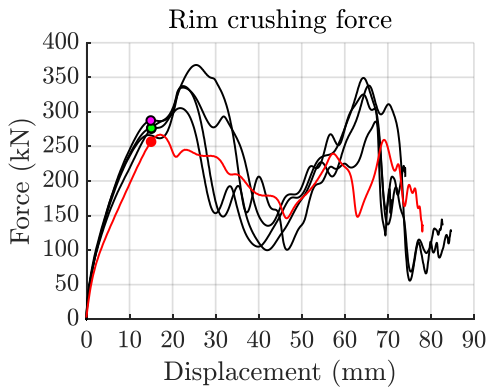
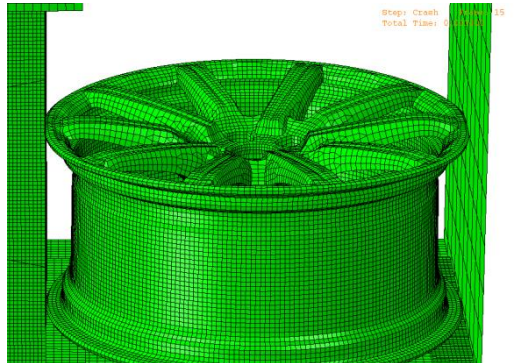
Rim 3 – Short spoke configuration



Rim 4 – Long spoke configuration



Numerical – Short spoke configuration



---

20 mm deformation

Rim 1 – Short spoke configuration



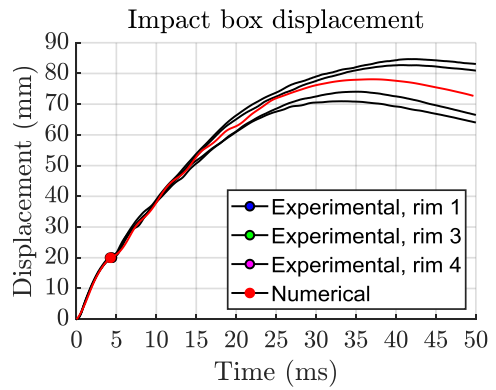
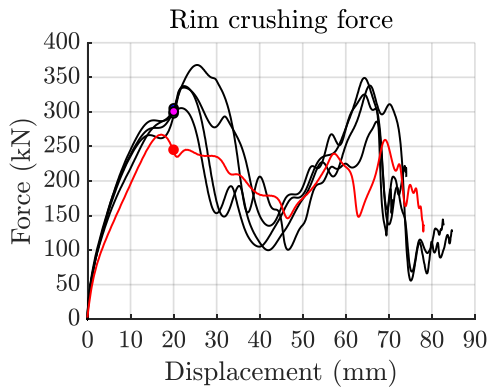
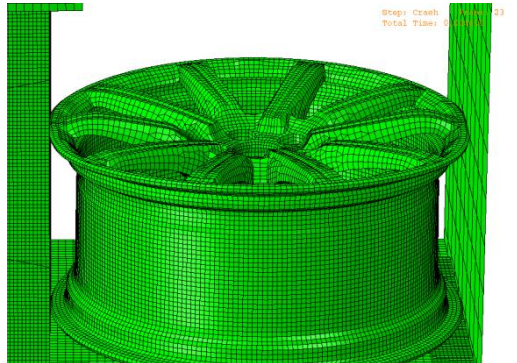
Rim 3 – Short spoke configuration



Rim 4 – Long spoke configuration



Numerical – Short spoke configuration



25 mm deformation

Rim 1 – Short spoke configuration



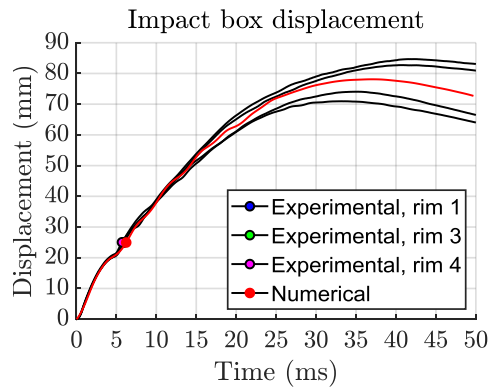
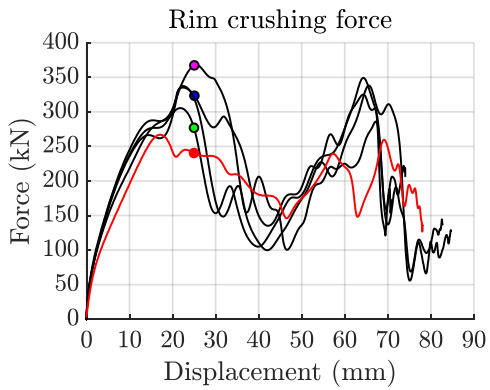
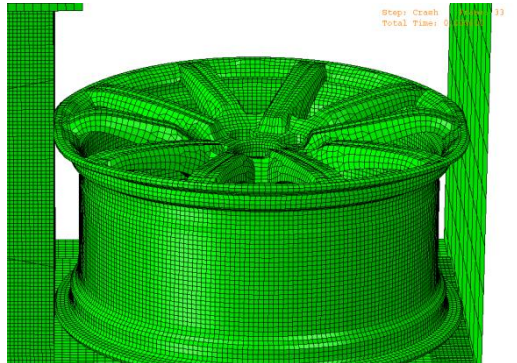
Rim 3 – Short spoke configuration



Rim 4 – Long spoke configuration



Numerical – Short spoke configuration





35 mm deformation

Rim 1 – Short spoke configuration



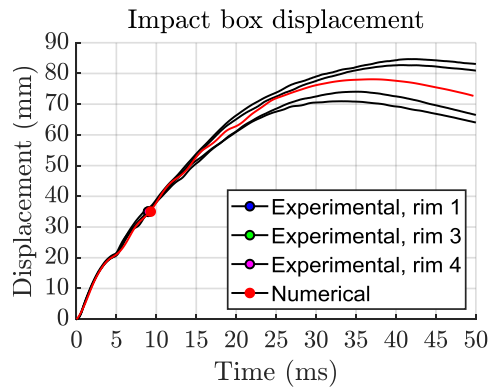
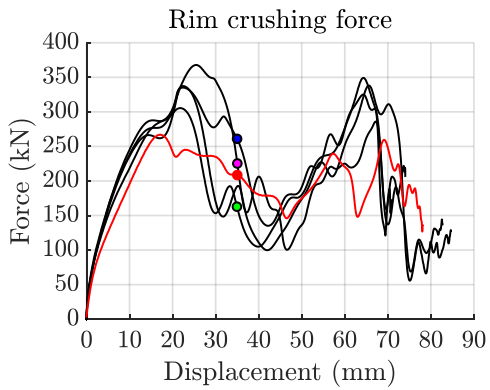
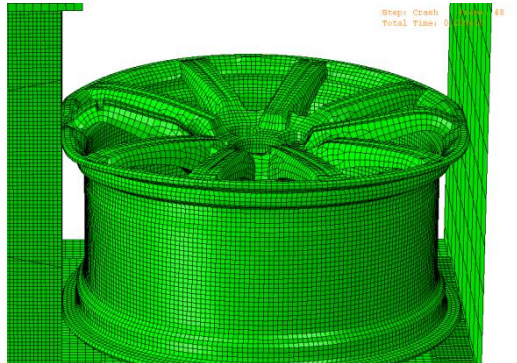
Rim 3 – Short spoke configuration



Rim 4 – Long spoke configuration



Numerical – Short spoke configuration



40 mm deformation

Rim 1 – Short spoke configuration



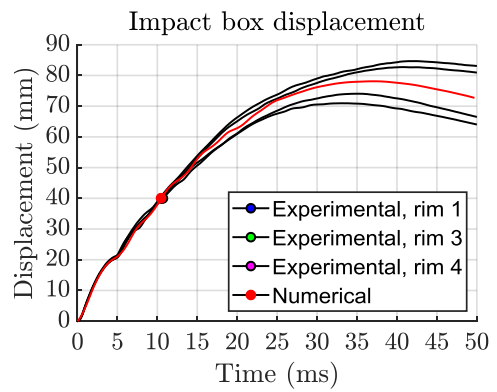
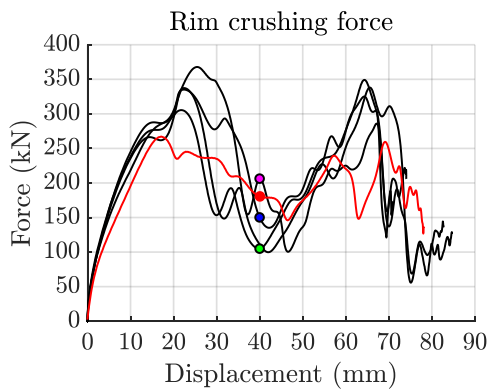
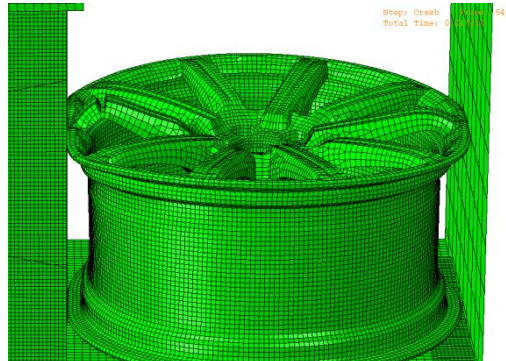
Rim 3 – Short spoke configuration



Rim 4 – Long spoke configuration



Numerical – Short spoke configuration



45 mm deformation

Rim 1 – Short spoke configuration



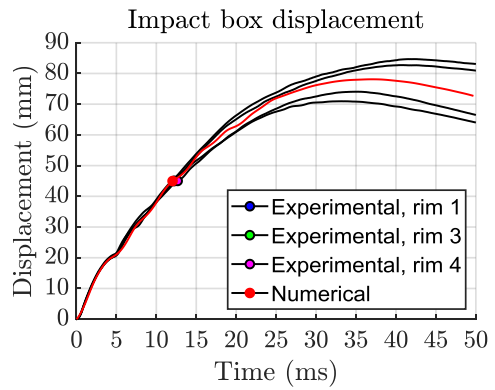
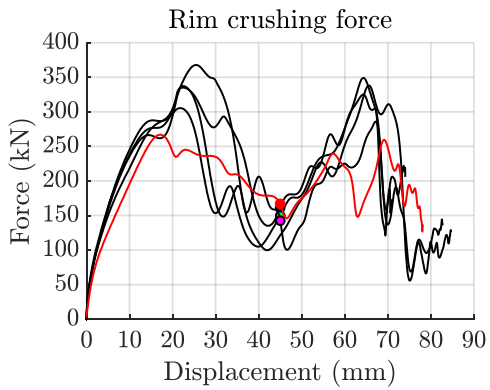
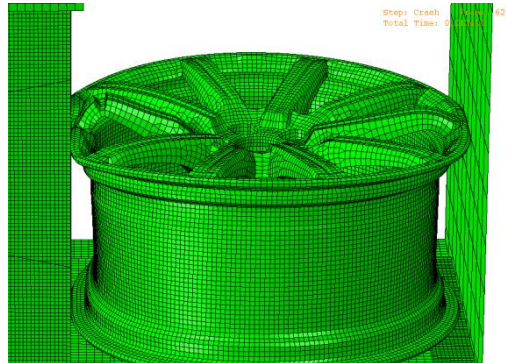
Rim 3 – Short spoke configuration



Rim 4 – Long spoke configuration



Numerical – Short spoke configuration



---

50 mm deformation

Rim 1 – Short spoke configuration



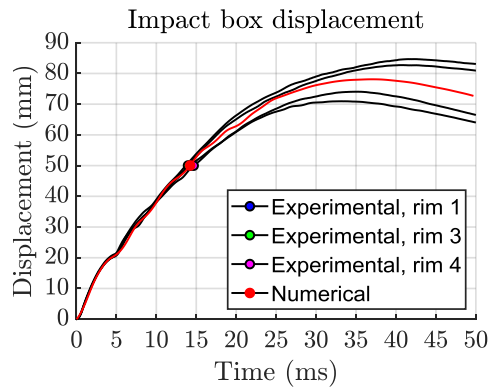
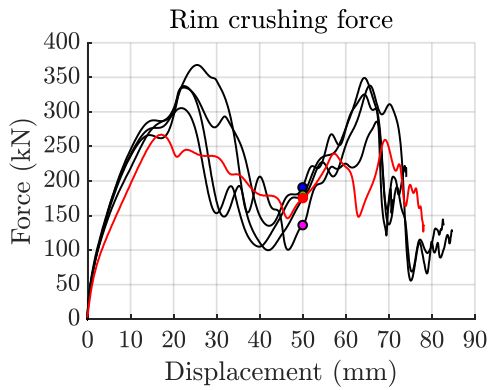
Rim 3 – Short spoke configuration



Rim 4 – Long spoke configuration



Numerical – Short spoke configuration





60 mm deformation

Rim 1 – Short spoke configuration



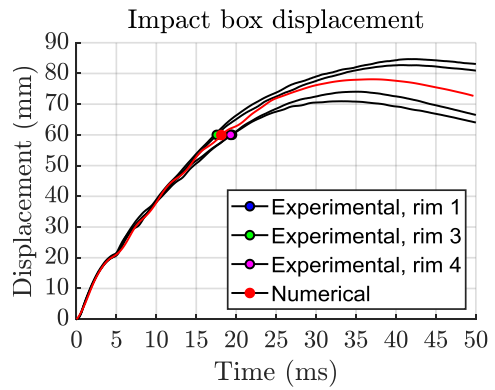
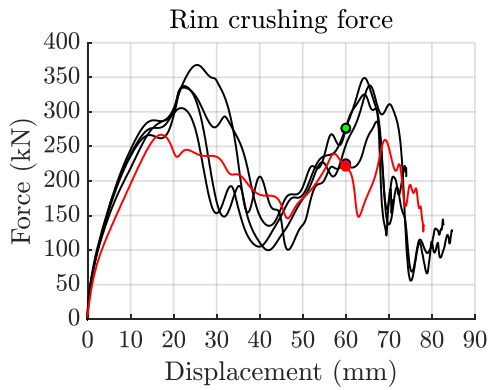
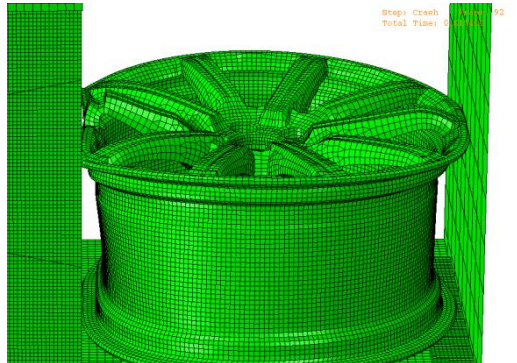
Rim 3 – Short spoke configuration



Rim 4 – Long spoke configuration



Numerical – Short spoke configuration



65 mm deformation

Rim 1 – Short spoke configuration



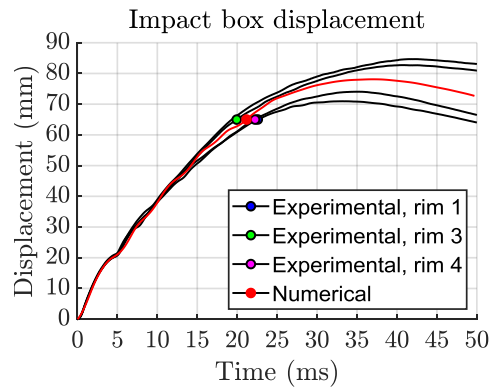
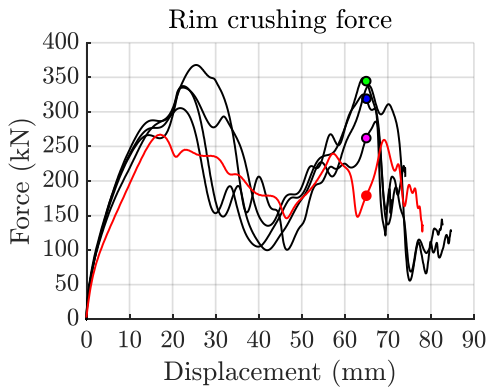
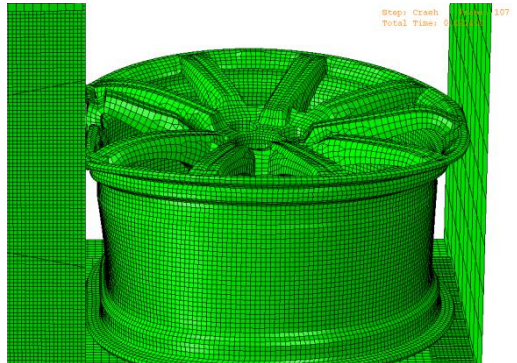
Rim 3 – Short spoke configuration



Rim 4 – Long spoke configuration



Numerical – Short spoke configuration



---

70 mm deformation

Rim 1 – Short spoke configuration



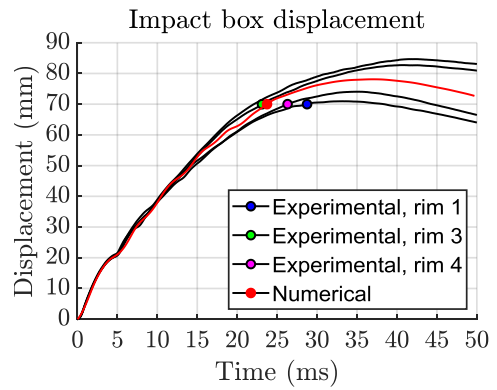
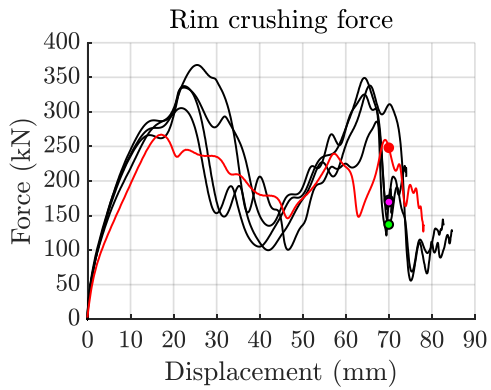
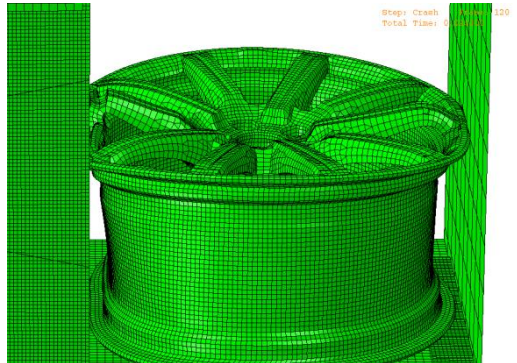
Rim 3 – Short spoke configuration



Rim 4 – Long spoke configuration



Numerical – Short spoke configuration



75 mm deformation

Rim 1 – Short spoke configuration (71 mm)



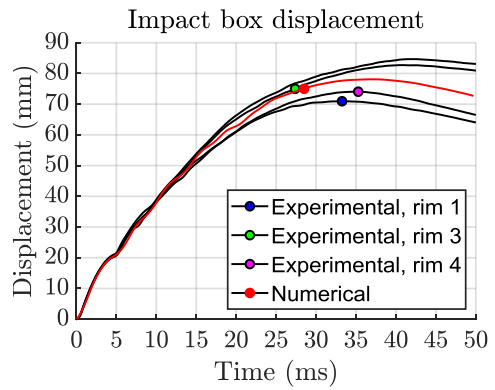
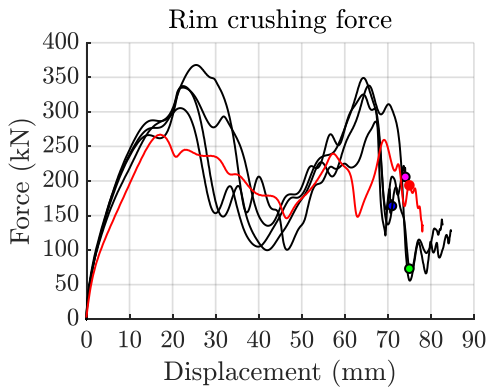
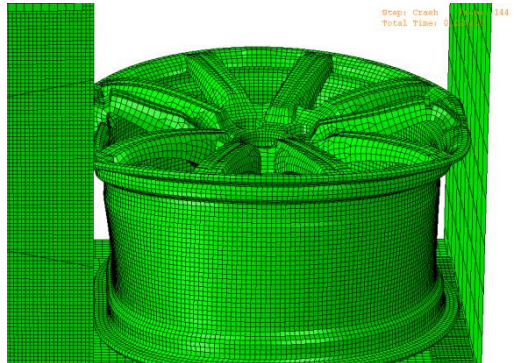
Rim 3 – Short spoke configuration



Rim 4 – Short spoke configuration (74 mm)



Numerical – Short spoke configuration



80 mm deformation

Rim 1 – Short spoke configuration (71 mm)



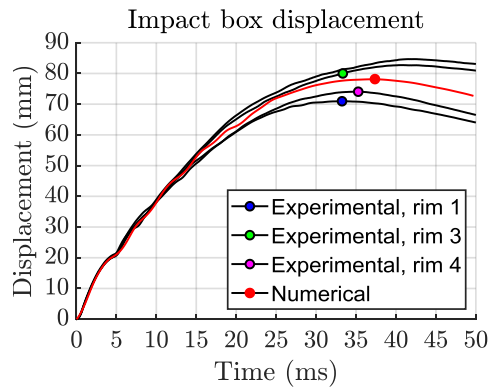
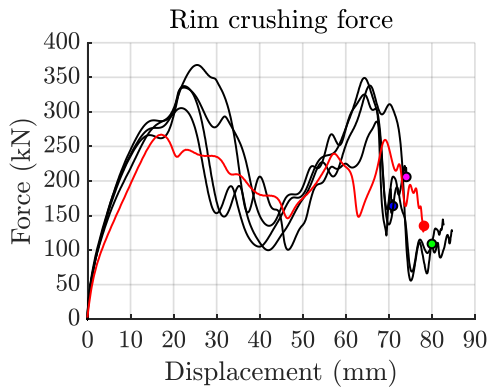
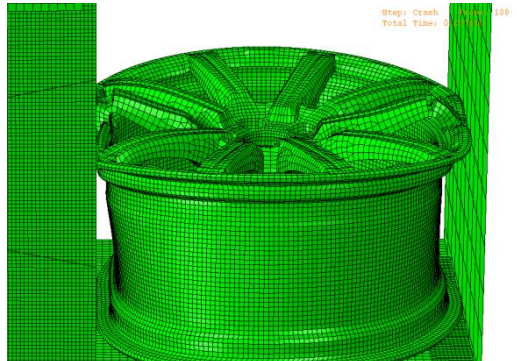
Rim 3 – Short spoke configuration



Rim 4 – Short spoke configuration (74 mm)



Numerical – Short spoke configuration (78 mm)





---

---

